Modelling of Interaction between Plasticity and Martensitic Phase Transformation in Shape Memory Alloys

AMIRHOSEIN SAKHAEI

(*M.Sc.*, IUT)

A THESIS SUBMITTED

FOR THE DEGREE OF DOCTOR OF PHILOSOPHY

DEPARTMENT OF MECHANICAL ENGINEERING

NATIONAL UNIVERSITY OF SINGAPORE

2014

Declaration

I hereby declare that the thesis is my original work and it has been written by me in its entirety. I have duly acknowledged all the sources of information which have been used in the thesis.

This thesis has also not been submitted for any degree in any university previously.

AMIRHOSEIN SAKHAEI

December 10, 2014

To my inspiring parents

Badri and Mohammad Hasan,

for their endless love, support and encouragement.

Acknowledgments

First and foremost, I would like to express my sincere gratitude to my highly respected supervisor, Associate Professor Lim Kian Meng for the continuous support and encouragement throughout my Ph.D study. His knowledge, expertise, and innumerable discussions I had with him added considerably to my graduate experience. I am also grateful that despite his busy schedule he managed to allocate time to read and comment critically on my thesis.

I would also like to thank Associate Professor Sergio Turteltaub and Professor Erik Van der Giessen for offering me the research attachment opportunity in Delft University of Technology and guiding me working on the discrete dislocation-transformation method. I have learned many precious points during several long distance discussions with them. In addition, I would like to warmly thank Professor Prakash Thamburaja for guiding me during this study by his profound knowledge of continuum mechanics and finite element theories.

My sincerest thanks to my colleagues and friends in the experimental mechanics laboratory in NUS; Dr. Mostafa Jamshidian, Dr. Long Bin Tan, Sara Adibi, Saeid Arabnejad, and shahrokh Sepehri and my colleague in Delft University of Technology; Sourena Yadegari. I appreciate their friendship and many useful discussions we had about my research. I would also like to thank Mr. Chiam Tow Jong, our friendly lab officer for his

sincere help and support during my work at NUS.

I would also like to thank my parents, two elder sisters, and my brother. They were always supporting and encouraging me with their best wishes.

Last but not the least, I thank my institution, National University of Singapore, specially the department of Mechanical Engineering for providing me with research facilities during the entire course of my candidature. I also gratefully acknowledge the Singapore International Graduate Award (SINGA scholarship) provided to me by Agency for Science, Technology and Research (A*STAR).

Contents

Summary

Dislocation slip and martensitic phase transformation are two important deformation mechanisms in shape memory alloys (SMAs) and the interaction between them affects the pseudoelasticity and shape memory effect behaviors. These influence the reversibility behavior and also actuation behavior of SMAs under cyclic loadings. To reduce irreversibility and improve actuation behavior, a lot of studies have been conducted in the recent years. The aim of this study is to model the dislocation slip and phase transformation mechanisms in micro-scale and investigate the micro-structural effects of (i) dislocations on martensitic transformation, (ii) phase transformation on dislocation slip and (iii) interaction of both phenomenon on the total reversibility of SMA.

In the first part of this study, the two-dimensional discrete dislocation dynamic was used to model the plastic deformation in the BCC structure. Furthermore, a two dimensional discrete transformation method was developed for the simulation of martensitic transformation in the same scale as dislocation slip. The discrete transformation framework is based on the kinetics of austenite-martensite interface by computing the thermo-mechanical driving force on the transformation interface. Therefore it is capable of simulating the two-way phase transformation under thermo-mechanical loading. The main results show the effect of dislocations on irreversibility of SMAs and the reduction in plastic strain by multiple cy-

cling processes. The existence of dislocations also affects the occurrence of the phase transformation in lower stresses.

In the second part of this study, the interaction between plasticity and phase transformation was modeled in macroscopic scale. The constitutive equations were presented by considering the transformation induced plastic deformation in addition to martensitic transformation and plasticity. The model was numerically implemented in VUMAT subroutine and it was applied in three-dimensional finite element simulations in ABAQUS package. The comparison of results with experiments shows the validity of the model to predict the mechanical behavior of SMAs under thermo-mechanical loading in macro-scale applications.

Overall, this study is a micro-mechanics investigation on the interaction between plasticity and phase transformation. It also suggests some of the possible processes to improve the reversibility behavior of shape memory alloys.

List of Tables

List of Figures

List of Symbols

$\boldsymbol{\sigma}$	Stress field tensor
$\boldsymbol{\varepsilon}$	Strain field tensor
$\boldsymbol{\varepsilon}^{tr}$	Transformation strain
$\boldsymbol{a}$	Transformation strain vector
$\boldsymbol{m}$	Habit plane normal
$\boldsymbol{n}$	Slip plane normal for dislocation i
$\boldsymbol{t}$	Traction force on the boundary
$\boldsymbol{u}$	Displacement field vector
$\dot{\varepsilon}$	Applied strain rate
ϵ	Internal energy per unit reference volume
η	Entropy per unit reference volume
κ	Bulk modulus
λ	Transformation latent heat
$\mathbb{C}$	Fourth-order stiffness tensors
$\mathbb{S}$	Fourth order Eshelby's tensor for interior points
$\mathbf{C}^e$	Elastic right Cauchy-Green strain tensor
$\mathbf{E}^e$	Elastic Green strain tensor
$\mathbf{F}$	Deformation gradient
$\mathbf{L}$	Velocity gradient tensor
$\mathbf{q}$	Heat flux per unit referential area
$\mathbf{R}$	Rotation tensor

$\mathbf{S}$	First Piola Kirchhoff stress tensor
$\mathbf{T}$	Cauchy stress
$\mathbf{U}$	Stretch tensor
μ	Shear modulus
ν	Poisson's ratio
ψ	Helmholtz free energy
ρ^d	Dislocation density
ρ^d_{source}	Dislocation source density
ρ^m_{source}	Transformation source density
τ_i^{cr}	Critical resolved shear stress of dislocation i
τ_{obs}	Obstacles' strength
$\mathbf{b}^i$	Burgers vector of dislocation i
θ	Temperature
ζ	Martensitic volume fraction
A_f	Austenite finish temperature
A_s	Austenite start temperature
B_d	Drag coefficient
f_j^{tr}	Transformation driving force
f_i^d	Peach-Koehler force of dislocation i
M_d	Martensitic transformation temperature
M_f	Martensite finish temperature
M_s	Martensite start temperature
r	Heat supply per unit reference volume
t	Time

Chapter 1

Introduction

Shape memory alloys (SMAs) are kinds of metallic materials that are able to regain an initial shape by applying appropriate thermal or mechanical loads. The first SMA was discovered in 1951 by Chang and Read [1]. Then, it rapidly attracted the attention of material scientists due to its unique functional behaviors. The particular behaviors of SMAs are the ”shape memory effect” and ”superelasticity” which are caused by the mechanism of martensitic phase transformation. The shape-memory effect (SME) is a phenomenon to recover from the deformation of martensitic phase completely by heating up the material to austenitic phase. Pseudoelasticity or superelasticity is an isothermal behavior due to the stress-induced martensitic transformation when the material is originally in austenitic phase. Due to these properties, SMAs are employed in different applications such as actuators and sensors in aerospace, oil and gas, automation, and biomedical

industries [2–5].

1.1 Interaction between martensitic transformation and plasticity

Martensitic transformation is a diffusion-less solid-solid transformation between a higher symmetry parent phase named austenite and a lower symmetry product phase named martensite. It is caused by shear distortion of the atomistic structure along a specific plane named habit plane. The martensitic transformation is reversible because the atomic structure of austenitic phase is obtainable by heating up the martensitic phase. The martensitic transformation causes the recoverable inelastic strain with hysteric behavior under cyclic thermo-mechanical loading.

The transformation hysteresis under thermal and mechanical cyclic loading are illustrated schematically in Figures 1.1a and 1.1b. In these figures, (M_s) and (M_f) are martensite start and martensite finish temperatures which are the temperatures at which transformation from austenite to martensite begins and finishes, respectively. Similarly, (A_s) and (A_f) are the austenite start and finish temperatures, respectively [6].

In addition to martensitic transformation, dislocation plasticity is another deformation mechanism which affects the performance of the SMAs [7–10]. The coupling of plasticity and transformation in SMAs produces ir-

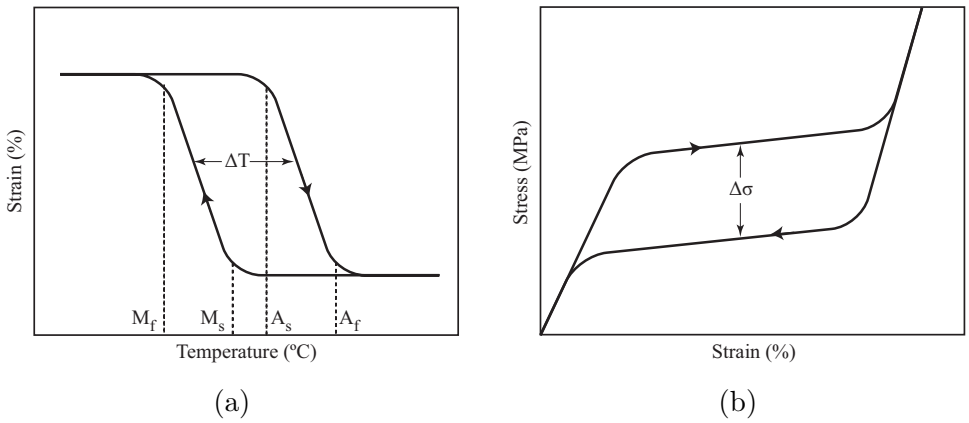

Figure 1.1: Schematic of transformation hysteresis. (a): Typical strain-temperature curve, where ΔT is temperature hysteresis, (b) Isothermal stress-strain curve describing superelasticity, where $\Delta\boldsymbol{\sigma}$ is stress hysteresis.

recoverable strain and reduces the work output under cyclic loading. This poor stability under thermal cyclic loading is experimentally illustrated in [11–14]. As it is explained in [3] and shown in Figure 1.2, the recoverable strain is due to the transformation from austenite to detwinned martensite and mechanical elastic strain, while the irrecoverable strain is due to the plastic deformation under thermal cycling when external traction is prescribed. Furthermore, the instability during superelasticity is reported in [15–18]. As it is illustrated schematically in Figure 1.3 and discussed in [3], the material is originally in the austenite phase and the inelastic recoverable strain is due to the transformation and detwinning of the martensitic phase, while the irrecoverable strain at the end of unloading is due to the plastic strain that is generated under loading and unloading processes.

In addition to the effect of plastic deformation on the cyclic behavior of

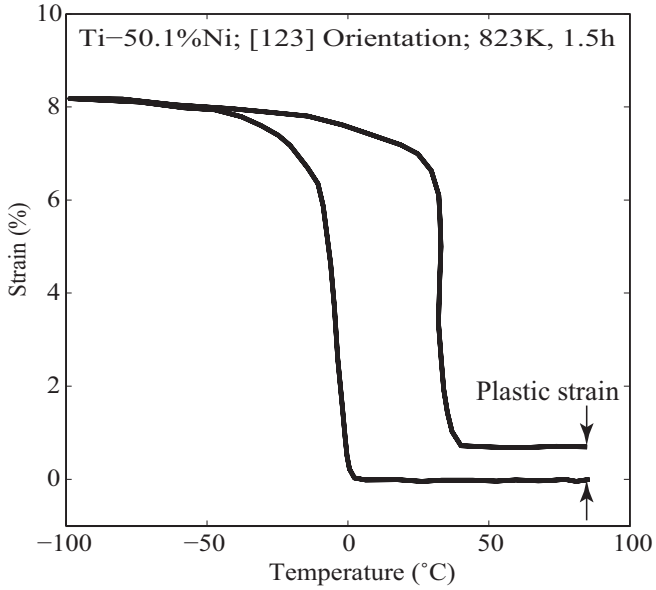

Figure 1.2: Plastic strain in Ti-50.1at.% Ni single crystal in the [1 2 3] orientation under thermal cycling and constant stress 175 MPa [14].

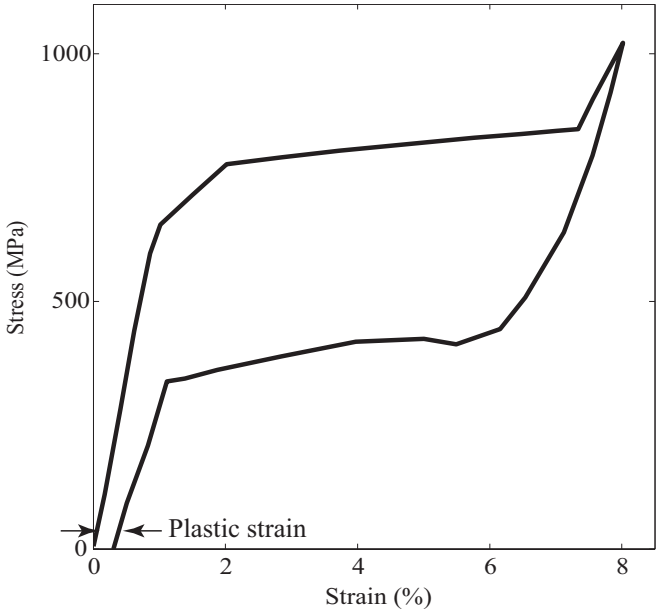

Figure 1.3: Plastic deformation of NiTi sample under mechanical loading at constant applied temperature of $100°C$ [16].

SMAs, there are other mechanisms that may occur simultaneously with the phase transformation. One of these mechanisms is transformation-induced

plasticity (TRIP) that explains the generation of plastic strain during the martensitic transformation. It is known as the effect of transformation on the dislocation dynamics. Although TRIP is firstly explained in some steel alloys [19–21], the appearance of TRIP in SMAs is also discussed in literature [22–24]. It is indicated that the local stress fields of martensitic transformation may affect the activation of plastic mechanisms. It is an important issue for SMAs that shows irreversible strain during cyclic loading where the external stress is lower than yield stress of the material.

Furthermore, the dislocations in the structure of SMAs may affect the motion and nucleation of the martensitic regions. It is explained that the local stress field which is produced by dislocations influences the mechanism of phase transformation. However, according to the experimental reports, it is still unclear whether the dislocations assist the martensitic transformation (so called dislocation-induced transformation) [25, 26] or resist the growth of the martensite-austenite interface [27, 28].

1.2 Rationale and Aims

By increasing the application of devices made from SMAs, many investigations on physical behavior of SMAs have been performed recently. With the development of the computational facilities in the last two decades, many different numerical models have been presented to simulate the thermomechanical behavior of SMAs. These models vary from constitutive mod-

eling in macro-scale (e.g., [29, 30]) to atomistic simulation in nano-scale (e.g., [31,32]). The phenomenological continuum models are useful to simulate the large-scale three dimensional devices. Furthermore, they are capable of solving problems with complicated geometry. However, the continuum models are unable to capture the physical mechanisms that occurred in microstructure of SMA during phase transformation and plastic deformations.

Discrete dislocation dynamic gives the opportunity to model the microstructure of plastic deformation by considering the nucleation, motion, and annihilation of dislocations [33, 34]. Shi et al. [35] combined the discrete dislocation method with a proposed discrete transformation model to simulate the effect of phase transformation on plasticity in the TRIP steels. However their model is unable to predict reversible transformation in SMAs, and also it is unable to simulate the response of material under thermal loading. It is clear that the two-way martensitic transformation and the thermal cyclic loading are the crucial elements to study the behavior of SMAs. Therefore, in this study, a modified discrete transformation model for SMAs is coupled with discrete dislocation method to present a new discrete dislocation-transformation framework. This framework is capable of simulating the two-way shape memory behavior of SMA under thermo-mechanical loadings. Then, the model is applied to study the microstructure of the interaction between phase transformation and austenitic

plasticity under cyclic thermal and mechanical loading for both single and multi crystal samples of SMA. The study about the interaction between martensitic transformation and plasticity includes the effect of dislocation on phase transformation and the influence of transformation on dislocation plasticity as well as effects of both mechanisms on the mechanical behavior of SMA under cyclic thermo-mechanical loadings. Moreover, the effects of grain boundaries and grain sizes on the martensitic growth and dislocation plasticity are studied by modeling the multi-crystalline samples with the proposed discrete dislocation-transformation framework.

Furthermore, in the macro-scale level, most of the available continuum models do not consider the transformation-indiced plasticity (TRIP) as an active deformation mechanisms for SMAs. However, it is previously explained how plastic deformations may affect the SMA stability under cyclic loading. Therefore, a continuum model in macro-scale is presented such that the phenomenological formulations are qualitatively linked with the discrete dislocation-transformation results. This model is applied to simulate the industrial applications of SMA by considering the interaction between plasticity and phase transformation.

This thesis focuses on the simulation of interaction between plasticity and martensitic transformation in SMA. Therefore, the experimental observations of other researchers are taken to understand the physics and verify some of the numerical results.

1.3 Outline of the thesis

In this chapter the importance of shape memory alloys and the necessity of modeling the interaction between plasticity and phase transformation for SMAs are presented. Furthermore, the strategies to model the behaviors of SMA are discussed briefly. In Chapter 2, a comprehensive literature review on the background of SMAs and deformation mechanisms in shape memory alloys are presented.

The discrete dislocation-transformation method and the numerical implementations for modeling the micro-scale behavior of shape memory alloys are presented in Chapter 3. This chapter includes the equations to calculate the local stress, strain, and displacement fields due to the dislocations and martensitic inclusions as well as rules for dislocation dynamics, and nucleation, growth, and annihilation of martensitic transformation under thermo-mechanical loading.

The discrete dislocation-transformation model which is developed in Chapter 3 is used in Chapter 4 to simulate the behavior of single-crystalline NiTi. Thus, the isothermal pseudoelasticity and two-way shape memory effect behaviors of single-crystalline sample are simulated under thermo-mechanical loadings and the interaction between martensitic transformation and plasticity is investigated in the microstructure of the single-crystal samples. Moreover, the behavior of SMAs under multi-cyclic thermal and mechanical loadings is studied in this chapter.

Furthermore, in Chapter 5, the results of simulation of multi-crystalline NiTi under thermo-mechanical loadings are presented. The interaction between plasticity and phase transformation in the presence of grain boundaries is analyzed in this chapter. Moreover, the orientation effect, grain size effects, and the interaction of grain boundaries on dislocation dynamic and martensitic transformation are studied in this section.

A phenomenological continuum model is presented in Chapter 6 to model the mechanical behavior of SMAs in macro-scale including the interaction between plasticity and phase transformation. This model is used to simulate the large-scale and industrial application of SMAs. It is worth mentioning that although this study is not a multi-scale analysis, the phenomenological rules in this chapter are linked with the results from microstructural simulation qualitatively.

Although each chapter has an individual conclusion, the overview of the whole study, the significant results of each chapter, and possible future works are presented in Chapter 7.

1.4 General scheme of notations

In this thesis all the notations are according to the following scheme:

- Scalars are written as lowercase italic letters (e.g., a, b),
- First-order tensors are written as bold lowercase italic letters (e.g.,

$\boldsymbol{a}$, $\boldsymbol{b}$),

- Second-order tensors are written as bold uppercase italic letters (e.g., $\boldsymbol{A}$, $\boldsymbol{B}$), except for the stress and strain tensors that bold lowercase Greek letters are used (i.e., $\boldsymbol{\sigma}$, and $\boldsymbol{\varepsilon}$),

- Fourth-order tensors are written as blackboard bold uppercase letters (e.g., $\mathbb{A}$, $\mathbb{B}$),

- The inner product is indicated by a single dot between quantities (e.g., $\boldsymbol{a}.\boldsymbol{b}$, $\boldsymbol{A}.\boldsymbol{B}$),

- The tensor product is indicated similar to $\boldsymbol{a} \otimes \boldsymbol{b}$ and $\boldsymbol{A} \otimes \boldsymbol{B}$,

- The product of two tensor is denoted like: (e.g., $\boldsymbol{A}\boldsymbol{b}$, $\boldsymbol{A}\boldsymbol{B}$).

Chapter 2

Literature review

The importance of the investigation of interaction between martensitic transformation and plasticity for shape memory alloys was presented in Chapter 1. A more comprehensive review on the background of SMAs, their industrial applications, different active deformation mechanisms under thermo-mechanical loadings, and simulation strategies to investigate the behavior of SMAs are presented in this chapter.

2.1 Background of shape memory alloys

Shape memory alloys (SMAs) have the ability to recover from the macroscopic strain under thermo-mechanical loading. Furthermore, they can consume and dissipate energy and show reversible and hysteric behavior when they are under cyclic thermal and/or mechanical loadings. These significant properties attracted a lot of attention to use SMAs in industrial

applications.

The first SMA (Au-Cd) was discovered at 1951 by Chang and Read [1] but the rise of attention towards shape memory alloys was during the discovery of NiTi at early 1960s by Buehler et al. [36,37]. Nitinol is a famous name for NiTi, because NiTi was firstly discovered in a lab with the name "*Nickel Titanium Naval Ordnance Laboratory*". Since then, many investigations have been done on the metallurgy of SMAs and their different industrial applications. Currently, NiTi is one of the most favored SMAs for medical and non-medical applications [2,38–41]. However, the transformation temperature of binary NiTi varies between $-50°C$ to $+110°C$ [42] and it is not suitable to use in high temperature applications in aerospace and power generation industries. On the other hand, recent researches show that alloying binary NiTi with more than 10% of Pd, Pt, Hf, or Zr increases the transformation temperatures to values up to $500°C$ [43–49]. The SMAs with transformation temperatures above $100°C$ are called high temperature shape memory alloys (HTSMAs). There is also another type of shape memory alloys that is induced by magnetic fields. This alloy is called ferromagnetic shape memory alloy (FSMA) or magnetic shape memory alloy (MSMA) and has attracted a lot of attention due to their faster and more efficient magnetic-induced response in comparison with other SMAs [50–53].

2.1.1 Shape memory effect and pseudoelasticity

A shape memory alloy experiences a diffusion-less and solid-solid transformation between two different crystal structures. The phase at higher temperature is called austenite or parent phase and it has cubic crystalline structure. The structure at lower temperature is called martensite or product phase and the crystalline structure is different for various types of SMAs for example, the crystal of NiTi in martensitic phase has monoclinic shape. When the martensitic phase is heated, it starts to transform to austenite at a special temperature A_s. It is called the austenite start temperature. The temperature at which material is transformed fully to austenite is called A_f. Similarly, M_s and M_f are the martensite start and finish temperatures at which the austenitic phase begins and finishes to transform to martensite as the temperature is decreased [37].

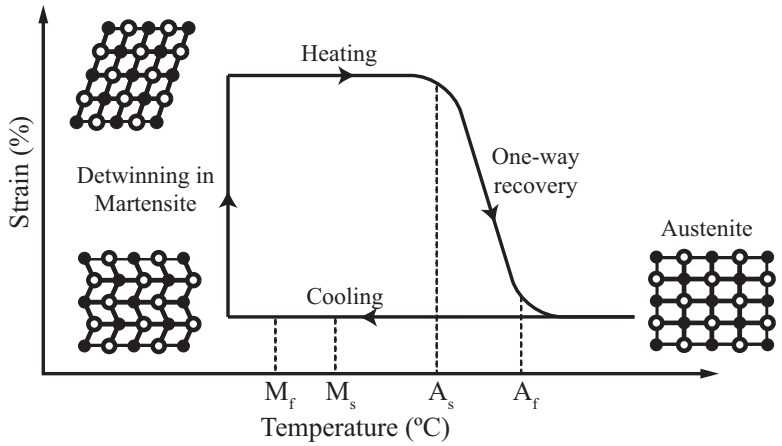

Figure 2.1: One way shape memory effect under thermo-mechanical loading.

The shape memory effect (SME) and superelasticity (SE) are the unique

properties of SMAs which are due to the martensitic transformation phenomena under thermal and/or mechanical loading. The ability to recover from the deformation which is applied to the material in martensitic phase (low temperature) by heating to the austenitic phase, is called the one-way shape memory effect (OWSME). The Schematic of the one-way shape memory effect including the structural changes is presented in Figure 2.1. Furthermore, the two-way shape memory effect (TWSME) is characterized by the reversible shape change of SMA on both heating and cooling which is only possible after employing training procedure. The schematic of the two-way shape memory effect is shown in Figure 2.2.

Superelasticity (pseudoelasticity) is the ability of SMAs to recover the original shape after an isothermal loading-unloading process. It is associated with inelastic and recoverable strain which is caused by stress-induced transformation. The material should be initially in the austenitic phase where the temperature is above A_f and lower than M_d. M_d is the temperature that the required energy for stress-induced transformation is equal to the energy for dislocation slip [54]. Therefore above M_d, SMA experiences dislocation slip similar to the other metallic alloys with no phase transformation. The schematic of the superelasticity behavior of SMAs is illustrated in Figure 2.3.

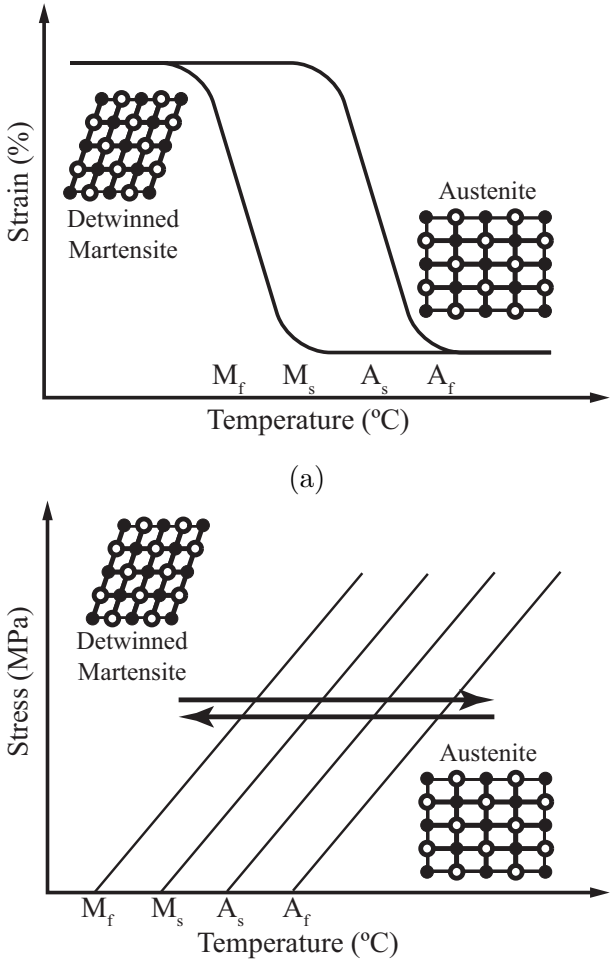

Figure 2.2: Schematic of two-way shape memory effect after experiencing training under applied stress: (a) The strain-temperature behavior (b) The stress-temperature diagram.

2.1.2 Applications of shape memory alloys

As mentioned earlier, shape memory effect (SME) and superelasticity (SE) are the significant properties of SMAs that make them useful in diverse applications. For example, the SMAs are used as actuators because the SME behavior generates motion or strain when the device is under stress [55]. SMAs are employed in many different fields but here we divide the

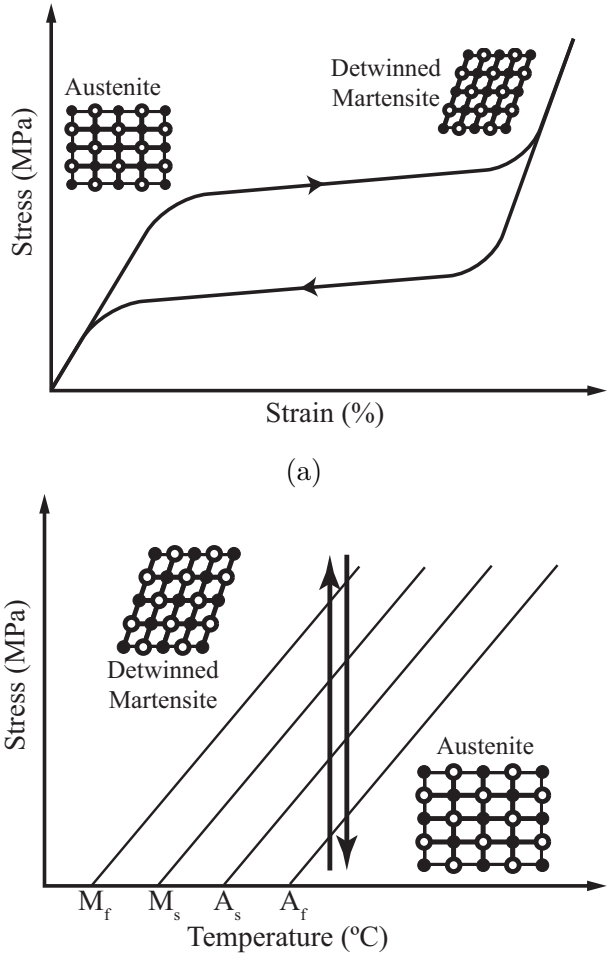

Figure 2.3: Schematic of isothermal pseudoelasticity: (a) The stress-strain diagram, (b) The stress-temperature diagram.

applications in three main groups of automotive, medical, and aerospace applications.

In the history of shape memory alloy, one of the first applications of SMAs was implant in dentistry [56,57]. Although SMAs are more expensive than steel, they quickly replace stainless steel in biomedical applications. High corrosion resistance, non-magnetic behavior, operation temperature around the human body temperature, and bio-compatibility with bones

and tissues are the main benefits of using the SMAs in the biomedical field [58–60]. SMAs also use in medical devices such as stents, guide wires, and eyeglass frames. The more complete reviews on medical applications of SMAs are presented in [50, 61].

One of the other applications of SMA is in the automotive industry because the actuators and sensors made by SMAs are used in different parts of present-day vehicles [50, 62]. Using SMA actuators has benefits in comparison to other type of actuators due to the smaller, lighter, and cheaper components. The sensors and actuators can be used in exterior parts and body, as well as in the motor of the vehicle [63,64]. Most of the applications in the exterior parts are covered by the binary NiTi because the working temperatures of NiTi devices are near environment temperature. However, the actuators and the sensors working inside or on the frame of the engine need to work in higher temperatures than room temperature. Therefore, high temperature shape memory alloys are used for these applications [65]. Using HTSMA actuators makes the design more expensive, and it causes challenges related to brittleness, stability and fatigue strength.

SMAs are also applied as actuator wires, vibration dampers, connectors, manipulator, and torque tubes in aerospace applications [3, 66, 67]. Although the devices are expensive for most of the cases, they have been applied widely in jet engines and aircraft wings during the last decade [2,68]. Furthermore, the significant mechanical properties of SMAs presented them

as a solution for problems in high dynamic load and space situations.

Although aerospace, automotive, and medical fields are well-known as the main industries that SMAs have applications, there are many other situations that SMAs are used or they are proposed as a solution for a problem. These applications vary from actuators in robotic [69, 70] to vibration controller with pseudoelastic behavior in civil structures [71, 72]. In the recent years, the oil and gas industry also shows interests in using SMA actuators [73]. However, the high operating temperatures for these devices limited the SMAs to high temperature shape memory alloys in this industry.

2.2 Response of SMA under thermo-mechanical loading

As discussed earlier, martensitic transformation can be activated by both thermal and mechanical loading. Therefore, it is sometime categorized as temperature-induced transformation and stress-induced transformation. The temperature-induced transformation occurs when the SMA is under suitable temperature cycling with or without external stresses. The stress-induced transformation takes place when SMA experiences appropriate external forces under isothermal condition. In the following sections, the mechanical behaviors of SMA under different loading conditions are dis-

cussed.

2.2.1 Temperature cycling (under stress or stress free)

In this kind of loading, the material is assumed to be in austenitic phase at high temperature. Then it transforms to martensitic phase by cooling to a specific temperature and it transforms back to austenite by heating to the initial temperature. Furthermore, the dislocation slip in austenitic phase can affect the behavior of SMA under thermal cycling. Miyazaki et al. [74] observed that the generated dislocations under temperature cycling can delay the phase transformation. Hamilton et al. [14] illustrated that when the bias applied stress is more than 150 MPa, the thermal cycling of NiTi is not fully recoverable. However, it has been shown that, for the specific SMAs that the generation and motion of dislocations are difficult, the temperature cycling is fully reversible [75, 76]. For example, Hamilton et al. [14] showed that aged NiTi has more resistance to plasticity, and the thermal cycles under different applied stress are recoverable for aged NiTi.

In addition to the macroscopic behavior of SMA, some researchers observed the existence of dislocations in the microstructure of SMAs experimentally. It was recently observed that dislocations are created in austenitic phase after phase transformation [26, 74, 77–79]. Pelton et al. [78] performed some microstructural study on SMAs undergoing thermal cycling. They observed that the dislocation density in austenitic phase in-

creases from $10^{12}m^{-2}$ in a quench specimen to $5\times10^{14}m^{-2}$ after 100 thermal cycles. Simon [79] also suggested a mechanism to explain the generation of dislocations that are induced by transformation. Figure 2.4 shows a sample TEM result that is captured from the microstructure of SMA [78].

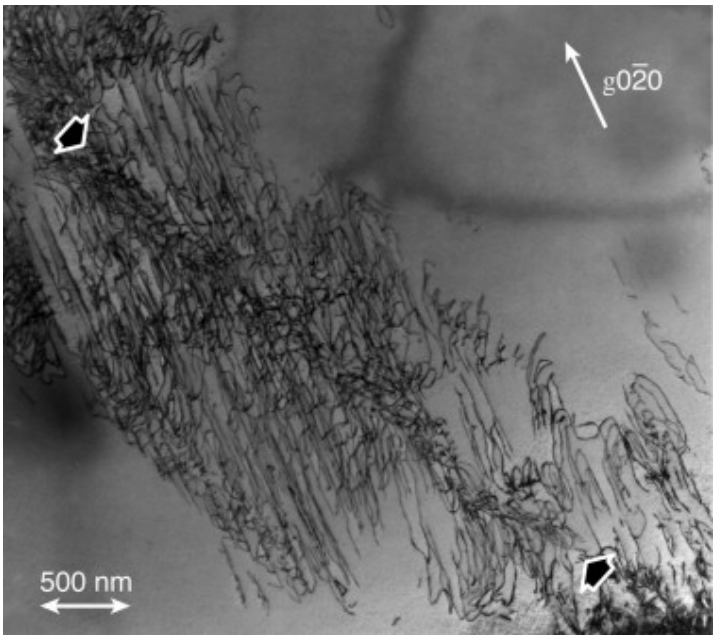

Figure 2.4: Large array of dislocation loops in the cubic austenite phase of the $Ni_{50.5}Ti_{49}$ specimens after one thermal cycle. The image is directly from [78].

2.2.2 Isothermal mechanical loading at $A_f < \theta < M_d$

When the SMA is loaded mechanically at constant temperature ($A_f < \theta < M_d$), the stress-induced transformation occurs. The local stress due to the external loading and local field of transformation can generate and drive dislocations along the slip planes. Therefore, the dislocation slip causes residual strain after each loading-unloading cycles. This behavior is observed experimentally in the stress-strain responses of the SMAs [54, 75,

80, 81] as well as microscopic evidences in TEM analysis [76, 82–84].

Shaw [80] and Miyazaki et al. [54] are the first researchers who studied the macroscopic behavior of pseduelasticity under uni-axial loading for NiTi. Strnadel et al. [81] also studied the stress-strain cyclic behavior of NiTi and NiTiCu, and investigated the plasticity of austenitic phase under mechanical loading.

The plastic strain is always undesirable for actuation behavior of SMAs. Therefor, many efforts have been done to prevent or reduce the plastic deformation of SMAs under cyclic loading. There are different solutions to minimize the dislocation slip such as adding precipitations to microstructure [83] and grain refinement [85, 86]. Sehitoglu et al. [75] showed that creating Ni-rich NiTi alloys increases the slip resistance and decreases the residual strain in pseudoelasticity. Gall et all [83] also investigated the effect of Ti_3Ni_4 precipitant in NiTi. They concluded that the smaller size of precipitants can reduce the dislocation generation and plastic strain in pseudoelasticity cycle.

Perkin [87] was one of the first scientists who studied the microstructure of SMAs. He indicated the importance of the interaction between dislocations and martensitic transformation in shape memory alloys. Norfleet et al. [82] illustrated the generation of dislocations during the martensitic transformation in NiTi micropillars with STEM experiments. He then studied the effect of specimen size on dislocation plasticity. Delville et

al. [84] investigated the effect of grain size on dislocation slip by TEM experiments. They observed that the dislocation density is higher in bigger grain size samples. Furthermore, they concluded that the effect of dislocation slip on pseudoelasticity is increasing when the temperature is higher. Ibarra et al. [26] studied the structure of dislocations after stress-induced transformation mechanism in CuALNi single crystal. They divided the generated dislocations into two groups. The first group of dislocations are generated at austenite-martensite interface, working as obstacles against the transformation. The second group consists of dislocations from plastic deformation in martensite that help the phase transformation. Figure 2.5 shows a sample TEM result which captured the dislocation tangles after superelasticity [84].

The interaction between dislocations and transformation has been a challenging discussion among researchers for many years. Some scientists proposed that the dislocations assist the nucleation and motion of martensitic transformation [25, 26]. However, there are many studies that show the resistance role of dislocations against martensitic transformation [27, 28, 88–90]. Furthermore, it was also observed in the experiments that phase transformation induces the nucleation of dislocations [74, 77].

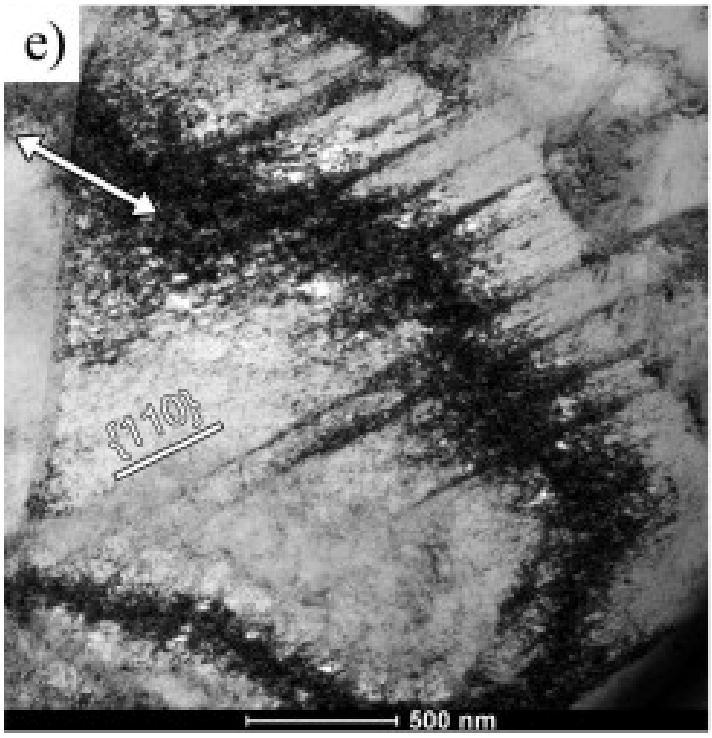

Figure 2.5: The accumulation of dislocations along slip planes in NiTi wire after 10 superelastic cycles. The image is directly from [84].

2.3 Methods to simulate SMA behavior

As discussed in Chapter 1, there are many models from atomistic scale to the continuum level to simulate the mechanical behavior of shape memory alloys. In the first part of this thesis, a discrete dislocation-transformation model is presented to model the interaction between plasticity and phase transformation in the SMAs. It is then used to model the behavior of single and multi crystal NiTi. In the second part of this thesis, a continuum level model is presented to model the mechanical behavior of SMAs at macro-scale level. In the following a review on the both methods used in the literature is presented.

2.3.1 Discrete dislocation-transformation model

The discrete dislocation-transformation method is incorporated from two different models: (i) discrete dislocation and (ii) discrete transformation. The discrete dislocation dynamic (DDD) is a method to simulate the dynamics of dislocations to predict the plastic behavior of crystalline metals at the micro-scale level. To keep the compatibility with the applied models, the discrete transformation is proposed to model the martensitic transformation at the same scale level as discrete dislocation works.

The discrete dislocation is a method to study the nucleation and motion of dislocations. Therefore, it is applied to model the plasticity in microscale without considering the atomistic scale of crystalline metals. In the discrete dislocation dynamic models the dislocations are considered as line defects in elastic domain [91, 92]. Then the constitutive dynamics equations are presented to estimate the position and the formation of dislocations in each time step based on the local stress field.

Many researches have been performed in the field of the discrete dislocation dynamics in the last decade [33, 34, 93–95]. Some of these models simulate the three dimensional behavior of dislocations and estimate the behavior of material by looking at all slip planes interacting with each other [96–101]. Although this kind of modeling is in agreement with the physical view of the crystalline microstructure, the computational cost is a big issue for them. Furthermore, according to the crystallography of the metals, dis-

locations tend to move in some specific planes and directions (energetically minimum) which are called slip systems. Therefore, some researchers tried to simplify the model into the two-dimensional method which looks directly at the motion of the dislocations in slip planes [34,96,102–104]. They eliminated the rest of the three dimensional shape of the structure which has less effects on dislocation motions [34]. Changing from three-dimensional simulation to two-dimensional model reduces the computational costs while the prediction of plasticity behavior is still accurate [96].

In addition to dislocation plasticity, phase transformation is another significant deformation mechanism in shape memory alloys. Due to the larger values of transformation strain in comparison to the plastic strain, many researchers considered only phase transformation as the nonlinear deformation process and ignored the plastic behavior of SMAs. Ezaz et al. [105] showed that the slip planes in BCC structure of austenitic NiTi are active, therefore the transformation and plasticity may affect each other and also the total mechanical behavior of shape memory alloy. Shi et al [35, 106] used the discrete dislocation dynamic method for modeling plasticity and the discrete transformation method to model the phase transformation in TRIP steel. Although they model the effects of phase transformation on dislocation plasticity in TRIP steels, they did not model the two-way phase transformation which occurs in SMAs. Furthermore, their model was unable to include temperature effects and thermal cycling as important

factors that affect the response of SMAs.

Recently, Kundin et al. [107,108] developed a three-dimensional microelastic-plastic phase field model to study the incoherent transformation and plastic accommodation and relaxation. They have improved the classical phase field model of a micro-elastic case by adding the nucleation and accommodation of dislocations in austenitic phase and their effect on martensitic transformation. Although their model does not include the gliding and motion of the dislocations in the microstructure, calculating dislocation densities and elastic energy fields of dislocations are significant parts of their study that allow them to present the model for three-dimensional cases.

2.3.2 Continuum macro-scale model

As discussed in previous section, the discrete dislocation-transformation method simulates the mechanical behavior of SMAs by considering the physical phenomena in the microstructure. Therefore, it gives a good physical view about the deformation mechanisms in SMAs. However, it is not computationally possible to model a real three dimensional component with this method. To have a more useful model for macro-scale applications, the continuum method is applied to model the plasticity and the phase transformation.

Continuum modeling of the shape memory effect and pseudoelasticity

has been the subject of many researches. There are many phenomenological models that simulate the stress-induced and temperature-induced transformation without effect of plastic deformations [109–114]. However, they just assumed the phase transformation to be the main deformation mechanism and they did not consider the plastic behavior in the models. Also, the importance of irrecoverable strain in shape memory alloys attracted many works to include the phenomenological modeling of plasticity for SMAs. Tanaka et al. [115] studied the instability of SMAs under thermal and mechanical loading. Bo and Lagoudas [22] was one of the first studies that considered plastic deformation during superelasticity behavior at the continuum level. Thereafter, many other phenomenological models are proposed for plasticity of SMAs under thermo-mechanical cyclic loadings [23, 116–122].

Further investigations on the mechanism of plasticity in TRIP steel and SMAs showed that extra dislocation slip is induced by martensitic transformation in these materials. It is called the transformation-induced plasticity or TRIP strain [20]. Due to the larger number of applications of steel in the industry in comparison to SMAs, the first studies and phenomenological modeling of TRIP have been done on steel [19, 123–125]. However, the phenomenological relations to model the TRIP strain in ductile material including SMAs are presented in [126–128].

Finally, the continuum investigations of the interaction between plas-

ticity and phase transformation in SMAs are divided to two groups. In the first group, the continuum model of the interaction between plasticity and phase transformation is applied by considering the redistribution of stress field due to the phase transformation [30, 129]. In the second group, researchers represented phenomenological equations to include the effects of dislocations on martensitic generations [130–132]. Manchiraju and Anderson recently have presented a micromechanics finite element study on the interaction between phase transformation and plasticity [133, 134].

In the following chapters, the discrete dislcoation-transformation method is presented and then the single crystal and polycrystal NiTi is simulated under thermo-mechanical loading. Finally the phenomenological constitutive model and the simulations of macro-scale samples are presented in Chapter 6.

Chapter 3

Two-dimensional discrete dislocation-transformation method

An overview of the discrete dislocation-transformation method and the assumptions that are made during the implementation process are presented in this chapter. The discrete dislocation-transformation model is applied to simulate the interaction between dislocation slip plasticity and martensitic transformation in shape memory alloys (SMAs) under thermo-mechanical loading.

3.1 Discrete dislocation-transformation

The discrete dislocation-transformation model is developed by combining the discrete-dislocation method and the theory of martensitic transformation in the micro-structure. The first mechanism is applied to model the plastic deformation in the microstructure. Next, the discrete-transformation method is used to simulate the martensitic transformation at the same modeling scale of the discrete dislocation method. The region is assumed to be linear elastic that occupies Ω with boundary $\partial\Omega$. The domain is initially in a stress-free and dislocation-free austenitic phase with random dislocation and transformation sources. Then, the specimen is subjected to prescribed displacement and traction as

$$\begin{cases} \mathbf{u}_0 = \mathbf{u}_0(\mathbf{x}, t) & \text{on} \quad \partial\Omega_u, \\ \mathbf{t}_0 = \mathbf{t}_0(\mathbf{x}, t) & \text{on} \quad \partial\Omega_t, \end{cases} \tag{3.1}$$

where $\partial\Omega_u$ and $\partial\Omega_t$ denotes the part of boundary that prescribed displacement and traction are applied, respectively. The deformation process is assumed to be quasi-static which involves small strain. Therefore, an equilibrium problem is solved in each time step. Moreover, the dislocations are line defects which are nucleated and moved in the elastic domain. Furthermore, the transformed (martensitic) regions are assumed to nucleate and grow as elliptical-shaped inclusions during thermo-mechanical loading

process. The dislocation density and martensitic volume fraction at a given time are defined by $\rho^d(t) = \frac{N^d(t)}{\Omega}$ and $\zeta(t) = \frac{\sum_{i=1}^{k} \Omega_i^m}{\Omega}$, respectively, where $N^d(t)$ is the total number of dislocations and $\sum_{i=1}^{k} \Omega_i^m$ is the total area of martensitic region at time t.

In the current discrete dislocation-transformation method, the analysis of deformation mechanisms at time t consists of three computational stages. In the first step, the stress, strain and displacement fields are found for the current configuration of dislocations arrangement and martensitic inclusions. Then, the Peach–Koehler force (driving force for each dislocation) and driving force for martensitic transformation interfaces are calculated. Finally, the change of dislocations structure and martensitic plates are determined by defining the constitutive equations for the nucleation, motion and annihilation of dislocations, and the nucleation, growth and annihilation (in reverse transformation) of the martensitic plates.

The stress, strain and displacement states of a configuration including dislocations and martensitic plates under prescribed boundary conditions are computed with the decomposition method presented in [34,35]. Therefore, the problem is decomposed into three sub-problems: (i) dislocations in an infinite elastic medium, (ii) martensitic regions as inclusions in an infinite medium, and (iii) a complementary problem in the finite medium to satisfy the applied boundary conditions. Therefore, the stress, strain, and displacement fields of the total problem can be mathematically written

as

$$\begin{cases} \boldsymbol{\sigma} = \boldsymbol{\sigma}^d + \boldsymbol{\sigma}^m + \boldsymbol{\sigma}^c, \\ \boldsymbol{\varepsilon} = \boldsymbol{\varepsilon}^d + \boldsymbol{\varepsilon}^m + \boldsymbol{\varepsilon}^c, \\ \boldsymbol{u} = \boldsymbol{u}^d + \boldsymbol{u}^m + \boldsymbol{u}^c, \end{cases} \tag{3.2}$$

where all the parameters with d, m, and c superscripts show the fields due to the dislocations, martensitic plates, and the complementary problem, respectively. The schematic of the above decomposition is illustrated in Figure 3.1.

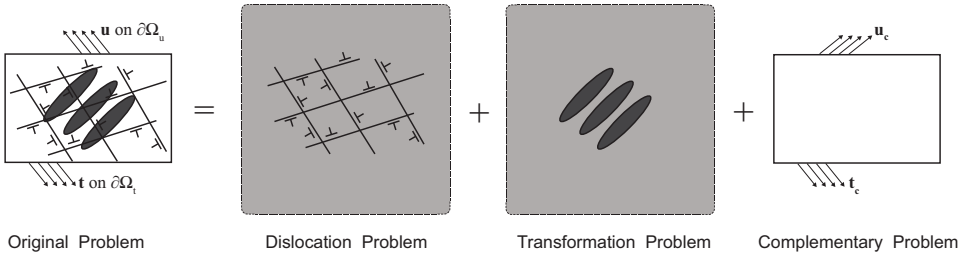

Figure 3.1: Dividing the problem into three sub-problems: interacting dislocations in infinite region, martensitic inclusions in infinite medium, and complementary problem.

If there are N^d numbers of dislocations and N^m numbers of martensitic inclusions in the medium at time t, the fields in equation (3.2) are written as a summation of states from each individual dislocations and martensitic regions as

$$\begin{cases} \boldsymbol{\sigma}^d = \sum_{i=1}^{N^d} \boldsymbol{\sigma}_i^d, \\ \boldsymbol{\varepsilon}^d = \sum_{i=1}^{N^d} \boldsymbol{\varepsilon}_i^d, \\ \boldsymbol{u}^d = \sum_{i=1}^{N^d} \boldsymbol{u}_i^d, \end{cases} \tag{3.3}$$

$$\begin{cases} \boldsymbol{\sigma}^m = \sum_{j=1}^{N^m} \boldsymbol{\sigma}_j^m, \\ \boldsymbol{\varepsilon}^m = \sum_{j=1}^{N^m} \boldsymbol{\varepsilon}_j^m, \\ \boldsymbol{u}^m = \sum_{j=1}^{N^m} \boldsymbol{u}_j^m, \end{cases} \tag{3.4}$$

where i and j subscripts determine the individual dislocations and martensitic regions, respectively. It is worth mentioning that all above terms (dislocations and transformations fields) are determined analytically in infinite medium. This is followed by numerical solution of complementary problem to satisfy boundary conditions of the original finite domain.

3.1.1 Fields due to the dislocations

The focus in this study is on the two-dimensional plane-strain problem with edge dislocations in an infinite, isotropic and homogeneous domain, where the line direction of dislocations is perpendicular to the plane of deformation. Furthermore, each dislocation core is a singular point; therefore, all fields are computed analytically outside of the dislocation core as mentioned in [34].

It is assumed that the Burgers vector $\mathbf{b}^i$ of each dislocation is represented in the x direction and the slip plane normal is assumed in the y direction. Therefore, as it is illustrated schematically in Figure 3.2, for each point positioned at (X, Y) in the plane, the displacement and stress

fields due to the dislocation i positioned at (X^i, Y^i) are given by [91,92] as

$$\boldsymbol{u}_i^d(x,y) = \begin{pmatrix} u_i^d \\ v_i^d \end{pmatrix} = \begin{pmatrix} \frac{b^i}{2\pi(1-\nu)}\{\frac{1}{2}\frac{\Delta x\Delta y}{(\Delta x)^2+(\Delta y)^2} - (1-\nu)\tan^{-1}(\frac{\Delta x}{\Delta y})\} \\ \frac{b^i}{2\pi(1-\nu)}\{\frac{1}{2}\frac{(\Delta y)^2}{(\Delta x)^2+(\Delta y)^2} - \frac{1}{4}(1-2\nu)\ln\frac{(\Delta x)^2+(\Delta y)^2}{(b^i)^2}\} \end{pmatrix}, \tag{3.5}$$

$$\begin{cases} \boldsymbol{\sigma}_i^d|_{xx} = -\frac{\mu b^i}{2\pi(1-\nu)}\frac{\Delta y[3(\Delta x)^2+(\Delta y)^2]}{[(\Delta x)^2+(\Delta y)^2]^2}, \\ \boldsymbol{\sigma}_i^d|_{yy} = \frac{\mu b^i}{2\pi(1-\nu)}\frac{\Delta y[(\Delta x)^2-(\Delta y)^2]}{[(\Delta x)^2+(\Delta y)^2]^2}, \\ \boldsymbol{\sigma}_i^d|_{xy} = \frac{\mu b^i}{2\pi(1-\nu)}\frac{\Delta x[(\Delta x)^2-(\Delta y)^2]}{[(\Delta x)^2+(\Delta y)^2]^2}, \end{cases} \tag{3.6}$$

where $\boldsymbol{\sigma}_i|_{xx}$, $\boldsymbol{\sigma}_i|_{yy}$, and $\boldsymbol{\sigma}_i|_{xy}$ are in-plane stress field components, $\Delta x = X - X^i$, and $\Delta y = Y - Y^i$.

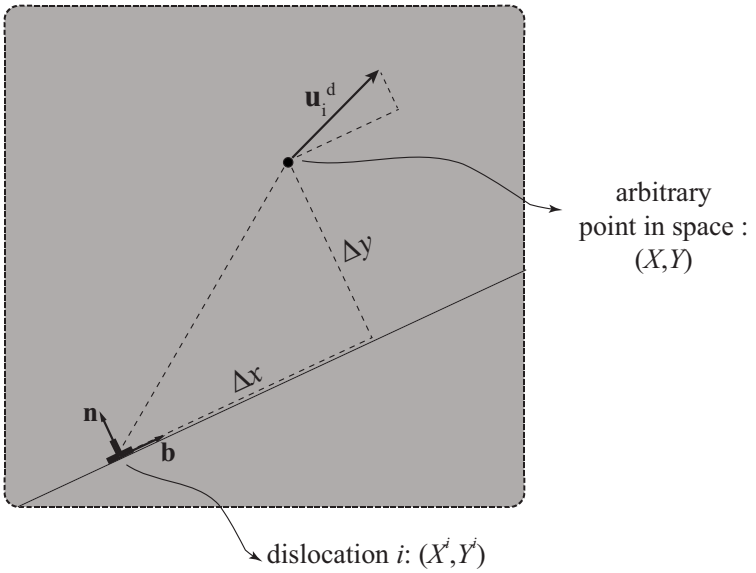

Figure 3.2: Schematic of displacement field at each point due to the dislocation i.

In this study, it is also considered that the Burgers vector of dislocations in the austenite and martensite regions are the same; therefore, the constitutive relation for stress and strain fields of dislocations depends only

on the location of dislocations and it is expressed as

$$\boldsymbol{\sigma}_i^d := \begin{cases} \mathbb{C}^a \boldsymbol{\varepsilon}_i^d & \text{for} \quad i \in A^a, \\ \mathbb{C}^m \boldsymbol{\varepsilon}_i^d & \text{for} \quad i \in A^m, \end{cases} \tag{3.7}$$

where $\mathbb{C}^a$ and $\mathbb{C}^m$ are fourth-order stiffness tensors of austenite and martensite phases and A^a and A^m are the set of dislocations in the austenite and martensitic regions, respectively.

3.1.2 Fields due to the martensitic area

According to equations (3.4), the stress, strain, and displacement fields due to the martensitic regions in infinite domain are the summation of fields for each individual jth region. Based on the physical observation [135–137] and work by Shi. et al. [35], it is considered here that each martensitic region is an elliptical shape under constrained condition. Each jth martensitic ellipse occupies Ω_j^m in an infinite medium with stiffness tensor $\mathbb{C}^m$. The rest of domain $(\mathbb{R}^2 - \Omega_j^m)$ is in austenite phase with stiffness tensor $\mathbb{C}^a$. For isotropic-elastic cases

$$\mathbb{C}_p = \frac{1}{3}(3\kappa^p - 2\mu^p)\mathbf{I} \otimes \mathbf{I} + 2\mu^p \mathbb{I}, \tag{3.8}$$

where κ^p and μ^p are bulk and shear modulus of phase p, respectively, where p may be $p = a$ or $p = m$ for austenitic and martensitic phases. Further-

more, $\mathbf{I}$ and $\mathbb{I}$ are second and fourth order identity tensors.

The martensitic phase transformation is the change of crystallography from the parent phase (austenite) to the product phase (martensite). This transformation is from the body center cubic (BCC) structure in austenite to twin related monoclinic in martensite for NiTi shape memory alloy. There are 192 possible transformation systems under the unconstrained condition, including the different variants of twins for austenite→monoclinic transformation. Each transformation system is characterized by a pair of vectors $\boldsymbol{a}$ and $\boldsymbol{m}$, where $\boldsymbol{a}$ is the transformation strain vector and $\boldsymbol{m}$ is the habit plane normal [138] that is normal to the austenite-martensite interface. The schematic of unconstrained phase transformation is shown in Figure 3.3a.

From the theory of martensitic phase transformation [138, 139], the change in crystal structure under unconstrained and small strain conditions is described by transformation strain and it is expressed as

$$\boldsymbol{\varepsilon}^{tr} := \frac{1}{2}(\boldsymbol{a} \otimes \boldsymbol{m} + \boldsymbol{m} \otimes \boldsymbol{a}). \tag{3.9}$$

In this study the specimen is assumed in plane-strain. Therefore, both dislocation motion and phase transformation occur in a plane with normal vector $[-1 \quad 0 \quad 1]$. Only, two transformation systems of all 192 possible systems which are of common occurrence in experiments are assumed to

be representative of transformation systems. Although these two systems are not in the loaded plane, to keep the problem consistent with plane-strain condition, it is considered that the transformation systems lie in the loaded plane similar to the slip planes. This keeps the transformation problem consistent with the plane-strain condition and also the dislocation dynamics problem.

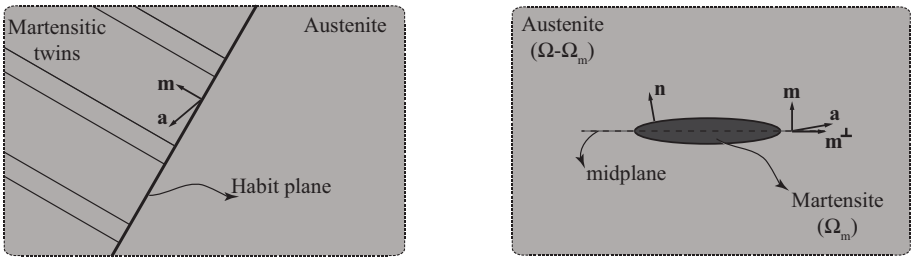

(a) (b)

Figure 3.3: Schematic diagram of unconstrained and constrained austenite-twinned martensite structure: (a) Unconstrained phase transformation, and (b) Constrained phase transformation.

As it is mentioned before, the cross section of the martensitic region is considered as an elliptical shape under constrained condition. The schematic of constrained martensitic phase and transformation systems is shown in Figure 3.3b. As can be seen in the Figure 3.3b, the habit-plane normal is changing around the ellipse surface. In this study, the transformation systems of unconstrained case are used as the eigen-strain of martensitic inclusions. Furthermore, the habit-plane normal $\vec{\boldsymbol{n}}$ in the constrained case is applied as the normal of the martensite-austenite interface at each point on the interface.

The transformation strain of jth martensitic plate consists of a dilation term with magnitude δ in the direction of the normal $\vec{\boldsymbol{n}}$ and a shape strain term with magnitude of γ in the direction perpendicular to the unconstrained habit plane normal $\vec{\boldsymbol{m}}$. Therefore, $\delta = \boldsymbol{a}_j \cdot \boldsymbol{m}_j$ and $\gamma = \boldsymbol{a}_j \cdot \boldsymbol{m}_j^{\perp}$ and the in-plane transformation strain is reformulated as

$$\boldsymbol{\varepsilon}_j^{tr} := \frac{1}{2}\gamma(\boldsymbol{m}_j^{\perp} \otimes \boldsymbol{m} + \boldsymbol{m} \otimes \boldsymbol{m}_j^{\perp}) + \delta(\boldsymbol{m}_j \otimes \boldsymbol{m}_j), \tag{3.10}$$

where $\boldsymbol{m}_j$ is the unit vector oriented perpendicular to the major semi-axis of ellipse and $\boldsymbol{m}_j^{\perp}$ is a unit vector parallel to major semi axis of ellipse, as shown in Figure 3.3b.

By considering the martensitic regions as elliptical inclusions, the stress field $\boldsymbol{\sigma}_j^m$ inside and outside of martensitic region is calculated by the eigen-strain of inclusion. The eigen-strain is due to the transformation strain and the difference between elastic behavior of martensitic and austenitic phases. Therefore, the eigen-strain is uniform as the transformation strain is uniform. The described fields can be calculated according to Eshelby solution using the equivalent inclusion method [140, 141]. For brevity, the stress and strain fields of martensitic inclusion are presented here and the complete analytical solution is elaborated in the Appendix B.

The constitutive relations between stress and strain both inside and

outside of the jth inclusion with eigen-strain equal to $\boldsymbol{\varepsilon}_j^m$ are expressed as

$$\boldsymbol{\sigma}_j^m := \begin{cases} \mathbb{C}^a \boldsymbol{\varepsilon}_j^m & \text{in} \quad \mathbb{R}^2 - \Omega_j^m, \\ \mathbb{C}^m (\boldsymbol{\varepsilon}_j^m - \boldsymbol{\varepsilon}_j^{tr}) & \text{in} \quad \Omega_j^m. \end{cases} \tag{3.11}$$

For the interior points of the jth martensitic inclusion, it can be shown that

$$\begin{cases} \boldsymbol{\varepsilon}_j^m = \mathbb{S}[(\mathbb{C}^m - \mathbb{C}^a)\mathbb{S} + \mathbb{C}^a]^{-1}\mathbb{C}^m \boldsymbol{\varepsilon}_j^{tr} & \text{in} \quad \Omega_j^m, \\ \boldsymbol{\sigma}_j^m = \mathbb{C}^a(\mathbb{S} - \mathbb{I})[(\mathbb{C}^m - \mathbb{C}^a)\mathbb{S} + \mathbb{C}^a]^{-1}\mathbb{C}^m \boldsymbol{\varepsilon}_j^{tr} & \text{in} \quad \Omega_j^m, \end{cases} \tag{3.12}$$

where $\mathbb{S}$ is the fourth order Eshelby's tensor for interior points [141]. To calculate the fields for the exterior points, the analytical solution is explained in Appendix B. However, the decomposition method that is suggested by Tanaka and Mura [142] is applied here to calculate the fields at exterior points of martensitic zone.

According to Tanaka and Mura [142], the uniform stress field $\boldsymbol{\sigma}_{in}$ for the interior points is found first. Then, the problem is decomposed into two separate problems: (i) a stress free void case with the stress equal to $-\boldsymbol{\sigma}_{in}$ at infinity, and (ii) a uniform domain without void or inclusion where stress is $\boldsymbol{\sigma}_{in}$ at infinity. The schematic of this decomposition is illustrated in Figure 3.4. The first problem is a void case which is solved by the Mushkelishvili's potentials. Therefore, if the stress field at the interior

points of the inclusion is $\boldsymbol{\sigma}_{in} = \mathbb{C}^a(\mathbb{S} - \mathbb{I})[(\mathbb{C}^m - \mathbb{C}^a)\mathbb{S} + \mathbb{C}^a]^{-1}\mathbb{C}^m\boldsymbol{\varepsilon}_j^{tr}$, and the solution of stress field for the void problem is $\boldsymbol{\sigma}^v$, then the total stress field for exterior points is expressed as

$$\boldsymbol{\sigma}_j^m = \boldsymbol{\sigma}_{in} + \boldsymbol{\sigma}^v \qquad \text{in} \qquad \mathbb{R}^2 - \Omega_j^m. \tag{3.13}$$

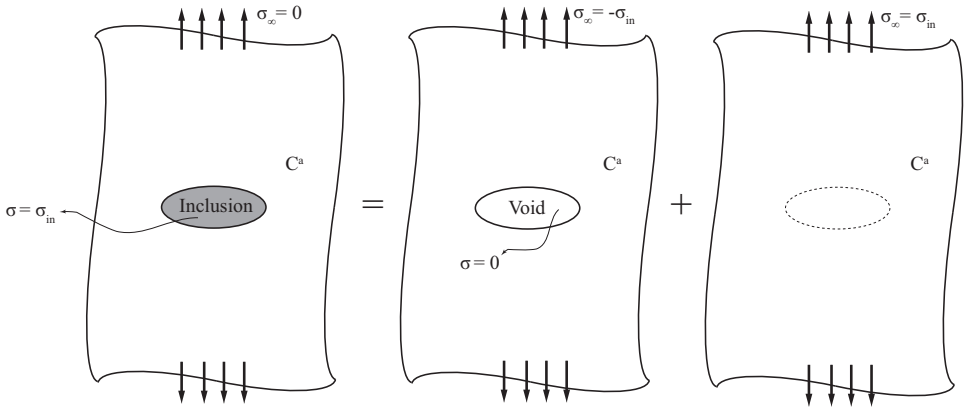

Figure 3.4: Schematic for the decomposition problem to find the stress field of exterior points.

3.1.3 Complementary fields

As it is illustrated in Figure 3.1 and discussed in the previous sections, the complementary field is added to the decomposition problem to satisfy the original boundary conditions of the domain and the inhomogeneity of martensitic areas. The procedure is explained by Shi et al. [35] and it is described as follows:

The equilibrium outside of dislocation cores states that

$$div\boldsymbol{\sigma} = \mathbf{0} \qquad \text{in} \qquad \Omega^*, \tag{3.14}$$

where the stress-strain-displacement relations in linear, homogeneous, and elastic domain are

$$\begin{cases} \boldsymbol{\sigma} = \begin{cases} \mathbb{C}^a\boldsymbol{\varepsilon} & \text{in} \quad \Omega^{a*}, \\ \mathbb{C}^m(\boldsymbol{\varepsilon} - \boldsymbol{\varepsilon}_j^{tr}) & \text{in} \quad \Omega_j^{m*}, \quad j = 1, ..., N^m, \end{cases} \\ \boldsymbol{\varepsilon} = \frac{1}{2}(\bigtriangledown \boldsymbol{u} + \bigtriangledown \boldsymbol{u}^T) \qquad \text{in} \qquad \Omega^*, \end{cases} \tag{3.15}$$

where the star superscript domains (*) indicate the domains excluding the dislocation cores. Thus according to the decomposition (3.2), the complementary field is stated as:

$$div\boldsymbol{\sigma}^c = \mathbf{0} \qquad \text{in} \qquad \Omega^*, \tag{3.16}$$

$$\begin{cases} \boldsymbol{\sigma}^c = \begin{cases} \mathbb{C}^a\boldsymbol{\varepsilon}^c + \boldsymbol{P}_a^d & \text{in} \quad \Omega^{a*}, \\ \mathbb{C}^m\boldsymbol{\varepsilon}^c + \boldsymbol{P}_j^m + \boldsymbol{P}_j^d & \text{in} \quad \Omega_j^{m*}, \quad j = 1, ..., N^m, \end{cases} \\ \boldsymbol{\varepsilon}^c = \frac{1}{2}(\bigtriangledown \boldsymbol{u}^c + (\bigtriangledown \boldsymbol{u}^c)^T) \qquad \text{in} \qquad \Omega^*, \end{cases} \tag{3.17}$$

where $\boldsymbol{P}_a^d$, $\boldsymbol{P}_j^m$, and $\boldsymbol{P}_j^d$ are polarization stresses to correct the stress field of dislocations and inclusions due to the difference in elastic properties

between the austenite and martensite. They are formulated according to [35] as

$$\begin{cases} \boldsymbol{P}_a^d := (\mathbb{C}^a - \mathbb{C}^m) \sum\limits_{j \in A^m} \boldsymbol{\varepsilon}_j^d & \text{in} \quad \Omega^{a*}, \\ \boldsymbol{P}_j^m := (\mathbb{C}^m - \mathbb{C}^a) \sum\limits_{l=1, l \neq j}^{N^m} \boldsymbol{\varepsilon}_l^m & \text{in} \quad \Omega^{m*}, \quad j = 1, ..., N^m, \\ \boldsymbol{P}_j^d := (\mathbb{C}^m - \mathbb{C}^a) \sum\limits_{j \in A^m} \boldsymbol{\varepsilon}_j^m & \text{in} \quad \Omega^{m*}, \quad j = 1, ..., N^m, \end{cases} \tag{3.18}$$

where A^a and A^m indicate the set of dislocations in the austenite and martensitic regions. It is clear that if the austenitic and martensitic phases have the same elastic properties, all the polarization stresses in the equation (3.17) will be zero.

The boundary conditions for complementary problem based on decomposition (3.2) are

$$\begin{cases} \boldsymbol{u}^c := \boldsymbol{u}_0 - \boldsymbol{u}^d - \boldsymbol{u}^m & \text{on} \quad \partial\Omega_u, \\ \boldsymbol{t}^c := \boldsymbol{t}_0 - \boldsymbol{t}^d - \boldsymbol{t}^m & \text{on} \quad \partial\Omega_t, \end{cases} \tag{3.19}$$

where $\boldsymbol{t}^c = \boldsymbol{\sigma}^c \boldsymbol{n}$, $\boldsymbol{t}^d = \boldsymbol{\sigma}^d \boldsymbol{n}$, $\boldsymbol{t}^m = \boldsymbol{\sigma}^m \boldsymbol{n}$ and $\boldsymbol{n}$ is the outward unit vector normal to $\partial\Omega$.

The above linear elastic boundary value problem is solved numerically in each time step. Generally to consider inhomogeneity in finite element implementation, it is necessary to assign austenite and martensite stiffness

to specific elements and re-mesh the domain at each time step. However, if the stiffnesses of austenite and martensite are equal then the polarization stresses vanish. In this study, as the main objective is to see the interaction between transformation and plasticity, the inhomogeneity plays a very small role in comparison to transformation strain. Therefore, the difference between austenite and martensite stiffness is neglected in this study.

3.2 Two dimensional dislocation dynamic

The nucleation and motion of dislocations in the microstructure are the main mechanisms for plastic deformation in crystalline metals. In the last decades, many research has been done to model the plasticity mechanism by studying the dynamic behavior of dislocations [33, 143, 144]. Van der Giessen and Needleman [34] presented the two dimensional plane strain discrete dislocation method. The loading plane in the model is the plane which contains the slip lines and edge dislocations. Furthermore, the constitutive rules for nucleation, motion, pinning, and annihilation of dislocations were explained.

In this work, the model presented by Van Der Giessen in [34] is followed. The domain is considered as a two dimensional plane-strain region with edge dislocations as line singularities. The dislocation loops are modeled as edge dipoles and are restricted to glide in the slip planes and along slip directions. Furthermore, in some steps, dislocation dynamics occur

with martensitic phase transformation. Therefore, some assumptions are taken in the current study. The dislocation sources in martensite region are deactivated, and dislocations in martensite regions are frozen (because there is no significant observation on dislocation plasticity in martensite).

The gliding of ith dislocation with $i = 1, \ldots, N^d$, characterized by slip plane normal $\boldsymbol{n}_i$ and burgers vector $\boldsymbol{b}_i$, is determined by Peach-Koehler force, f_i^d. Peach-Koehler force is the force conjugate to the motion of dislocations that changes the potential energy of the body Ω. The Peach-Koehler force is defined as the shear component of the total stress field at the ith dislocation position excluding the singular stress $\boldsymbol{\sigma}_i^d$ of the ith dislocation on the slip system $\boldsymbol{b}_i, \boldsymbol{n}_i$:

$$f_i^d := (\boldsymbol{\sigma} - \boldsymbol{\sigma}_i^d) \cdot (\boldsymbol{b}_i \otimes \boldsymbol{n}_i). \tag{3.20}$$

The evolution of dislocation structure during deformation process is presented as (i) nucleation of dislocation pairs from discrete sources, (ii) motion of dislocations along slip planes, (iii) pinning of the dislocations at obstacles, and (iv) annihilation of dislocations with opposite sign. Each of these processes are formulated based on the [34].

3.2.1 Dislocation nucleation

New dislocation dipoles are generated through the operation of two dimensional Frank-Read sources which are random discrete source points in the domain. When magnitude of Peach-Koehler force at the ith source point exceeds a critical value (f_i^{cr}) during a time period (t_{nuc}), two dislocations with opposite Burgers vector are generated. The above situation can be formulated as

$$\frac{1}{t_{nuc}} \int_t^{t+t_{nuc}} |f_i^d| dt \geq f_i^{cr}. \tag{3.21}$$

The schematic of two dimensional dislocation nucleation is illustrated in Figure 3.5 [34]. The distance between the two new dislocations is defined as it grantees that the resolved shear stress on each of them balances the attractive shear stress that two dislocations exert on each other. Therefore, based on the calculation presented in [34]

$$L_{nuc} = \frac{\mu}{2\pi(1-\nu)} \frac{b_i}{\tau_i^{cr}}, \tag{3.22}$$

where $\tau_i^{cr} := \frac{f_i^{cr}}{b_i}$ is the critical resolved shear stress and $b_i := \boldsymbol{b}_i \cdot \boldsymbol{n}_i$ is the magnitude of Burgers vector $\boldsymbol{b}_i$.

3.2.2 Dislocation gliding, pinning and annihilation

The motion of ith dislocation is controlled by Peach-Koehler force that is calculated in equation (3.20). Thus, the kinetic relation for gliding of the

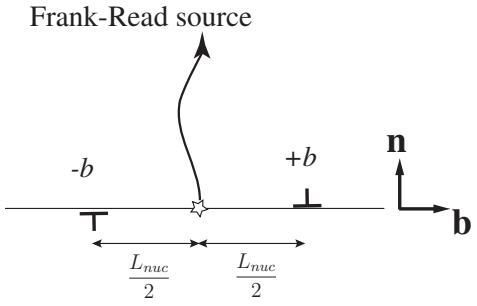

Figure 3.5: Schematic of two dimensional dislocation generation from Frank-Read sources.

ith dislocation can be written as

$$\begin{cases} v_i^d = \frac{f_i^d}{B_d}, & \text{if} \quad 0 \leq |v_i^d| \leq v_{max}^d, \\ v_i^d = v_{max}^d & \text{if} \quad |v_i^d| > v_{max}^d, \end{cases} \tag{3.23}$$

where B_d is a drag coefficient which is mainly from phonon drag in metallic microstructures. v_i^d is the velocity of ith dislocation along slip plane, and v_{max}^d is a cut-off value for the dislocation velocity. The motion of dislocation in reality is affected by the types of obstacles. In two-dimensions, it is modeled by putting random obstacles with obstacles' strength τ_{obs} and the pinned dislocations at obstacles can be released if the resolved shear stress exceeds the τ_{obs}.

The dislocations of opposite Burgers' vectors in the same slip plane may annihilated each other if they come close to each other. In the two dimensional model, the annihilation occurs when the distance between two opposite singed dislocations is less than a material-dependent distance (L_e)

that is assumed as $L_e = 6b_i$ (the same value that Van der Giessen assumed in [34]).

3.3 Transformation kinetic

The configuration of phase transformation at the time $(t + \Delta t)$ will be updated based on the field state at the time (t). The method that is described here is based on the two dimensional discrete transformation for nucleation and growth of the martensitic regions that was presented in [35] for phase transformation in TRIP steels. However that model has the restriction on modeling the reverse transformation in SMAs. The other limitation is that it just worked under mechanical loads. Therefore, the following model explains diminishing and elimination of martensitic region in the backward transformation (martensite→austenite), as well as nucleation and growth of martensitic region in the forward transformation (austenite→martensite) under thermo-mechanical loading.

Abeyaratne and Knowles [145, 146] presented the formulation to find the local driving force on austenite/martensite interface. The driving force caused the forward or backward phase transformation. This framework is used here to calculate the driving force on the interface.

If a martensitic region Ω_j^m is considered to be surrounded by austenitic domain with boundary surface S_j^m between them together with the small deformation consideration, the transformation driving force on each point

on S_j^m is given by

$$f_j^{tr} := \rho[\![\psi]\!] - \langle \boldsymbol{\sigma} \rangle \boldsymbol{n} \cdot [\![\boldsymbol{\varepsilon}]\!] \boldsymbol{n}, \tag{3.24}$$

where ρ is the mass density and ψ is the Helmholtz free energy per unit mass. $[\![\ \ ]\!]$ sign shows the jump between the austenitic and martensitic phases at the interface (S_j^m). Therefore, $[\![\psi]\!] := \psi^a - \psi^m$ is the jump of Helmholtz free energy between austenite and martensite phases and $[\![\boldsymbol{\varepsilon}]\!] := \boldsymbol{\varepsilon}^+ - \boldsymbol{\varepsilon}^-$ is the jump of strain across the austenite-martensite interface. Furthermore, $\langle \boldsymbol{\sigma} \rangle := \frac{1}{2}(\boldsymbol{\sigma}^+ + \boldsymbol{\sigma}^-)$ is the average of stress across the interface.

Although the stress and strain fields are not continuous across the interface ($\boldsymbol{\sigma}^+ \neq \boldsymbol{\sigma}^-$ and $\boldsymbol{\varepsilon}^+ \neq \boldsymbol{\varepsilon}^-$), the displacement field and traction vector are continuous across the interface S_j^m ($u^+ = u^-$ and $\boldsymbol{\sigma}^+ \boldsymbol{n} = \boldsymbol{\sigma}^- \boldsymbol{n}$). As the elastic strains on both sides of the interface are small, the jump in strain tensor is estimated to the negative of transformation strain

$$[\![\boldsymbol{\varepsilon}]\!] \approx -\boldsymbol{\varepsilon}_{\boldsymbol{j}}^{\boldsymbol{tr}}. \tag{3.25}$$

Finally, during thermo-mechanical loading, according to Shi et al. [35] and [145–147], the local transformation driving force is expressed as

$$f_j^{tr} = \boldsymbol{\sigma}^{\pm} \boldsymbol{n} \cdot \boldsymbol{\varepsilon}_j^{tr} \boldsymbol{n} + \frac{1}{2} \mathbb{D}^a \boldsymbol{\sigma}^+ \cdot \boldsymbol{\sigma}^+ - \frac{1}{2} \mathbb{D}^m \boldsymbol{\sigma}^- \cdot \boldsymbol{\sigma}^- - \frac{\rho \lambda}{\theta_T} (\theta - \theta_T), \tag{3.26}$$

where $\boldsymbol{\sigma}$ is the local stress tensor, θ is temperature, λ is transformation latent heat, and θ_T is so called transformation temperature and is defined as $\theta_T := (A_s + M_s)/2$. A_s and M_s are temperatures where the material starts to transform to austenite and marensite phases, respectively. It is worth mentioning that as the martensitic region is in elliptical shape, the curvature of the interface, and the actual habit plane normal $\boldsymbol{n}$ are used.

3.3.1 Nucleation of martensitic regions in forward transformation

The new martensitic regions are generated from the random transformation source points in the different transformation systems. The transformation driving force for the jth source point is defined according to equation (3.26)

$$f_j^{nuc} = \boldsymbol{\sigma} \cdot \boldsymbol{\varepsilon}_j^{tr} - \frac{\rho\lambda}{\theta_T}(\theta - \theta_T). \tag{3.27}$$

Clearly, the martensitic nucleation occurs at the source j when the nucleation driving force exceeds a local critical value (f_j^{cr})

$$f_j^{nuc} \geq f_j^{cr}. \tag{3.28}$$

When the above condition is satisfied, an elliptical embryo with semi-axes c_0 and d_0 is generated in the domain and the source j will be deleted.

3.3.2 Growth and shrinkage of martensitic regions in forward and backward transformation

The method to model the growth of martensitic transformation in this study is the modification of the method presented in [35]. Here, the reverse phase transformation rules with negative driving forces are added. The growth and shrinkage of the elliptical martensitic regions are modeled by defining the velocity of tips of the ellipse. Furthermore, without reducing from the physical meaning of the transformation, it is assumed that the aspect ratio of ellipses during transformation is constant ($e := \frac{d}{c}$=constant).

In general the constitutive relation between value of transformation driving force ($f_j^{tr}(x)$) around S_j^m defines the normal velocity ($V_n(x)$) of each point on the interface. However, this constitutive assumption cannot always keep the martensitic region in elliptical geometry. Therefore, the effective values at the tips are considered for the ellipse evolution equation by satisfying the following conditions: (i) the total dissipation of point-wise growth relation be the same as effective driving force growth, (ii) the aspect ratio of ellipse is kept constant. The schematic of elliptical martensite regions and the martensitic growth which is modeled here is illustrated in Figure 3.6.

If $\mathscr{D}_j^q$ is the total dissipation due to the transformation when the tip (q)

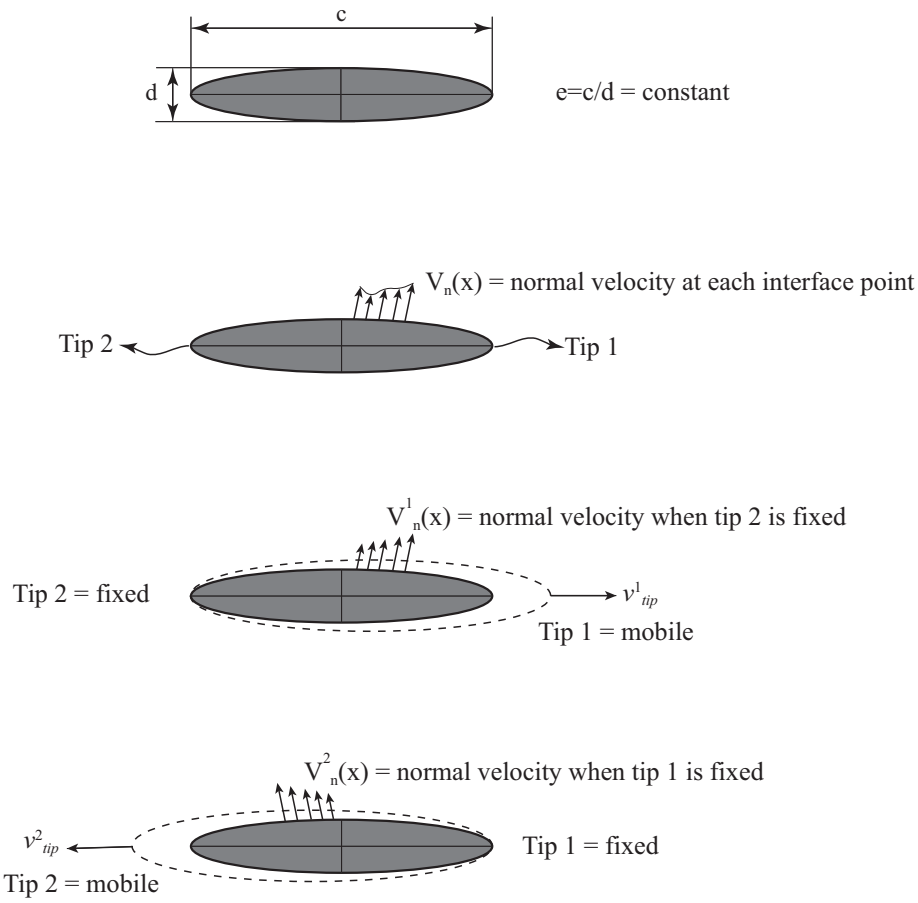

Figure 3.6: The schematic of the growth of elliptical martensitic regions.

moves and the opposite tip is held fixed

$$\mathscr{D}_j^q = \int_{S_j} f_j^{tr} V_n^{(q)} ds, \tag{3.29}$$

where $V_n^{(q)} = V_n^{(q)}(x)$ is normal velocity in each point at austenite/martensite interface and $q = 1, 2$. The $V_n^{(q)}(x)$ is reformulated as

$$V_n^{(q)} = w^{(q)} v_{tip}^{(q)}, \tag{3.30}$$

where $v_{tip}^{(1)}$ and $v_{tip}^{(2)}$ are velocity of tips 1 and 2 when the opposite one is kept fixed, and $w^{(1)}$ and $w^{(2)}$ are weighting functions independent of $v_{tip}^{(1)}$ and $v_{tip}^{(2)}$. The weighting functions connect the distribution of the normal velocity on the interface to velocity of the tips. The value of $w^{(q)}$ is 1 at tip q and zero in the opposite tip. Then from equations (3.29) and (3.30)

$$\mathscr{D}_j^q = \int_{S_j} f_j^{tr} w^{(q)} v_{tip}^{(q)} ds = \left(\int_{S_j} f_j^{tr} w^{(q)} ds \right) v_{tip}^{(q)}. \tag{3.31}$$

Then, it is supposed that the normal velocity on the interface and the driving force has a linear relation as

$$B f_j^{tr} = V_n^{(q)}, \tag{3.32}$$

where B is a drag coefficient for martensitic interface motion. From equations (3.29) and (3.32)

$$\mathscr{D}_j^q = \int_{S_j} \frac{1}{B} {V_n^{(q)}}^2 ds = \int_{S_j} \frac{1}{B} {w^{(q)}}^2 {v_{tip}^{(q)}}^2 ds. \tag{3.33}$$

By defining $\alpha = \int_{S_j} \frac{1}{B} {w^{(q)}}^2 ds$, it is summarized

$$\mathscr{D}_j^q = \alpha {v_{tip}^{(q)}}^2. \tag{3.34}$$

An effective driving force at tip (q) is defined such that the dissipation

of martensitic transformation is the same as the dissipation of martensitic transformation when tip (q) is moved and the opposite tip is fixed. By substituting the change rate of martensitic area with $\frac{d\Omega^{(q)}}{dt} = \pi e c v_{tip}^{(q)}$, we obtain

$$\mathscr{D}_j^q = \bar{f}^{(q)} v_{tip}^{(q)} (\pi e c) \,. \tag{3.35}$$

By using equations (3.34) and (3.35) it gives $\bar{f}^{(q)} v_{tip}^{(q)} (\pi e c) = \alpha {v_{tip}^{(q)}}^2$ and

$$\bar{f}^{(q)} = \int_{S_j} f_j^{tr} w^{(q)}(x) ds. \tag{3.36}$$

Therefore, the following effective kinetic relation is proposed for the two way martensitic phase transformation

$$\begin{cases} v_{tip}^{(q)} = \frac{\bar{f}^{(q)}}{B} & \text{if} \quad 0 \leq |v_{tip}^{(q)}| < v_{max}, \\ v_{tip}^{(q)} = v_{max} sign(\bar{f}^{(q)}) & \text{if} \quad v_{max} \leq |v_{tip}^{(q)}|. \end{cases} \tag{3.37}$$

3.3.3 Elimination of martensitic regions

During the reverse phase transformation (martensitic to austenitic phase), the jth elliptical martensitic region is reduced in size based on kinetic relation of tips as discussed in the previous part. The shrinking is continued until the size of the jth region be equal or less than the embryo dimensions (d_0 and c_0). Then, this martensitic region will be eliminated from the structure completely.

3.4 Conclusions

During the kinetically interaction between dislocations and transformations, the following assumptions were considered: (i) the dislocations that are nucleated and have moved in the asutenitic region would be fixed if they reach a martensite region, (ii) dislocation sources inside martensitic regions are deactivated and no new dipoles are nucleated in the martensitic phase, and (iii) the solution process is an explicit procedure and it means that by using the states and fields of system at time t the structure of sample will be updated for time $t + \Delta t$.

The method described in this section is used to model the interaction between plasticity and martensitic phase transformation in SMAs. Typical length scale for this method is much smaller than continuum mechanics and much larger than three-dimensional atomistic simulation. Hence, both plastic and phase transformation mechanisms are modeled by suggested constitutive rules for nucleation, motion and annihilation of dislocations and transformations in micro-structure.

Chapter 4

Simulation of Single crystal NiTi

The two dimensional discrete-dislocation-transformation framework that is developed in chapter 3 is applied to model the mechanical behavior of single crystal NiTi shape memory alloy. This particular shape memory alloy is selected as a material sample because it is the commonly used SMA in applications [148]. This chapter presents the results for isothermal mechanical loading in section 4.1 and thermo-mechanical loading in section 4.2. The behavior of material is also investigated under multiple mechanical and thermal cyclic loadings

4.1 Isothermal mechanical loading of single crystal NiTi

In the following simulations, temperature is kept constant and behavior of the specimen is investigated under mechanical loading. To find the different parameters which affect the thermo-mechanical behavior of material, the problem is solved under three different assumptions: (i) fully austenitic plastic loading, (ii) stress-induced martensitic transformation with the plastic deformation neglected, and (iii) martensitic transformation interacting with dislocation plasticity. The assumption for each loading case is discussed in the related section.

4.1.1 Problem assumptions and material parameters

For all of the simulations in this section, it is assumed that the material is loaded in two-dimensional plane strain condition in $(\bar{1}\quad 0\quad 1)$ plane. This plane is perpendicular to three slip planes which are considered according to [149] for BCC structures. $(1\quad 2\quad 1)[1\quad \bar{1}\quad 1]$, $(\bar{1}\quad 2\quad \bar{1})[\bar{1}\quad \bar{1}\quad \bar{1}]$ and $(1\quad 0\quad 1)[0\quad 1\quad 0]$ are the slip systems which represent the movement of edge dislocations. The loading plane and slip systems are illustrated in Figure 4.1.

The martensitic transformation in NiTi is from BCC austenitic structure to monoclinic crystal. As discussed in Chapter 3, among all possible

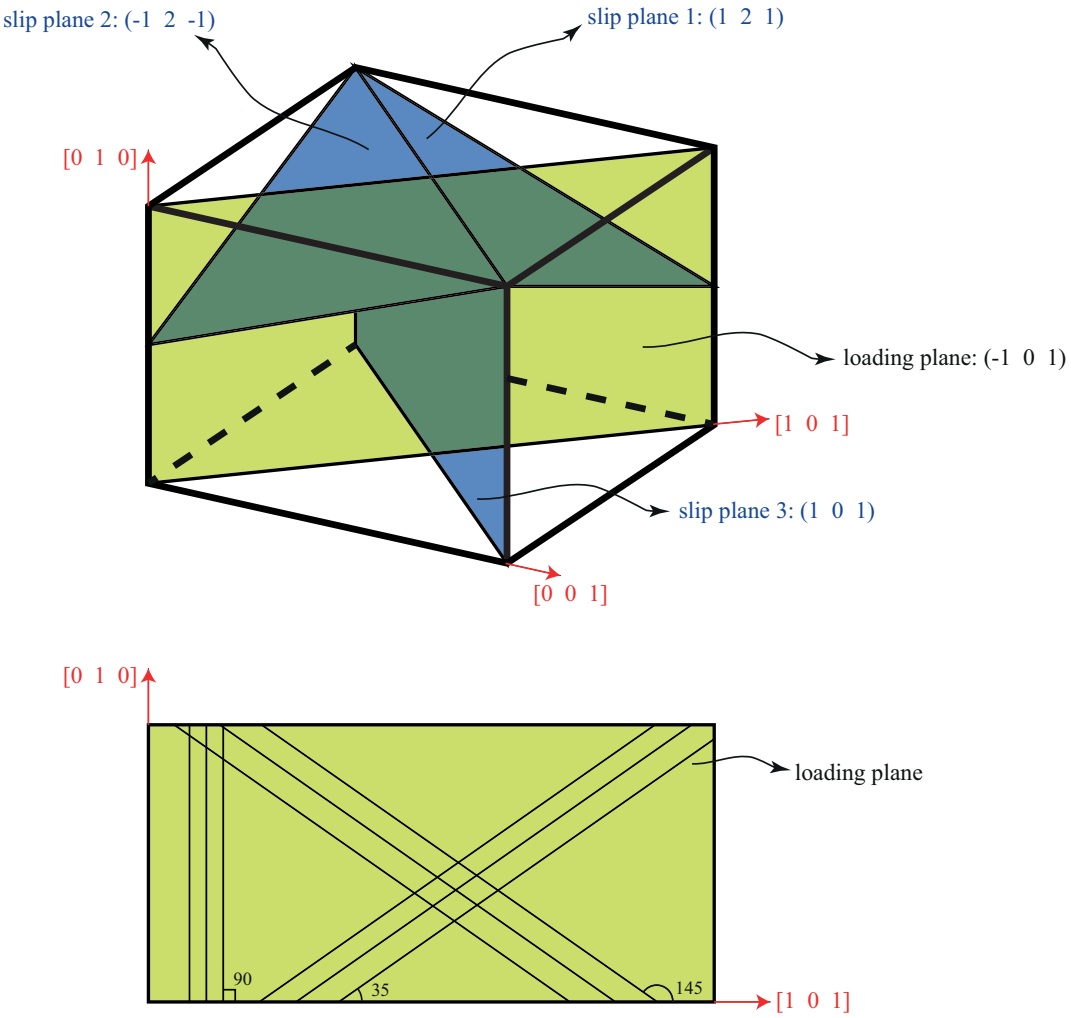

Figure 4.1: Schematic of slip planes and plane-strain loading plane for BCC crystal [149].

transformation systems in three-dimensional space, two systems are considered such that the habit plane normal **m** and strain vector **a** are perpendicular to loading plane normal $(\bar{1} \quad 0 \quad 1)$. The single crystal domain including slip planes and transformation regions are presented schematically in Figure 4.2.

The initial phase of the specimens is fully austenite in stress-free and dislocation-free configuration. Furthermore, dislocation sources are ran-

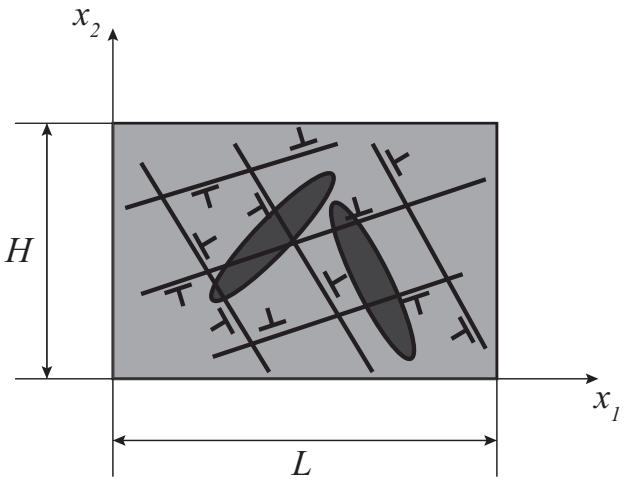

Figure 4.2: Schematic of single crystal problem including slip and transformation systems.

domly distributed on slip planes that are spaced 100×b apart, where b is the magnitude of Burgurs vector. The strength of each dislocation source is also assigned randomly with the Gaussian distribution scheme. The location and strength of transformation sources are defined in the similar way, with consideration of habit planes instead of slip planes. Furthermore, the minimum possible distance between two martensitic sources is also defined as $2 \times d_0$ where d_0 is the semi-major axis of the martensitic embryo. The critical value for nucleation f_j^{cr} of jth transformation source, is specified by considering the fact that the transformation nucleation has taken place in time t if the new martensitic embryo can grow in the next time step. Therefore, the critical nucleation driving force is the one which results the above mechanism. Furthermore, the parameters of transformation strain (δ, γ) are assumed to be scaled by a factor of 0.1 of the actual crystallogra-

phy values. The purpose is to keep the total deformation and numbers of dislocations that are nucleated during the process within computationally tractable range. This assumption limited the maximum recoverable inelastic strain that the material can experience. Table 4.1 presents a summary of the material parameters for NiTi SMA which are used in the simulations.

Table 4.1: Material Parameters of NiTi.

Elastic Constants	[150]
$E_M \approx E_A = 62 \times 10^9$ Pa	
$\nu_M \approx \nu_A = 0.33$	
Density: $\rho = 6500$ Kg/m^3	
Discrete Dislocation Properties	[34, 151]
Burgers vector: $b = 0.25$ nm	
nucleation time: $t_{nuc} = 10$ ns	
Drag coefficient: $B_d = 10^{-4}$ Pa.s	
Cut off value for velocity: $v^d_{max} = 20$ m/s	
Source Strength: τ^{cr} (Gaussian) mean= 195 MPa , std.dev= 40 MPa	
Discrete Transformation Properties	[150, 151]
$M_f = 51°$C $M_s = 71°$C $A_s = 92°$C $A_f = 105°$C	
Transformation strain: $\gamma = 0.11$ and $\delta = 3.4 \times 10^{-3}$	
Latent heat: $\lambda = 130$ Mj/m^3	
Cut off of tips velocity: $v^m_{max} = 4800$ m/s	
Drag coefficient of transformation: $B_m = 40$ Pa.s	
Source Strength: f^{cr} (Gaussian) mean= 6 MPa , std.dev= 1.2 MPa	

The dimension of the specimen in this study is $2\mu m \times 2\mu m$, and it is subjected to the plane strain uni-axial loading. The boundary conditions

and loading information are mentioned in equation (4.1).

$$\begin{cases} u_1(x_1 = 0, t) = 0, & t_2(x_1 = 0, t) = 0, \\ u_1(x_1 = L, t) = L\dot{\varepsilon}t, & t_2(x_1 = L, t) = 0, \\ t_1(x_2 = 0, t) = 0, & t_2(x_2 = 0, t) = 0, \\ t_1(x_2 = H, t) = 0, & t_2(x_2 = H, t) = 0, \end{cases} \tag{4.1}$$

where $\dot{\varepsilon}$ is the applied strain rate, H is height, and L is length of the specimen, as it is shown schematically in Figure 4.2.

4.1.2 Plasticity in austenitic phase

The isothermal mechanical loading to observe plastic deformation in the austenitic phases is simulated in this section. The temperature is chosen and kept constant such that the specimen deforms plastically in austenitic phase before occurrence of stress-induced transformation. To satisfy this condition, the temperature of specimen should be higher than the martensitic transformation temperature M_d [152]. $M_d > A_f$ is the temperature at which the energy for stress-induced martensitic transformation is equal to the energy for austenitic plastic deformation. $M_d = 120°C$ for NiTi [11]; therefore, the temperature in these simulations is selected to be higher than $120°C$. The discrete dislocation method is used to simulate the plastic deformation of austenitic NiTi with no martensitic transformation.

The displacement-control loading is characterized by strain rate along the loading process. Due to the computation time limitation, the strain rate in discrete dislocation problems is much higher than the real experimental values. Therefore, it is important to select a strain rate for loading that provides reasonable results with acceptable computation costs. Thus, to explore the effect of displacement loading rate on the results, a number of parametric analysis were performed in different strain rates. The results of simulations with strain rates $10^5 s^{-1}$, $10^4 s^{-1}$, $5 \times 10^3 s^{-1}$, $2.5 \times 10^3 s^{-1}$, and $10^3 s^{-1}$ are presented in Figure 4.3. As can be seen in this figure, the strain rate of $10^5 s^{-1}$ is too high to predict the plastic deformation. However, the mechanical behavior of the specimens shows less dependency on strain rates when the loading rate is reduced to lower strain rates such as $5 \times 10^3 s^{-1}$, $2.5 \times 10^3 s^{-1}$, and $10^3 s^{-1}$. Therefore, to have a model of plasticity at acceptable computational cost, the strain rate of $5 \times 10^3 s^{-1}$ is applied for the subsequent problems.

Although the dislocation source density is one of the material parameters, a number of parametric analysis were conducted to investigate the effect of this parameter on the results. Different simulations, considering the dislocation source densities as $10\mu m^{-2}$, $20\mu m^{-2}$, $30\mu m^{-2}$, and $40\mu m^{-2}$, are implemented and Figure 4.4 shows the comparison between the results. As illustrated in this figure, except $\rho^d_{source} = 10\mu m^{-2}$, the other dislocation source densities such as $20\mu m^{-2}$, $30\mu m^{-2}$, and $40\mu m^{-2}$ resulted in the re-

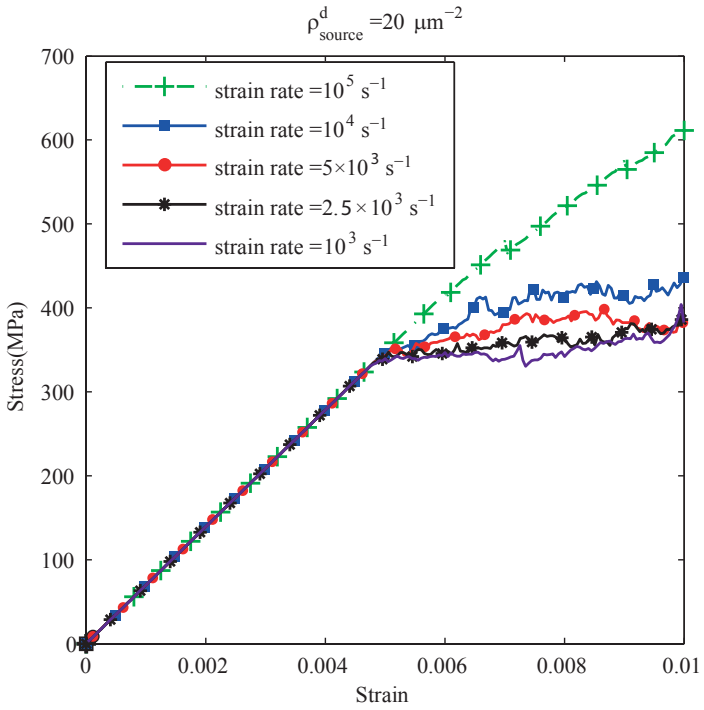

Figure 4.3: Effect of strain rate on stress-strain response in $\rho^d_{source} = 20\mu\text{m}^{-2}$.

sponses falling within a close range. Therefore, $\rho^d_{source} = 30\mu\text{m}^{-2}$ in the simulations is sufficient to provide a good prediction of results in addition to acceptable computational time.

Finally in this section, the specimen is loaded to 0.01 strain, followed by an unloading process. Figures 4.5a and 4.5b show the stress-strain response of austenitic plastic deformation and the variation of dislocation density during the loading/unloading processes, respectively. The predicted mechanical response illustrates the dislocation slip plasticity followed by elastic loading similar to plasticity mechanism of the other crystalline metals. It is worth mentioning that, this simulation is an observation of dislocation slip mechanism in NiTi when the martensitic transformation has not

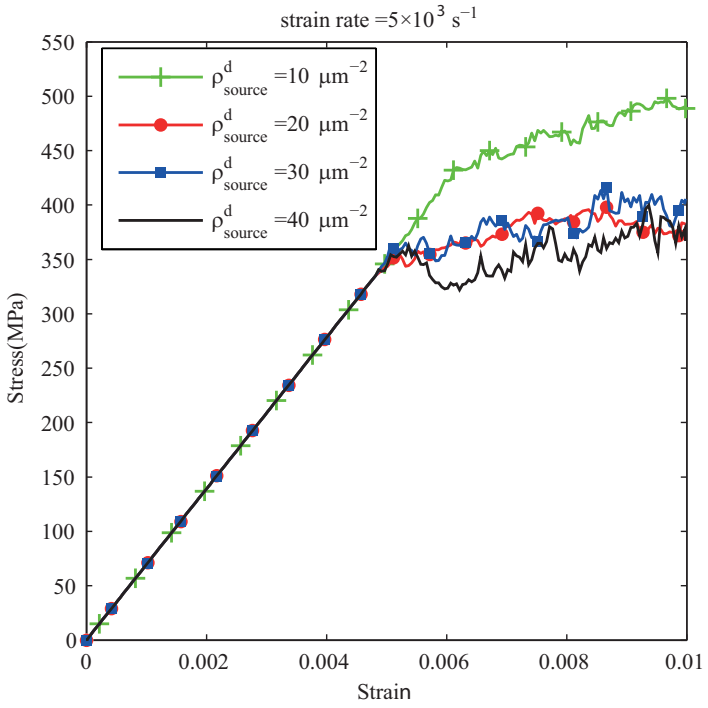

Figure 4.4: Effect of dislocation source density on the stress-strain response in $\dot{\varepsilon} = 5 \times 10^3 \mathrm{s}^{-1}$.

taken place in the micro-structure. Therefore the results presented in Figure 4.5 will be discussed more comprehensively in the next section where it will be compared with situations including the martensitic transformation mechanism.

4.1.3 Stress-induced martensitic transformation in absence of plastic deformations

The next group of isothermal simulations are designed at a temperature that the stress-induced martensitic transformation occurs and the pseudo-elastic response is investigated by mechanical loading and unloading path. Therefore, the temperature is kept constant above A_f but less than M_d:

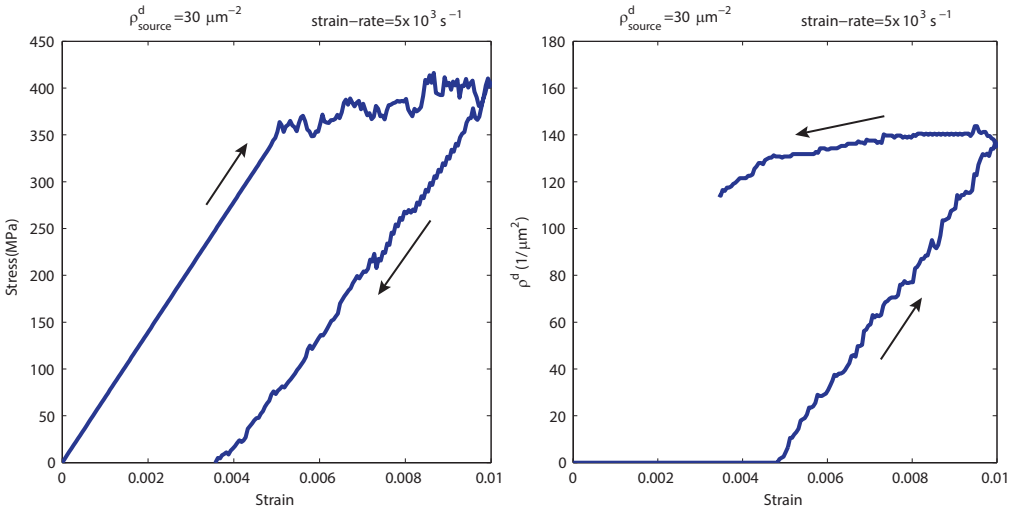

Figure 4.5: The elastic plastic response of austenitic NiTi.

$A_f < \theta < M_d$. It means that the material is initially in austenitic phase with stable cubic B2 structure. To have a better observation of the interaction between dislocations and martensitic interface, in this section the simulation is implemented without considering the dislocation plasticity. In the next section, the same problem with the effect of dislocation slip is solved. Therefore, the dislocation source density is kept at zero here and no dislocation nucleation and gliding are observed.

Similar to the parametric study of dislocation source densities in the previous section, the effects of applied strain rate and transformation source densities on martensitic transformation mechanism are revealed in Figures 4.6 and 4.7, respectively. The results presented in Figures 4.6a and 4.6b indicate that the loading rate does not influence the stress and martensitic volume fraction values. Therefore, the choice of $\dot{\varepsilon} = 5 \times 10^3 \mathrm{s}^{-1}$ gives

reasonable results as well as an acceptable computational time.

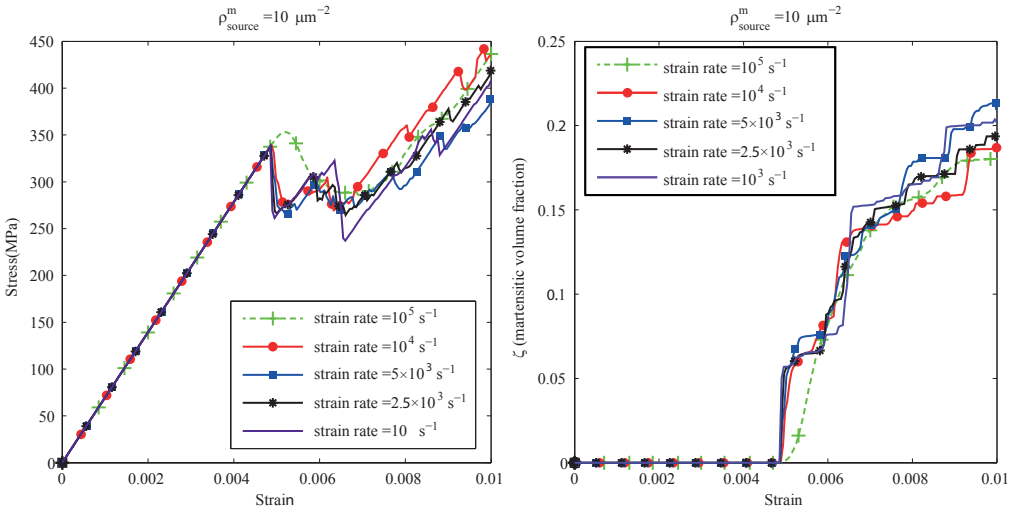

Figure 4.6: Effect of applied strain rate on discrete transformation model during the pseudoelasticity mechanism.

As defined in chapter 3, the martensitic transformation is generated from initial random transformation sources. The transformation source density is a user defined parameter that influences the computation time. However, results in Figure 4.7a and 4.7b demonstrate that the value of martensitic volume fraction and stress are fairly independent of transformation source density. Furthermore, the comparison of martensitic volume fraction in Figure 4.7b shows an interesting result that the transformation source density does not alter the maximum accessible volume of martensitic area in the simulation. Therefore the choice of $\rho^m_{source} = 8\mu\text{m}^{-2}$ maintains both reasonable results and acceptable computation costs in the discrete transformation problems.

The pseudo-elastic behavior of NiTi in the absence of dislocations is

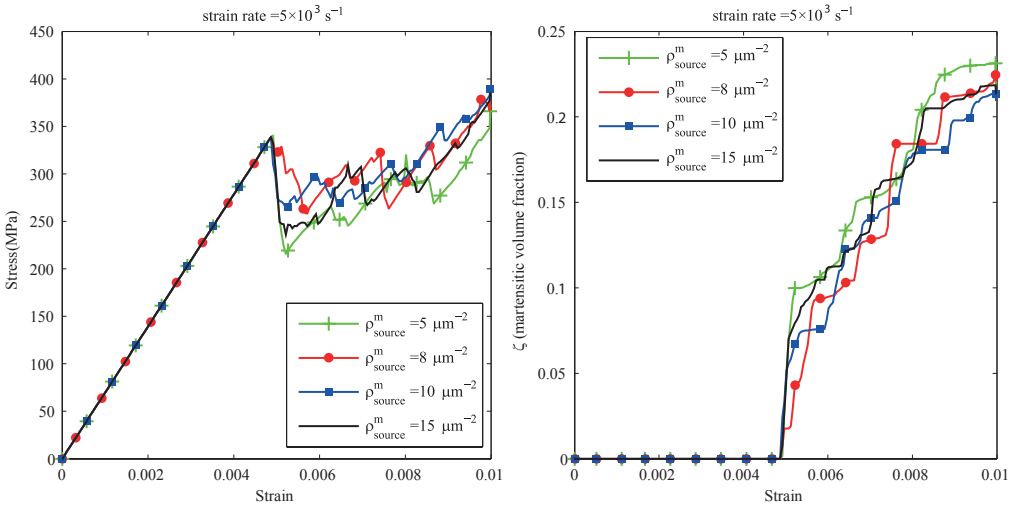

Figure 4.7: Effect of transformation sources on discrete transformation problem.

illustrated in Figure 4.8. It is shown that the loading and unloading processes are completely reversible and there is no residual strain at the end of one cycle loading. It is also indicated in Figure 4.8b that the material transformed to martensite during loading and transformed back to austenite completely after unloading to the original state. There are no remaining martensitic regions in the system after backward transformation.

The results presented in Figure 4.8 will be used in the next section where the dislocation plasticity is taken into account during the pseudo-elasticity mechanism. The comparison of material behavior with and without dislocations will be presented in that section.

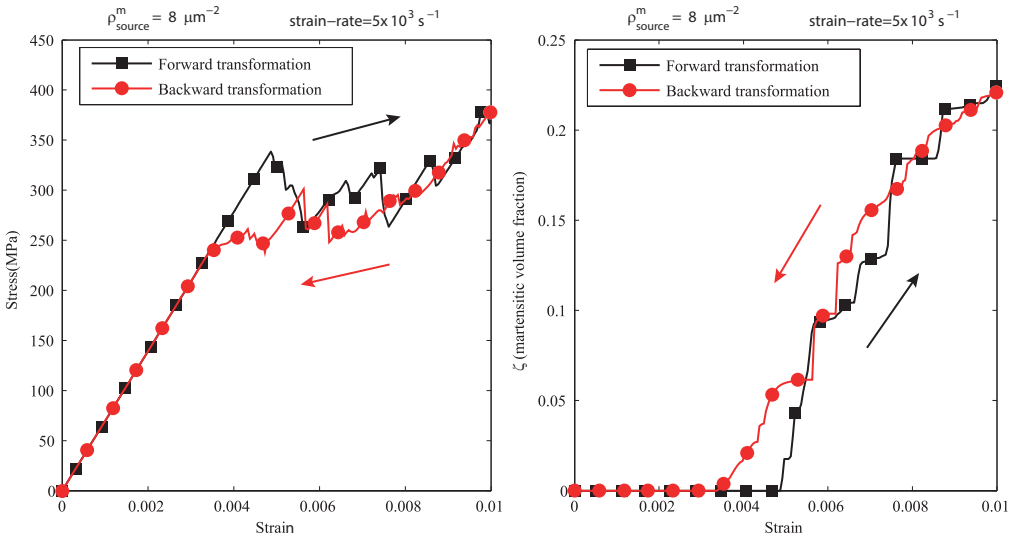

Figure 4.8: Two way shape memory effect with out considering dislocation slip.

4.1.4 Interaction between martensitic transformation and dislocation plasticity

After illustrating the stress-induced martensitic transformation in absence of dislocation plasticity in the previous section, the effect of dislocation slip is considered along with the pseudo-elastic behavior of the single crystal NiTi. The material is considered initially in austenitic phase, and it contains random dislocation and transformation sources. Therefore, dipoles and martensitic regions can be generated during isothermal loading; $A_f < \theta < M_d$. The mechanical responses of single crystal NiTi under isothermal mechanical loading is presented in Figures 4.9a – 4.9c.

The stress-strain response in Figure 4.9a shows that the loading/unloading cycle is not fully reversible in this case, and there are some residual strain

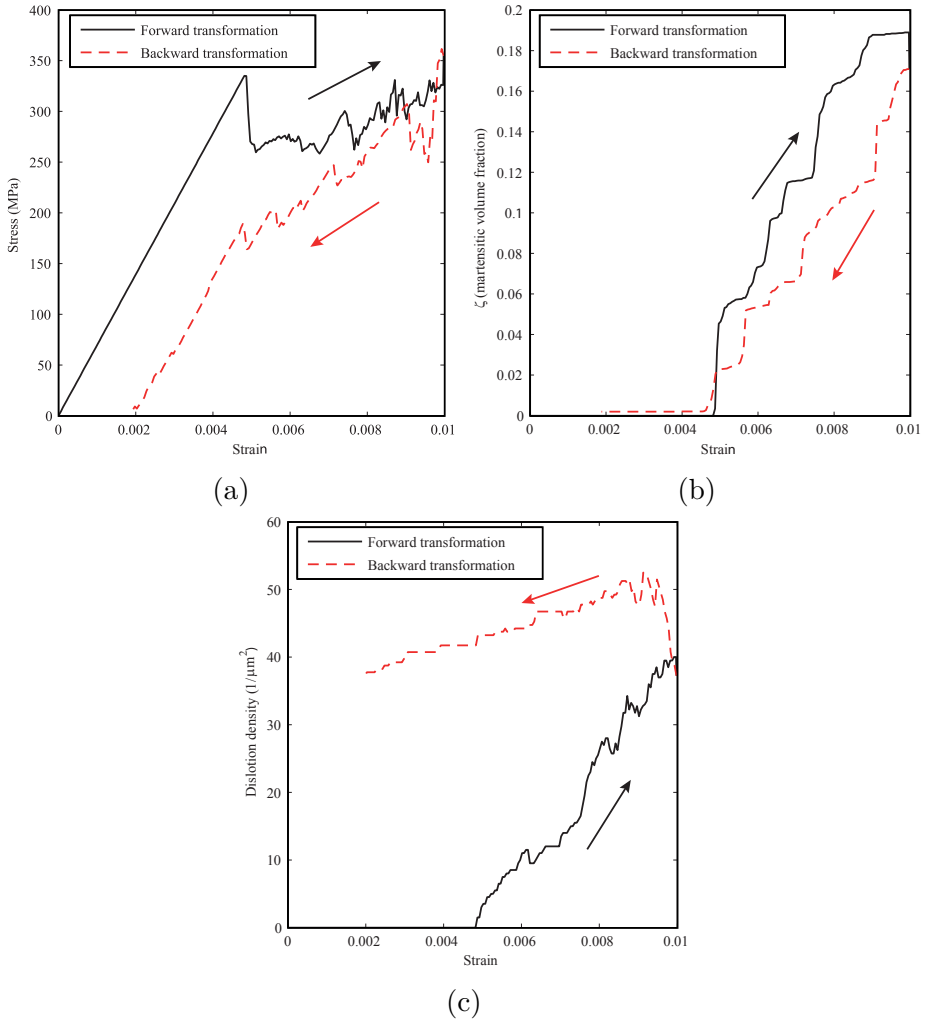

Figure 4.9: The pseudoelasticity behavior of NiTi affecting by dislocation slip mechanism for the case with: $\rho^d_{source} = 30\mu m^{-2}, \rho^m_{source} = 8\mu m^{-2}$, and strain-rate$= 5 \times 10^3 s^{-1}$.

after the unloading process. The residual strain is due to the remaining martensitic phases and dislocation slips. To analyze the reasons of the irreversibility, the change of martensitic volume fraction and dislocation density are given in Figures 4.9b and 4.9c, where the dashed line in all figures represents the backward transformation (unloading). It can be seen that a small fraction of martensitic region remained in the domain after

unloading, as the dashed line did not touch the solid line at strain near 0.002. Furthermore, it is shown in Figure 4.9c that dislocation dipoles are generated and moved in the domain. They cause the generation of plastic strain that remained at the end of the loading-unloading process.

In the following, the particular effect of dislocation plasticity on transformation mechanism and the effect of phase transformation on dislocation slip in SMAs are presented in Figures 4.10, 4.11, and 4.12. In Figure 4.10, only the forward transformation part of pseudo-elastic behavior of NiTi, with and without dislocation slip, are compared. It can be seen in Figures 4.10a and 4.10b that, in both simulations, the martensitic transformation begun at the same stress. This implies that the nucleation of marensitic regions is not affected by dislocation dipoles. It is because the threshold stress of dislocation nucleation is higher than the threshold stress for generation of transformation. Hence, when the first martensitic inclusion is nucleated, there is no dipole in the domain. This result also encourages us to continue loading and unloading process for more cycles. Then, it is possible to investigate the effects of remaining dislocations from the earlier cycles on the behavior of material in the later cycles. The results of this model are presented in section 4.1.5.

It also can be seen in Figure 4.10b that the material has transformed more in absence of dislocation plasticity after 0.01 strain loading, implying that the existence of dislocations in the system resisted the martensitic

growth. Finally, Figures 4.10a and 4.10b show that, although the transformation is less in the presence of dislocations, the stress-strain curve lies under the one for transformation-only case. This is because some energy is dissipated due to the dislocation plasticity, when the effect of dislocation slip is taken into account.

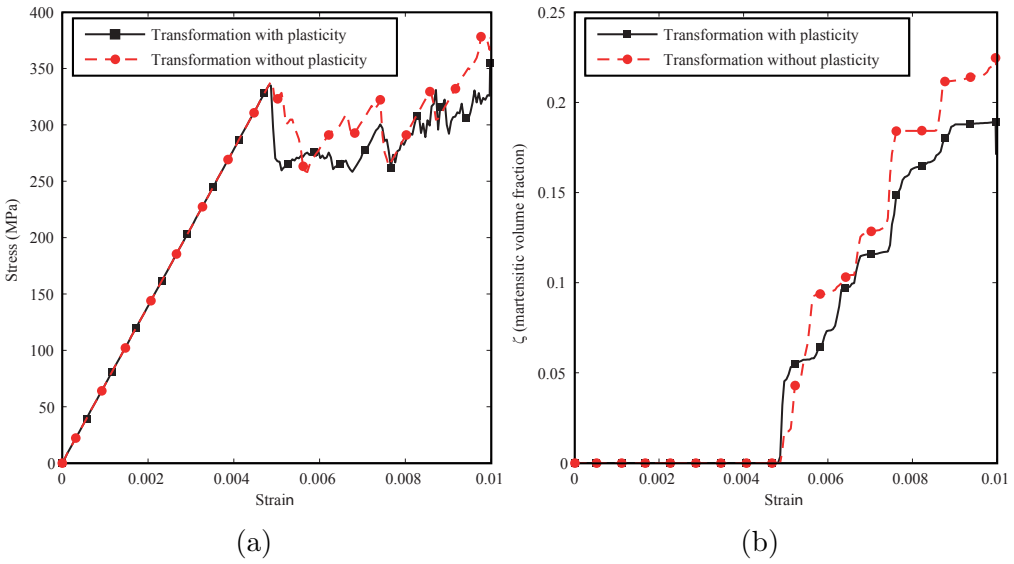

(a) (b)

Figure 4.10: The effect of dislocation plasticity on the forward transformation (loading).

The comparison of pseudo-elasticity behavior of the specimen with and without dislocation slip mechanism is presented in Figure 4.11. As can be seen in Figures 4.11a and 4.11b, the dislocation plasticity causes some irreversible strain in the loading-unloading problem, while it is completely reversible without dislocation effects. This is in addition to the interacting effect that dislocations have on the growth of martensitic interface discussed previously. Furthermore, Figures 4.11c and 4.11d demonstrate that, although the reverse transformation began at a lower value in pres-

ence of dislocations, it could not transform completely back to austenite at the end of unloading and some small values of martensitic area remained in the domain.

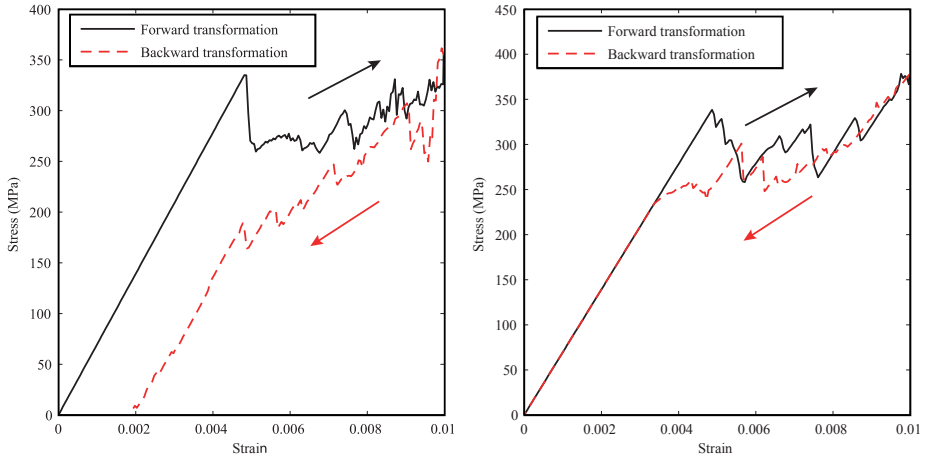

(a) with dislocation slip

(b) without dislocation slip

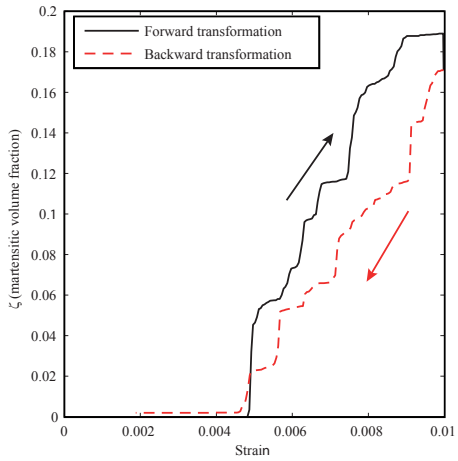

(c) with dislocation slip

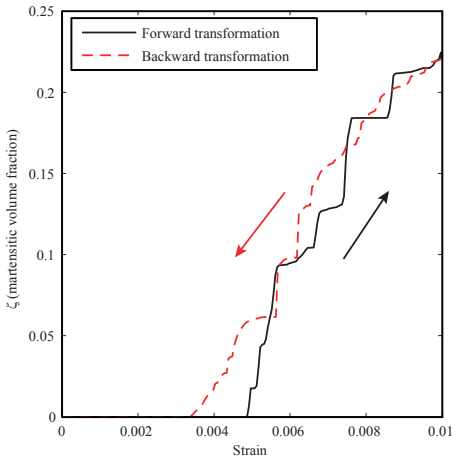

(d) without dislocation slip

Figure 4.11: Comparison of pseudoelasticity behavior for models with and without considering dislocation slip. In plot (b) and (d), there is no dislocation slip while in (a) and (c) both transformation and plasticity occur.

To discuss the particular effect of phase transformation on the dislocation slip mechanism, the results of austenitic plasticity problem that was presented in section 4.1.2 is compared with results of transformation with

plasticity. This comparison is illustrated in Figure 4.12.

As it is shown in Figure 4.12a, the average stress response of the plasticity model lies higher than that with both transformation and plasticity. This provides clear evidence that the combination of transformation and dislocation slip causes more relaxation than plasticity mechanism only. Furthermore, Figure 4.12b demonstrates that, the dislocation density is much higher when there is no transformation in the system. This behavior is due to the assumption that there is no dislocation nucleation and dislocation motion in the martensitic area. Therefore, the dislocation sources that are in martensitic regions at time t is turned inactive.

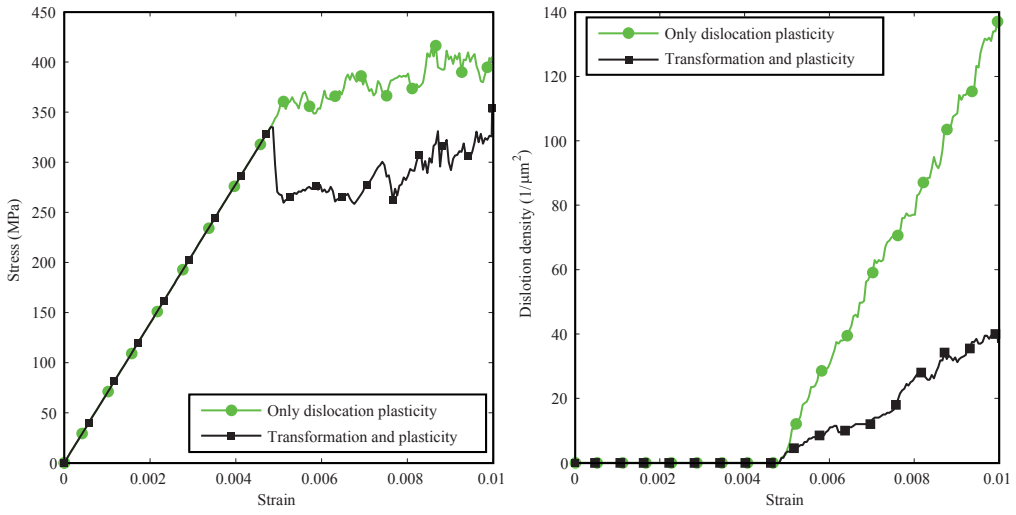

Figure 4.12: The effect of martensitic transformation on dislocation slip plasticity.

Furthermore, to have a better understanding about the interaction between plasticity and martensitic transformation, a comparison of microstructure for these three cases (no plasticity, no transformation, and

plasticity and transformation together) is illustrated in Figure 4.13. The dislocation and martensitic distributions are plotted in Figures 4.13a, 4.13b, and 4.13c as well as average stress contour at the end of loading step. It can be seen in this figure that the dislocations and martensitic regions affect the homogeneity of stress in the domain.

4.1.5 Mechanical cyclic loading

As discussed in the previous section, the local stresses of dislocations affect the nucleation of martensitic transformation in the domain. It was not possible to study this effect with only one cycle of loading. Therefore, the loading-unloading process is repeated for six cycles here. It is worth mentioning that all the dislocations that remained at the end of one cycle, are transfered to the next cyclic loading.

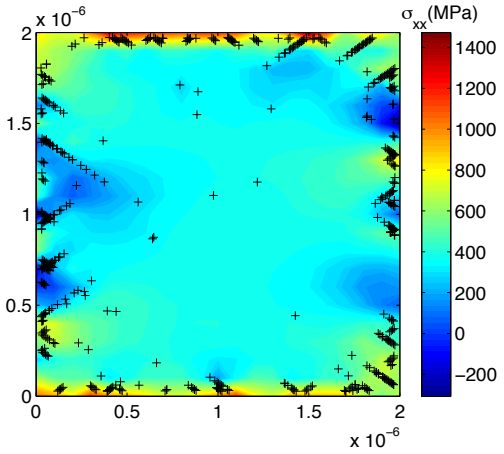

(a)

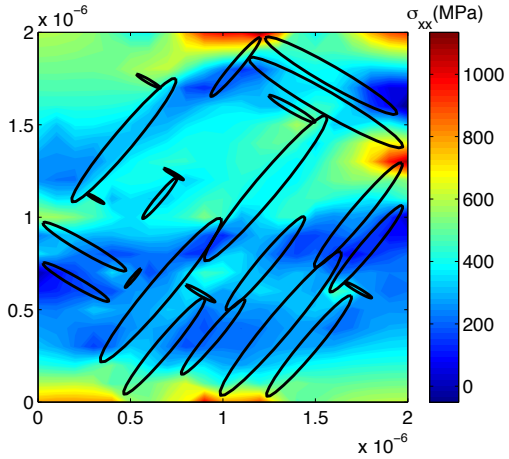

(b)

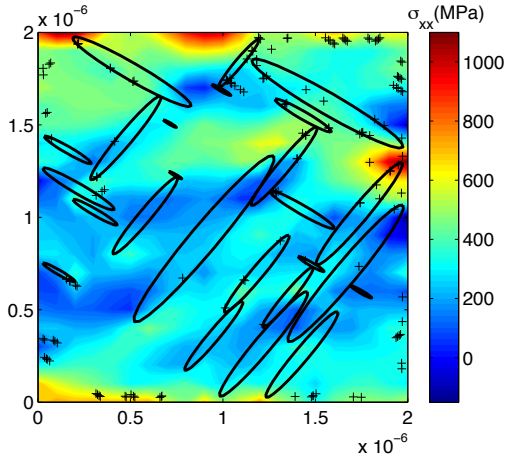

(c)

Figure 4.13: The distribution of average stress, dislocations, and martensitic regions at the end of loading path for : (a) only plasticity, (b) only transformation, and (c) plasticity and transformation together cases.

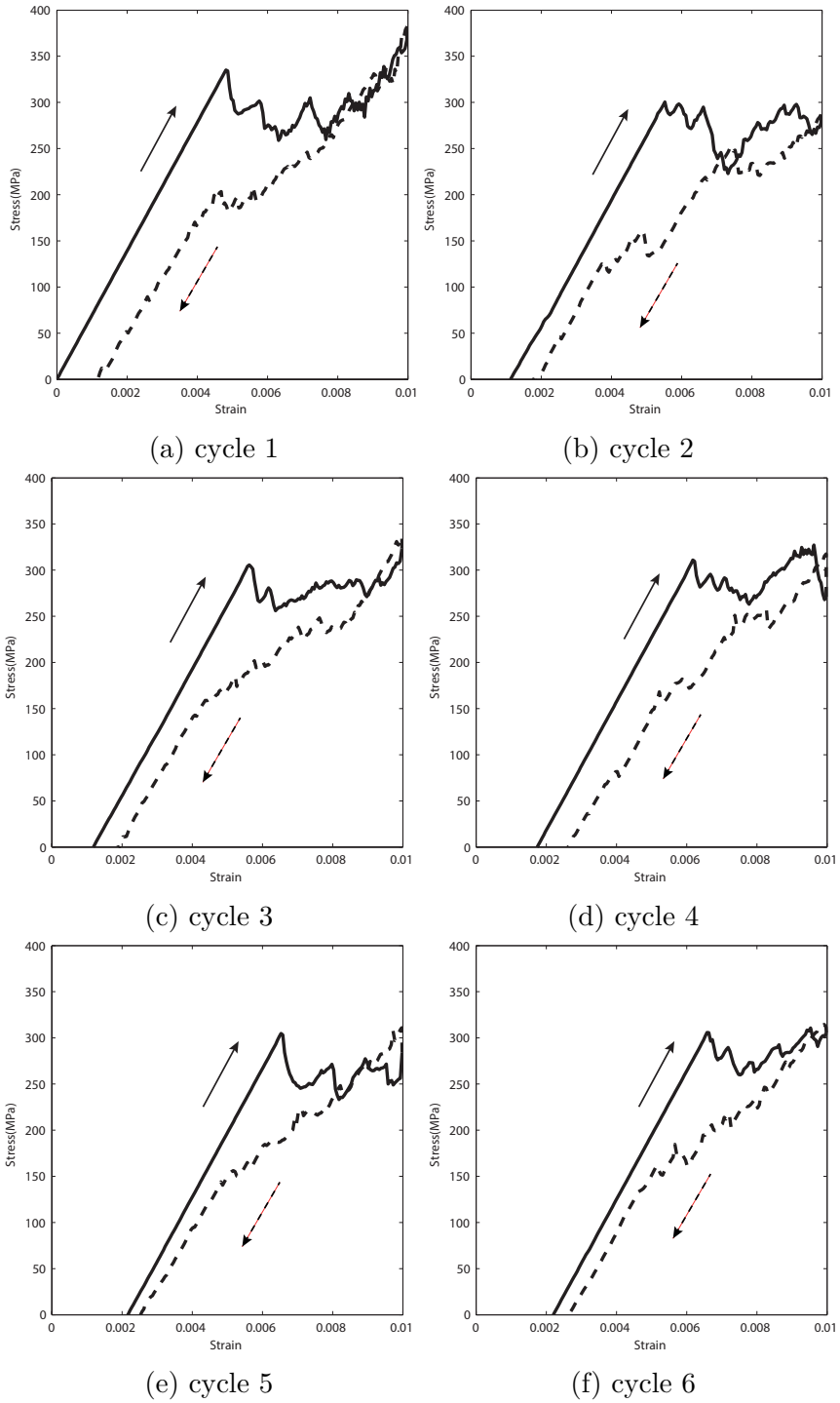

(a) cycle 1 (b) cycle 2

(c) cycle 3 (d) cycle 4

(e) cycle 5 (f) cycle 6

Figure 4.14: Isothermal mechanical loading of single crystal NiTi during 6 cycles.

Figure 4.14 shows the stress-strain behavior of the single crystal NiTi

during six isothermal mechanical cycles. The results suggested that the average stress in which the martensitic transformation begins, is decreased when the material experienced more loading cycles. This implies the effect of local stress of dislocations on the nucleation of transformation areas.

The changes of the critical transformation stress and residual strain during the six loading cycles are presented in Figures 4.15a and 4.15b. Figure 4.15a indicates that the martensitic phase is nucleated at a lower stress level when the number of cycles increases. This behavior is due to the effect of dislocations, which are generated in previous cycles, on the local stress around transformation sources. Furthermore, as can be seen in Figure 4.15b, the amount of residual strain during first cycle is higher than that in the next cycles, and it suggests that multiple cycling can be as a process to make SMAs more stable under thermo-mechanical loading. This behavior is explained by effect of dislocation accumulation in the system which causes hardening in the material.

4.2 Thermo-mechanical loading of single crystal NiTi

Two-way shape memory effect is another behavior that causes SMAs as applicable materials for actuation responses. In this section the behavior of single crystal NiTi is investigated under thermal cyclic loading and constant

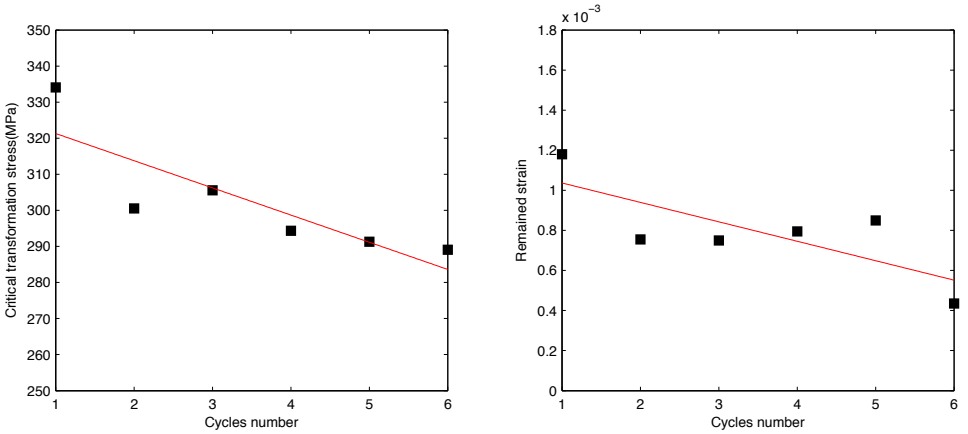

(a) (b)

Figure 4.15: Comparison of (a) critical transformation stress and (b) remain strain in different mechanical cycles.

external stress. To model this behavior, the temperature of material is switched between initial temperature ($T_1 > A_f$) and the low temperature ($T_2 < M_f$) when the domain is under constant stress (50 MPa, 150 MPa, 300 MPa). To study the interaction between plasticity and martensitic phase transformation on two-way shape memory effect, results in 4.2.1 are presented without the effect of dislocation slip while results in section 4.2.2 included dislocation plasticity mechanisms. Finally, in section 4.2.3, the response of material experiencing six cyclic loads is investigated. In all simulations, the thermal expansion strain is subtracted from the results as it has no effect in illustrating two-way shape memory effects.

4.2.1 Two way shape memory effect in the absence of dislocation plasticity

To study the two-way shape memory effect in the absence of dislocation plasticity, the dislocation source points are removed from the specimens. This guarantees that no dislocation is generated in the domain. Then, constant traction of 50 MPa is applied on the specimen and the temperature is reduced from 120°C to 40°C, and then is heated back to 120°C for backward transformation. The results are presented in Figures 4.16 and 4.17.

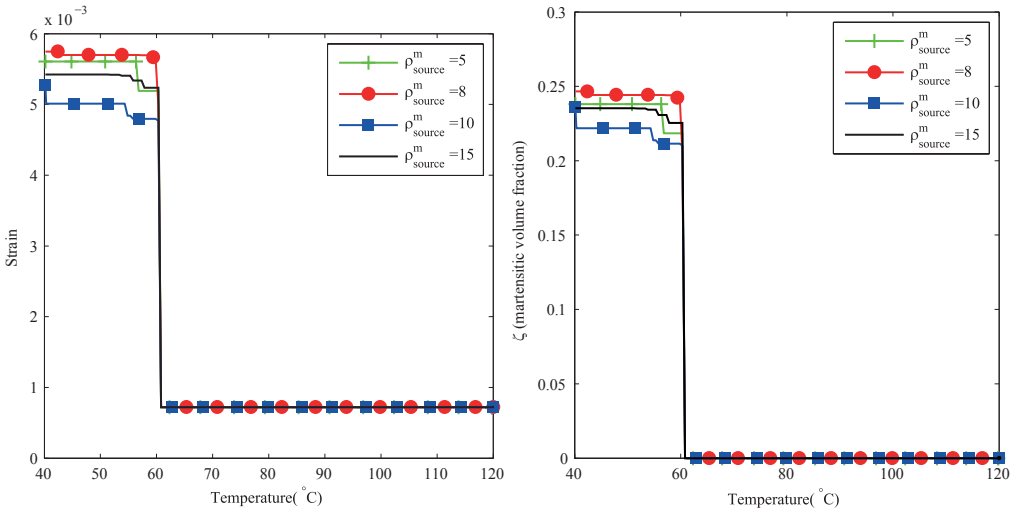

Figure 4.16: Effect of different transformation sources on discrete transformation model during thermal loading.

In Figure 4.16, a parametric study is done to be assured that the transformation source density that was chosen previously ($\rho^m_{source} = 8\mu\text{m}^{-2}$), is a proper choice. The changes of strain and martensitic volume fraction with

respect to temperature for different transformation source densities are illustrated in Figures 4.16a and 4.16b. The comparison from Figure 4.16b provides a clear evidence that changing the transformation source density from 5 to 15 does not affect the maximum marensitic volume fraction that may be generated in the domain. Therefore, $\rho^m_{source} = 8\mu\text{m}^{-2}$ is used in the next simulations to have both reasonable accuracy and acceptable computational time.

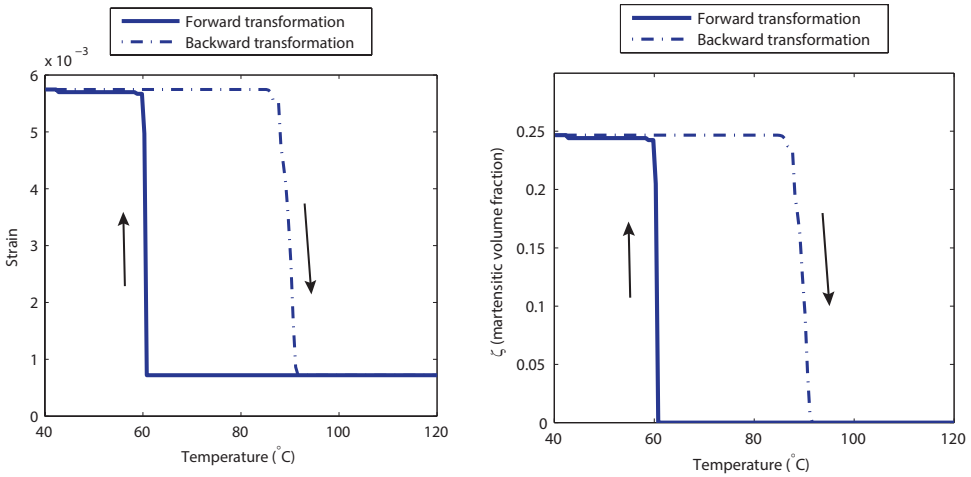

Figure 4.17: Two-way behavior of SMA under thermal loading in absence of dislocation plasticity.

The two-way shape memory effect of NiTi in absence of dislocation slip mechanism is presented in Figures 4.17a and 4.17b. As can be seen in Figure 4.17b, the martensitic volume fraction is increased from zero to 0.25 during cooling process and is declined back to zero after heating the specimen. It shows that the transformation is fully reversible, and no irreversibility is expected to occur in strain-temperature response. Figure

4.17a confirms the expected result and there is no residual strain after one thermal cycle loading. Furthermore, the average stress contour and martensitic distribution at the end of forward transformation is illustrated in Figure 4.18. It can be seen in Figure 4.18 that the stress field is not homogeneous in the domain due to the existence of martensitic regions. The simulations repeated for other applied stresses of 150 MPa and 300 MPa give the similar responses. These results are used in next section where they are compared with results of simulations that are considered with dislocation plasticity.

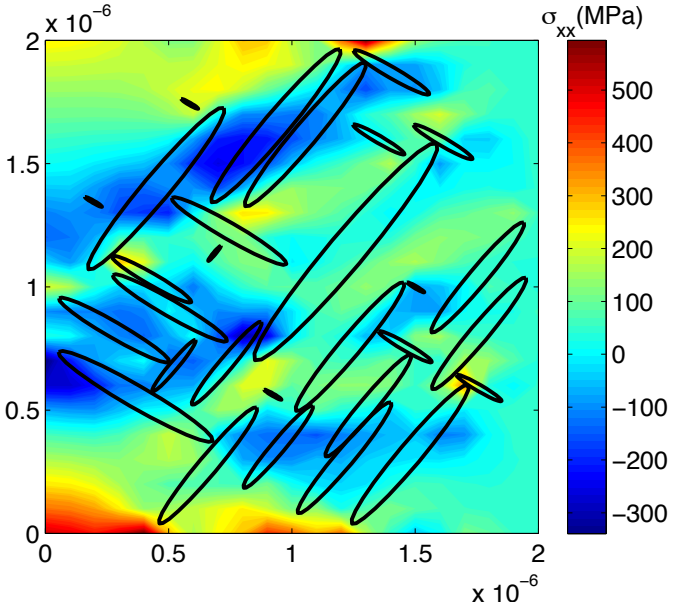

Figure 4.18: The distribution of martensitic regions and average stress at the end of forward transformation for temperature-induced martensitic transformation in absence of dislocation plasticity.

4.2.2 Interaction between thermally activated phase transformation and dislocation plasticity

In this section the two-way shape memory effect behavior of NiTi is investigated when the domain contains random dislocation sources. The discrete-dislocation-transformation framework is used to simulate the response of material to thermal cycle loading. Similar to the previous section, the specimen is cooled from $T1 > A_f$ to $T_2 < M_f$ and is heated back from T_2 to T_1 when it is under constant applied traction. The strain-temperature responses are presented in Figures 4.19a, 4.19b, and 4.19c when the specimens are under 50, 150, and 300 MPa applied traction, respectively. It should be mentioned that all the strain-temperature curves are calibrated to begin from zero strain. This gives a better comparison between responses in different tractions.

It can be seen in Figure 4.19a, that the material is fully reversible under thermal cyclic loading when the applied traction is low. However, when the applied traction on the model is increased to 150 MPa and 300 MPa in Figures 4.19b and 4.19c, there is some residual strain at the end of thermal cyclic loading. These results indicate that although 300 MPa is lower than the dislocation nucleation strength (∼400 MPa), the local stresses are increased in some locations inside the domain due to the nucleation and growth of martensitic regions, lead to dislocation generation. Therefore, the reversibility of actuation behavior is affected by dislocation

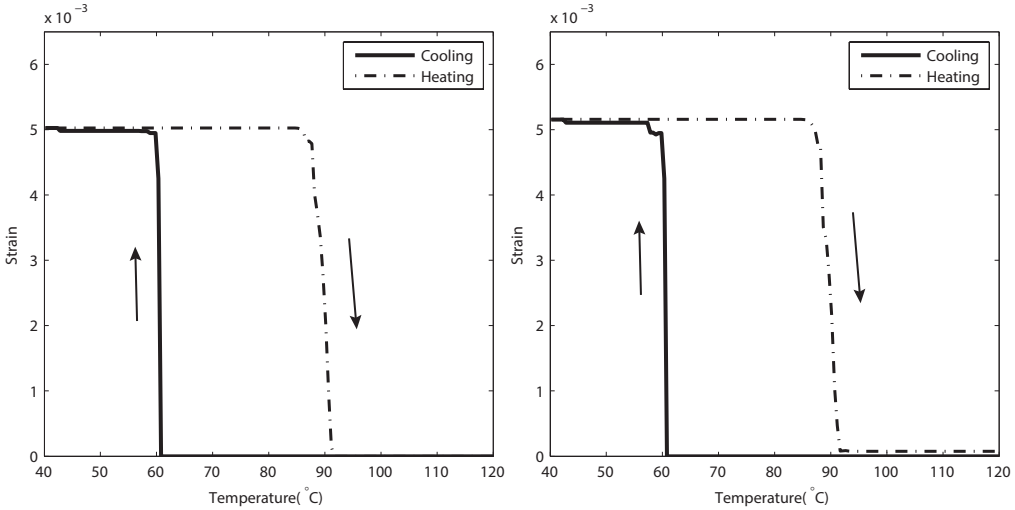

(a) 50 MPa

(b) 150 MPa

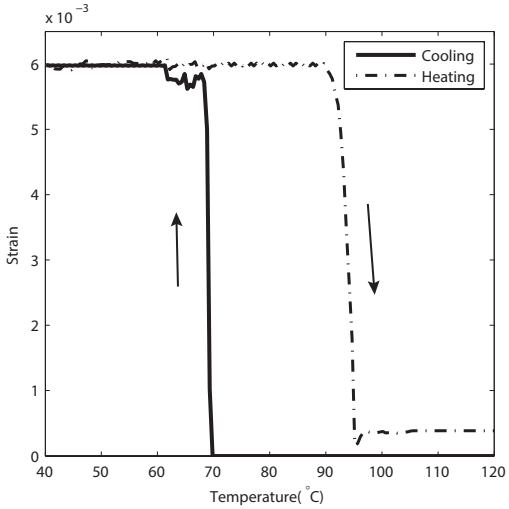

(c) 300 MPa

Figure 4.19: Interaction between martensitic transformation and dislocation plasticity under thermal cyclic loading.

slip at higher applied stresses. This is similar to the experimental results from [105].

The above findings indicate that the martensitic regions activate the nucleation of dipoles and dislocation slip mechanisms which in turn influences the two-way shape memory effect of SMAs. In the next section, the

effect of accumulated dislocations will be studied by simulating the thermal cyclic loading over six cycles.

4.2.3 Thermal cyclic loading

In this part, the same models as section 4.2.2 are loaded for six thermal cycles. The reason to do this is to investigate the behavior of material after accumulation of dislocations. Figure 4.20 presents the strain-temperature response of single crystal NiTi under six thermal cycles loading. It can be seen that the temperature in which the martensitic nucleation occurs is increasing when the number of cycles are increasing. This is due to the local stress of the accumulated dislocations that are generated in the previous cycles. This slight increase in mantensitic start temperature during the first six loading cycles is illustrated more clear in Figure 4.21. It can be explained that the mechanism of transformation nucleation is a thermo-mechanical process; therefore, at higher stress states, the martensitic phase is nucleated in higher temperatures.

In this study due to the computational cost it was not possible to go through large numbers of cycles (e.g. 100 cycles). However, the thermal cycling under external applied stress is a known mechanism of stabilization to reach a fully reversible two-way shape memory effect (2WSME) in shape memory alloys [153, 154].

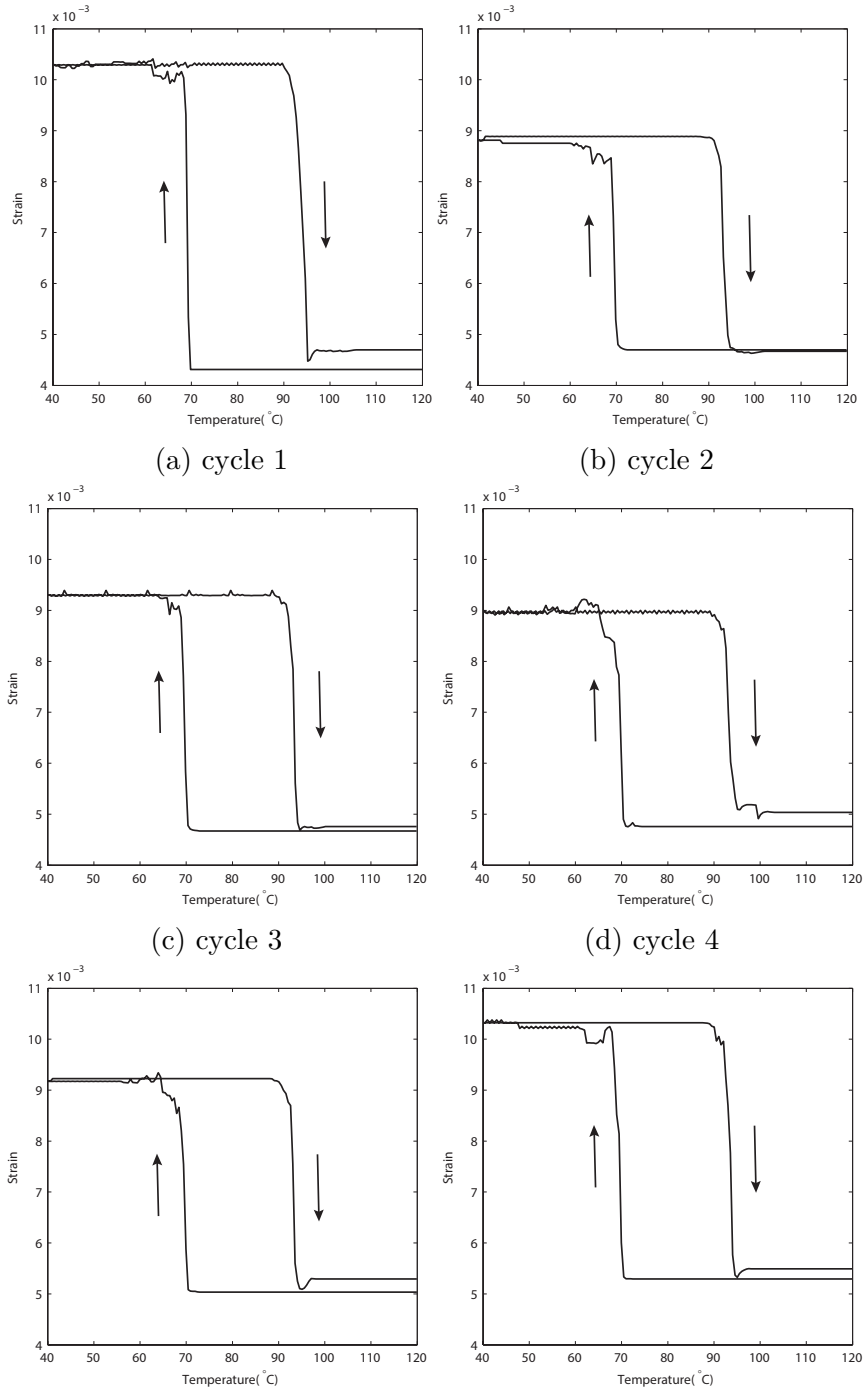

(a) cycle 1 (b) cycle 2

(c) cycle 3 (d) cycle 4

(e) cycle 5 (f) cycle 6

Figure 4.20: Thermo-mechanical loading of single crystal NiTi during 6 thermal cycles when the applied traction is 300 MPa.

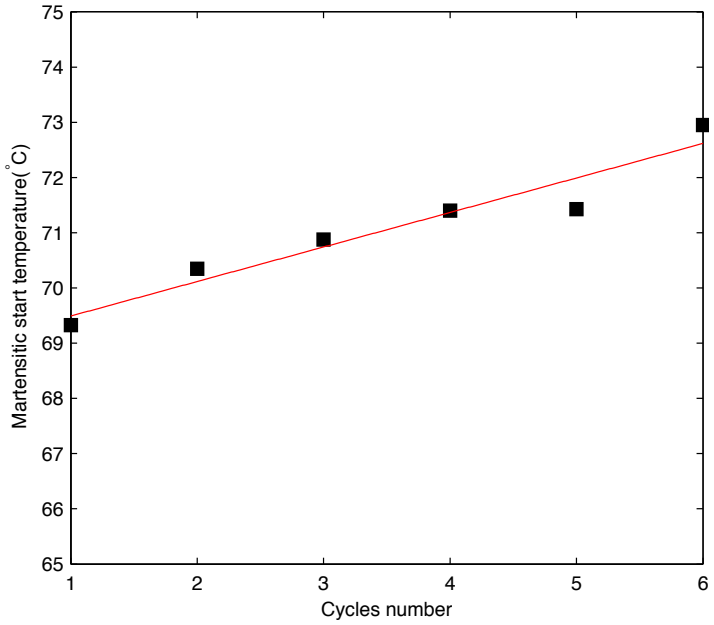

Figure 4.21: Effect of thermal cycling on martensitic start temperature.

4.3 Conclusions

Although the two-dimensional discrete-dislocation-transformation model has some limitations, this model provides useful information about the interaction between plasticity and martensitic phase transformation in shape memory alloys.

The mechanical and thermal cycling of single crystal NiTi show the effects of dislocations on irreversible pseudo-elastic behavior and two-way shape memory effects. Furthermore, the local stress fields of dislocations would lead the nucleation of transformation after repeated cyclic loading.

The martensitic transformation also has opposing effects on dislocation plasticity. On one hand, as shown in the results in Figures 4.17 and 4.19, the local stress fields at the transformed area activates the nucleation and

motion of dislocations when the applied stress is much lower than the dislocation strength. On the other hand, the martensitic-austenitic interface acts as resistance to the movement of dislocations and it reduces the number of nucleated dislocations and their motion, as shown in Figure 4.12.

Chapter 5

Simulation of multi-crystalline NiTi

Polycrystalline metals are materials composed of numerous grains with different sizes and orientations. These grains are connected to each other via grain boundaries across which the orientation of the crystals changes. The material behavior of single and polycrystalline shape memory alloys are different with each other. In single crystals, the behavior is highly dependent on the direction of loading and crystal orientation while the polycrystalline SMA shows less anisotropic behavior. Furthermore, the grain boundaries have a resistance role on the dislocation slip and the growth of transformation regions. A schematic of a polycrystalline structure is illustrated in Figure 5.1.

The material behavior of single-crystal NiTi under thermo-mechanical

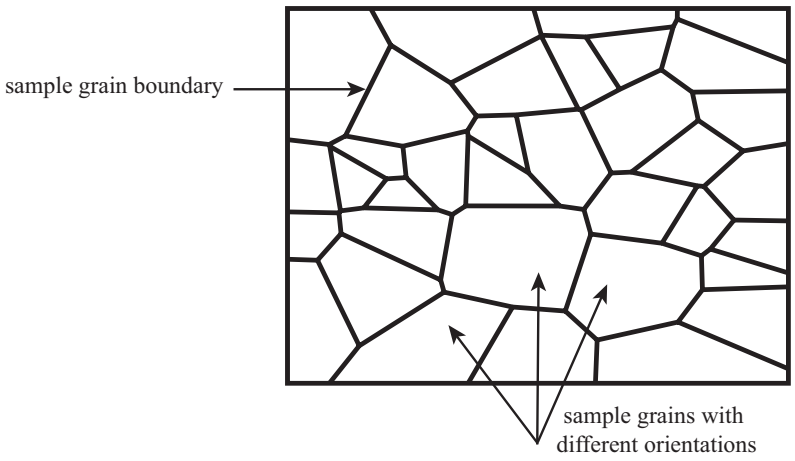

Figure 5.1: The schematic of a polycrystalline structure with grain boundaries.

loading was investigated in chapter 4 using the discrete dislocation-transformation method. However, it is impossible to predict the behavior of metallic devices by modeling the single crystal structure. Therefore, in this chapter the behavior of the untextured multi crystalline NiTi is investigated by discrete dislocation-transformation model under thermo-mechanical loading. An untextured polycrystalline structure consists of randomly oriented grains.

5.1 Discrete dislocation-transformation model for multi-crystal NiTi

The discrete dislocation-transformation method that was presented in Chapter 3, is applied in this section to model the mechanical behavior of multi-crystalline NiTi. The loading conditions and the material constants are the

same as single-crystal model which is described in Chapter 4. However, In the multi-crystalline model, there are numerous grains that are attached together with grain boundaries. Therefore, a new assumption about the grain boundaries is necessary. It is considered that the dislocations and martensitic areas which are nucleated and grown inside a grain cannot pass the grain boundaries. It is an extra limitation to stop the martensitic growth and the dislocations motion. Figure 5.2 shows a schematic of pinning the dislocations and martensitic regions in grain boundaries. Furthermore, in

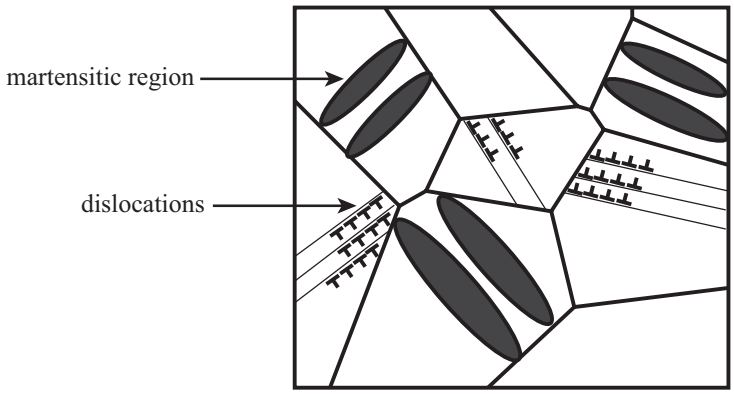

Figure 5.2: Schematic of dislocation and transformation pinning at grain boundaries.

this study, each multi-crystalline structure is considered to be composed of grains of same size and square shape. Then, the orientation of each grain is assigned randomly. This assumption allows us to investigate the effect of crystal orientation and grain boundary density on the mechanical behavior of multi-crystalline NiTi. Moreover, due to the computational limitations, the number of grains are limited to a maximum 16 grains. Therefore, we

called the structures multi-crystalline instead of polycrystalline structure. The schematic of a multi-crystalline specimen including nine grains is illustrated in Figure 5.3.

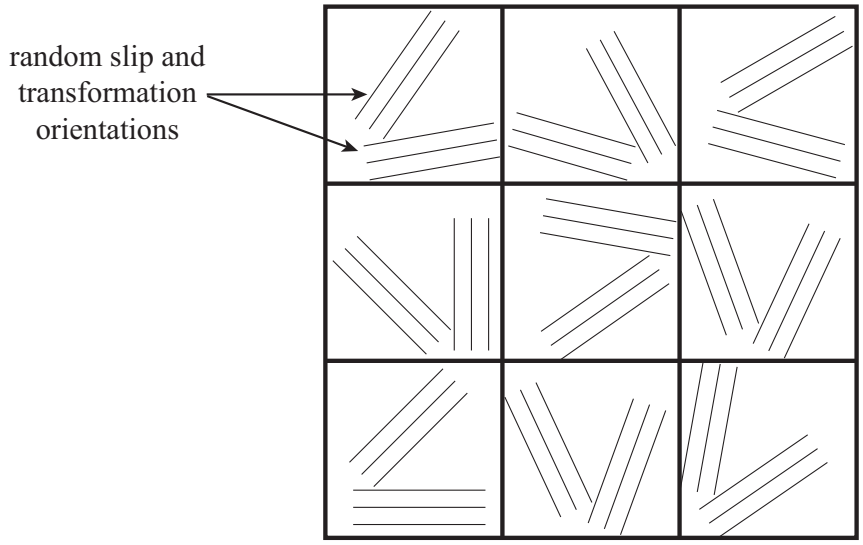

Figure 5.3: Schematic of a specimen with nine randomly oriented and square shape grains.

5.2 Isothermal mechanical loading of multi-crystalline NiTi

The material constants of NiTi in this section are the same as Chapter 4 and the method is the discrete dislocation-transformation framework that is explained in Chapter 3. Although the specimens here are made from multi grains, the boundary conditions are the same as single crystal model. In this section, the multi-crystalline NiTi is loaded mechanically when the temperature is constant. Then the effects of grain size and orientation

on the pseudoelasicity behavior of NiTi are investigated. The results are presented and categorized in the following sections: (i) grain orientation effect and (ii) grain size effect.

5.2.1 Grain orientation effects

As shown in previous chapters, the Peach-Koehler driving force of dislocations and dislocation sources is a function of the angle between loading direction and crystal orientations. Therefore, it is expected that the different grains in multi-crystalline materials experience different dislocation history. In shape memory alloys, the transformation mechanism is also orientation dependent. Therefore, the martensitic nucleation and the growth of transformation interface are affected by the grain orientation. This inhomogeneity of dislocations and martensitic regions cause the inhomogeneity of stress field through the domain.

In this part of the study, the following simulations are designed to check whether the discrete dislocation-transformation model, which is described in Chapters 3 and 4, is able to capture the grain orientation effect in the multi-crystalline SMA. Therefore, it is schematically depicted in Figure 5.4, the mechanical responses of four cases are studied under isothermal mechanical loading. Each case is a combination of two grains: the orientation of the first grain in each case is kept the same while the orientation of the second grain is defined by rotating it with respect to the first by

zero, 15, 30, and 45 degree for cases 1 to 4, respectively, as schematically illustrated in Figure 5.4.

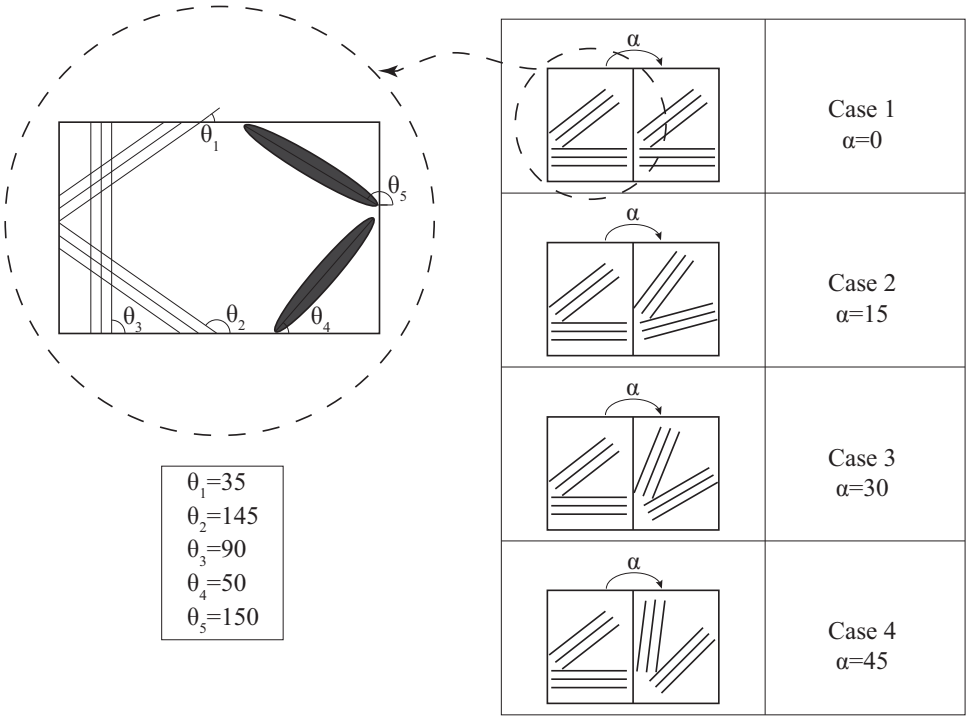

Figure 5.4: Schematic of grain orientation problem.

The comparison of the stress-strain curve of the above four cases under isothermal mechanical loading is compared in Figure 5.5. As expected, Figure 5.5 shows the different mechanical response for the four cases due to the different orientation of grains. However, it is not clear yet that this variation of results is due to the difference of dislocation slip directions or transformation systems or both of them. To find out the answer of this question, the change of dislocation density and martensitic volume fraction during the loading is compared for the above four cases in Figures 5.6 and 5.7, respectively.

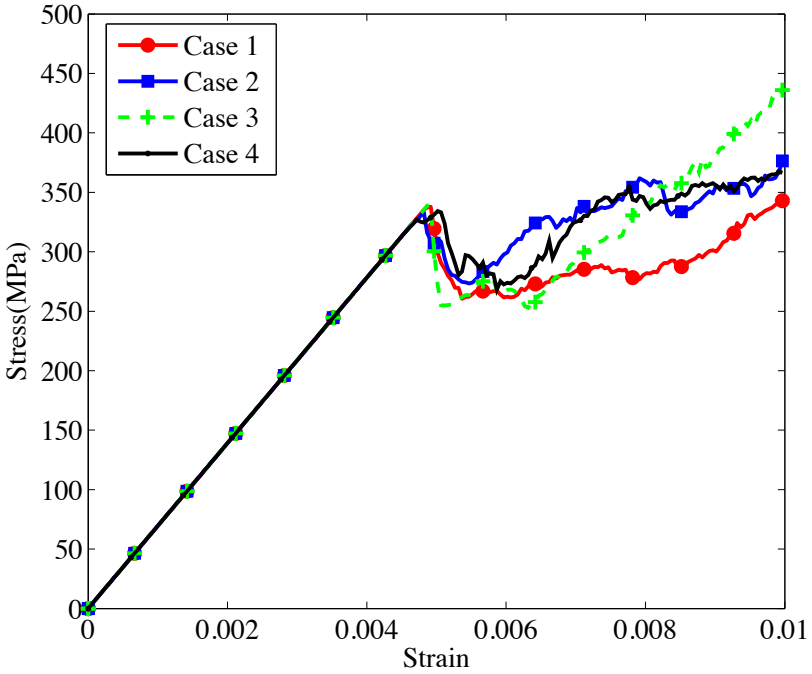

Figure 5.5: The comparison of stress-strain response of different grain orientation.

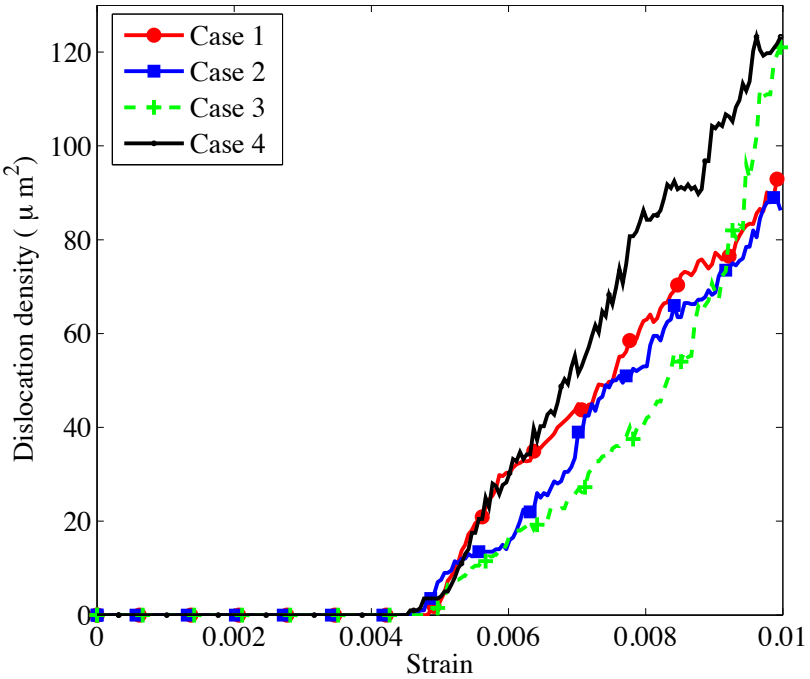

Figure 5.6: The comparison of dislocation density of different grain orientations.

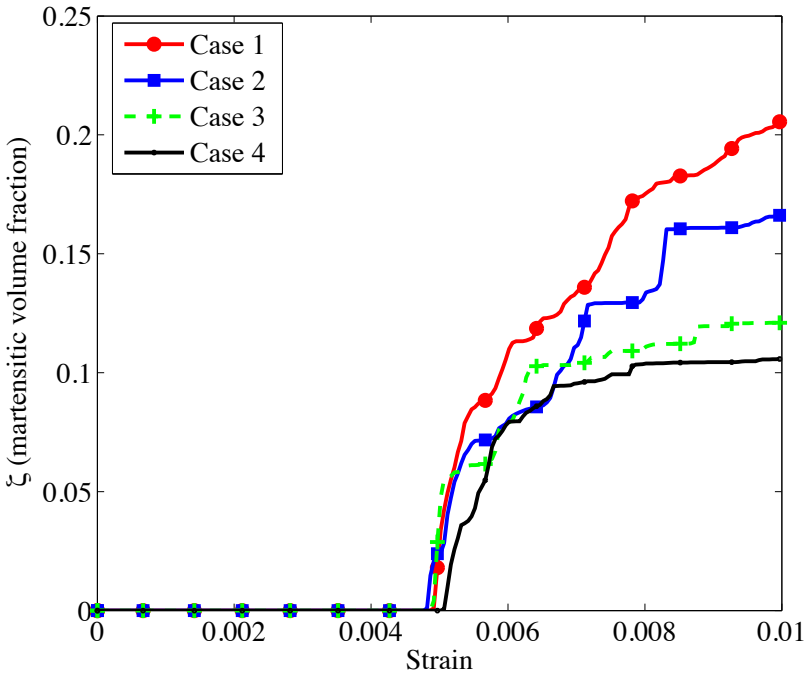

Figure 5.7: The comparison of the martensitic volume fraction of different grain orientation.

As seen in Figure 5.6, the change in dislocation density due to mechanical loading is different for case 1 to case 4. The variation of dislocation density for specimens with different slip orientations is in agreement with the fact that for a grain, the plastic response is orientation dependent. It also means that the dislocation nucleation and motion has different activity in different orientations. Furthermore, the above result confirms that our discrete dislocation-transformation method is able to capture the effect of slip system orientations.

To investigate the effect of transformation system orientations on the mechanical response of the SMA, the change of the martensitic volume fraction for specimens 1 to 4 under isothermal mechanical loading is compared

in Figure 5.7. The value of martensitic volume fraction (ζ) shows how much the martensitic regions grow in each of the cases. Therefore, it can be concluded that the grain orientation has clear effect on the nucleation and growth of the martensitic phase and again our discrete dislocation-transformation framework is able to show the effect of grain orientations on the transformation mechanism.

It is also worth mentioning that although the discussed results in this section show the grain orientation effect, it is not possible to compare the activeness of the different orientations with each other. It is due to the fact that in addition to the grain orientations, other factors such as transformation-plasticity interaction and the computational assumptions also influence on the results. For example, based on the assumption that is explained in previous sections, the dislocations cannot be generated in the martensitic regions. Therefore, specimen 1 which experiences more martensitic transformation in Figure 5.7 has less active sources for the nucleation of dislocations and as a result has a lower dislocation density in Figure 5.6.

Furthermore, the dislocations and martensitic regions distribution as well as average stress in the domain at the end of the loading pass is illustrated in Figure 5.8. As can be seen in this Figures 5.8a to 5.8d, the configuration of dislocations and martensitic regions is clearly different for different orientations.

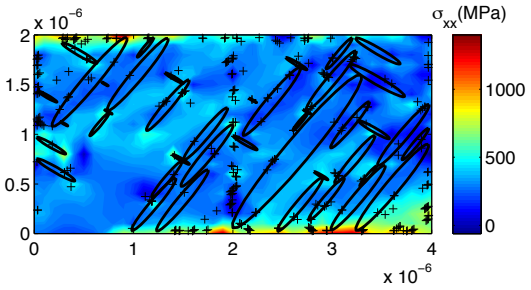

(a)

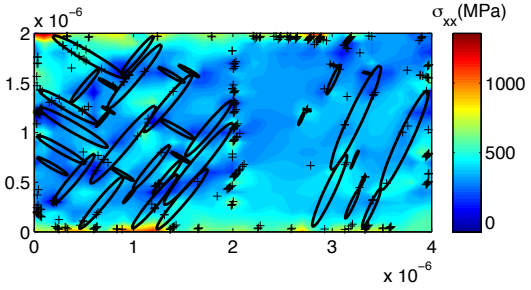

(b)

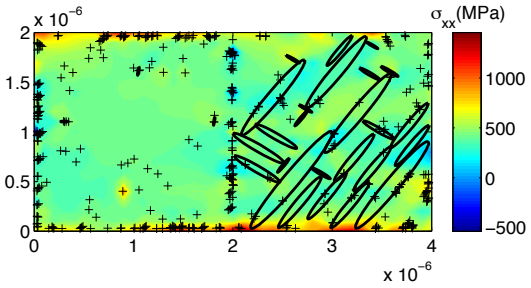

(c)

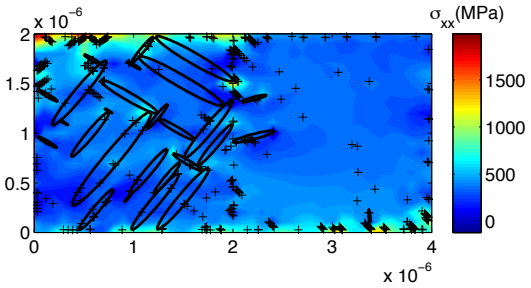

(d)

Figure 5.8: The comparison of average stress contour plot plus dislocations and martensitic distributions at the end of loading path for : (a) Case 1, (b) Case 2, (c) Case 3, and (d) Case 4.

5.2.2 Grain size effect (Hall–Petch effect)

The grain size is another important issue related to the polycrystalline metals. The effect of grain size on the mechanical behavior of metals was first proposed by Hall and Petch [155, 156], therefore the grain size effect is also called "Hall-Petch effect". There are a lot of studies that investigate the grain size effect in polycrystalline structure experimentally and computationally [157–159]. Shi et al. [106] have studied the effect of grain size on the transformation-induced plasticity in TRIP steels by discrete dislocation-transformation model. It was observed that the grain boundaries play the obstacle role against the dislocation motion. It is clear that the smaller grain sizes means higher grain boundary density and more resistance against dislocation motions. Therefore, the finer grain size materials exhibit higher strength behavior in comparison with course grain polycrystalline structure.

In this section the effect of grain size on the mechanical behavior of multi-crystalline NiTi is investigated. The mechanical behavior of NiTi is a combination of plasticity and phase transformation. Therefore, in the following simulations the grain size effect is studied on the martensitic transformation as well as the dislocation plasticity. To do this, three multi-crystalline domains which are made of 4, 9, and 16 square shape grains, respectively, are loaded mechanically under isothermal condition. Furthermore, the orientation of each grain in multi-crystalline structure

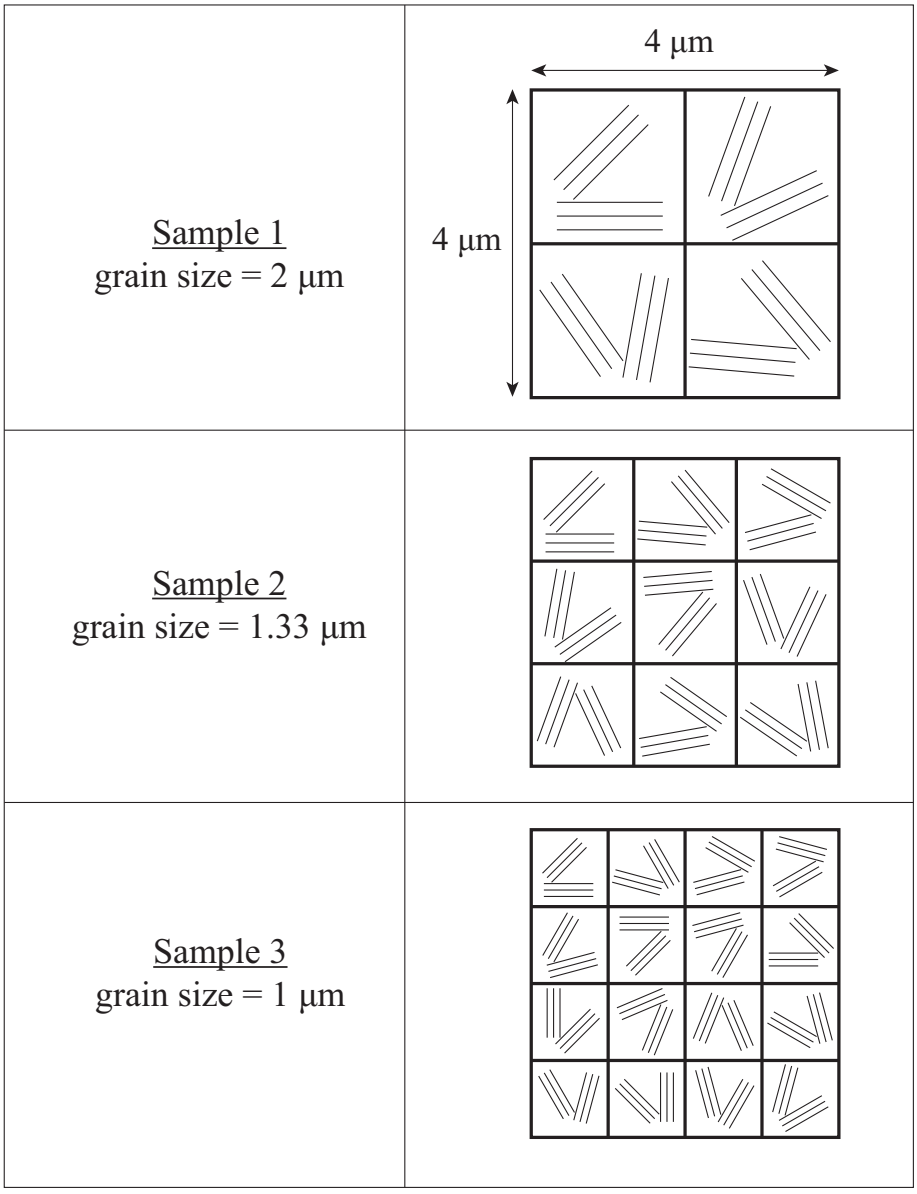

Figure 5.9: The schematic of models to study grain size effect.

are assigned randomly. The schematic of the multi-grain domain to study the Hall-Petch effect is presented in Figure 5.9.

In Figure 5.10, the mechanical response of the three multi-crystalline domains with different grain sizes under isothermal mechanical loading are compared together. As shown in this figure, the specimens with finer grains

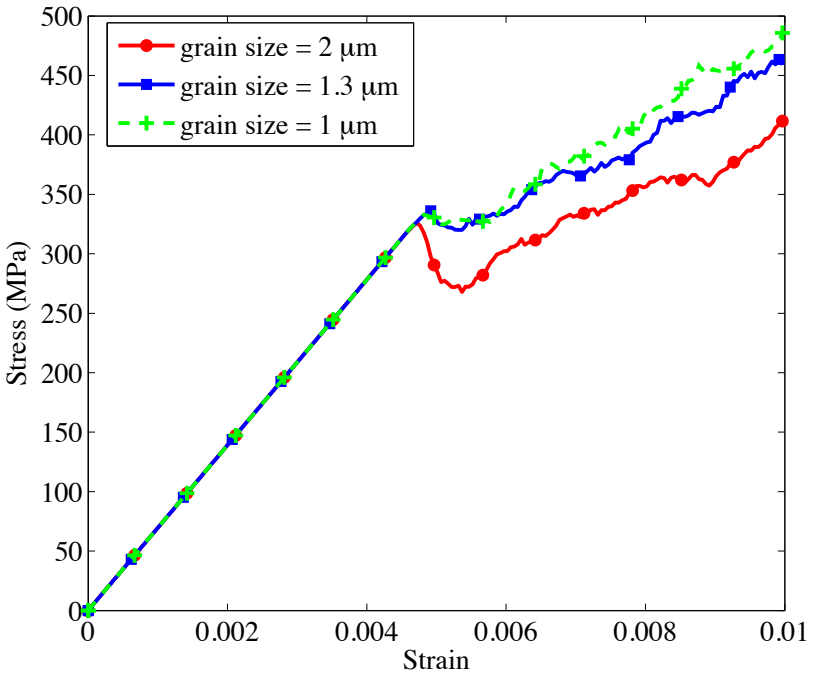

Figure 5.10: Comparison of stress-strain response for different grain sizes.

shows harder mechanical behavior. The small grain sample has higher grain boundary densities; therefore, it shows more resistance against dislocation motion and phase transformation. To have a better understanding about the effect of grain boundaries on the dislocation dynamic and transformation growth, the evolution of dislocation density and martensitic volume fraction are compared for simulations with different grain sizes. These are illustrated in Figures 5.11 and 5.12, respectively.

Fundamentally, work hardening is quantified by increasing the number of dislocations. As can be seen in Figure 5.11, the size of the grains affect the dislocation density in the domain. The smaller grain specimens have more grain boundaries and the likelihood of dislocations reaching the

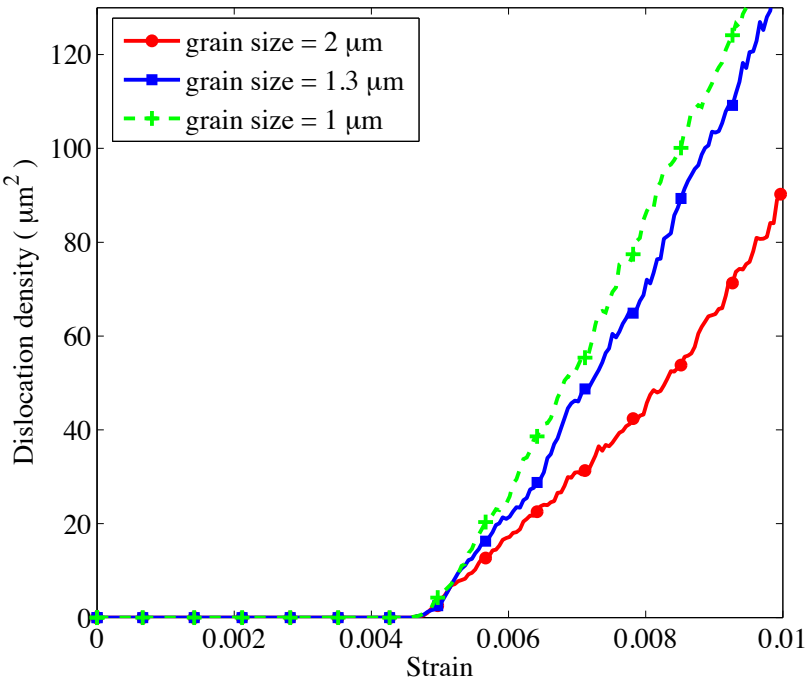

Figure 5.11: Comparison of dislocation density-strain response for different grain sizes.

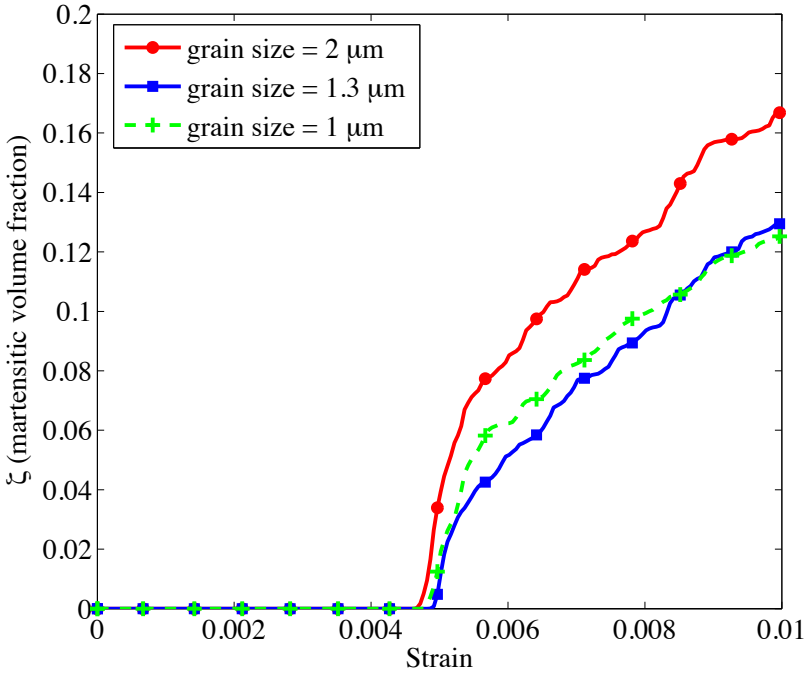

Figure 5.12: Comparison of martensitic volume fraction-strain response for different grain sizes.

grains and having pinned there is increased. Therefore, the sample with higher dislocation density in Figure 5.11 shows harder response in Figure 5.10. This result also confirms that our discrete dislocation-transformation framework has the ability to simulate the Hall-Petch effect in polycrystalline structures.

Figure 5.12 shows the particular effect of grain boundaries on the phase transformation in multi-crystalline NiTi. As illustrated in this figure, the samples with finer grains show less martensitic transformation. This results is in accordance with the assumption which is considered in the beginning of this chapter. Based on this assumption, the martensitic regions stop growing by reaching the grain boundaries. Therefore, the resistance against martensitic growth increases in multi-crystalline samples with smaller grains.

Finally, the average stress contour and the distribution of dislocations and martensitic regions for different samples with different grain sizes are presented in Figure 5.13. As you can see in Figures 5.13a to 5.13c, the sample with finer grains (Sample 3) has more dislocation pile ups in grain boundaries. Moreover, it is observed that the dislocation slip and martensitic transformation are not the same in all the grains. It is due to the different orientations of the grains in multi-crystalline structure.

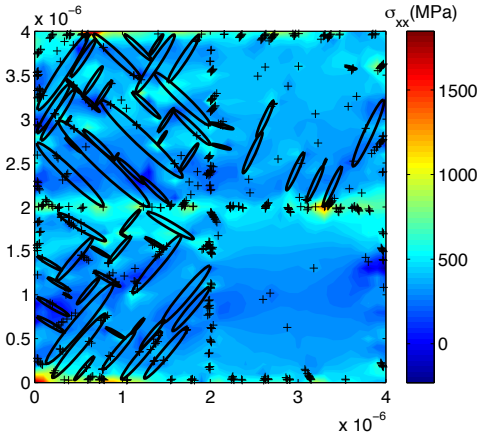

(a)

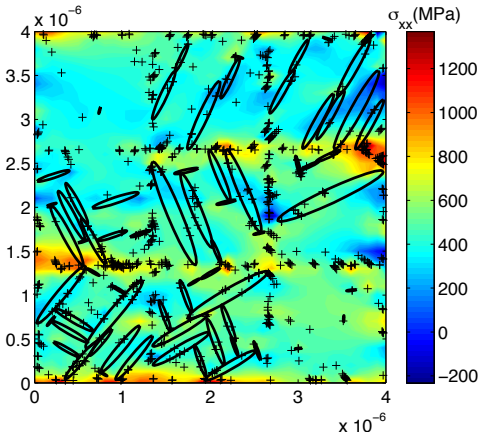

(b)

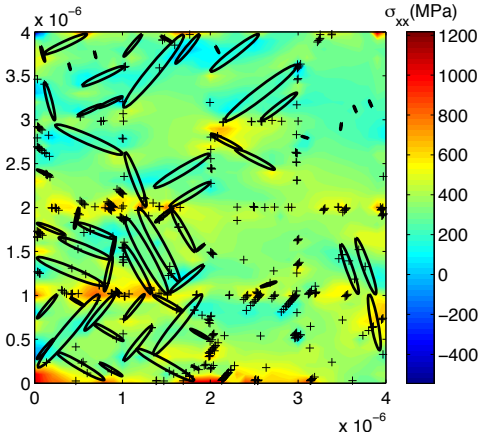

(c)

Figure 5.13: The comparison of average stress contour plot plus dislocations and martensitic distributions at the end of loading path for different grain size samples : (a) grain size=$2\mu m$, (b) grain size=$1.33\mu m$, and (c) grain size=$1\mu m$.

5.3 Thermal cycling loading of multi-crystal NiTi

Similar to the simulation of single-crystalline NiTi, the mechanical behavior of multi-crystalline SMA is studied under thermal cyclic loading and constant external stresses in this section. These simulations are performed to observe the shape memory effect in multi-crystalline NiTi and the effect of grain orientations and grain sizes on this behavior. At first, the orientation dependence of the material under temperature cycling is investigated in Figure 5.14a to 5.14c. In these simulations, four samples with different orientation which are described in Figure 5.4, are cooled from austenite to martensitic phase and then heated back to the initial temperature when they are under constant uni-axial stress.

Furthermore, the dislocation and martensitic regions as well as average stress contour for double-grain samples with different orientations are illustrated in Figure 5.15. These distributions are plotted for the lowest temperature during the thermal cyclic simulation. Similar to isothermal mechanical loading, it can be seen in Figures 5.15a to 5.15d that the distribution of dislocations and martensitic regions are clearly different for samples with different orientations.

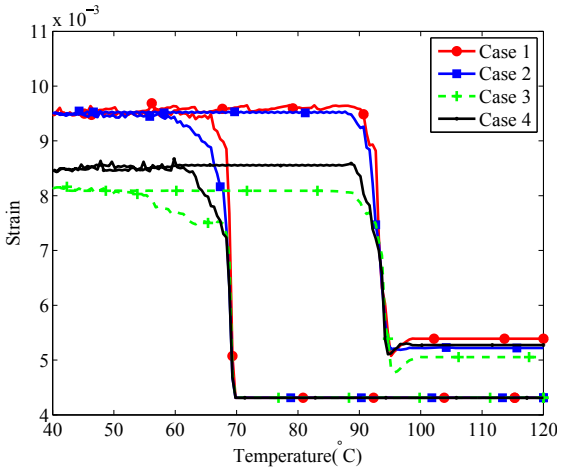

(a)

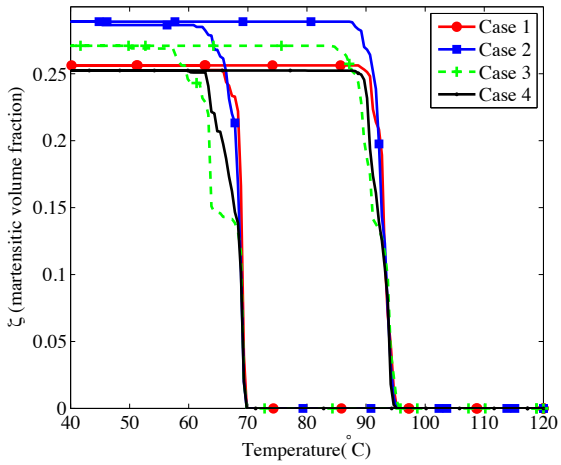

(b)

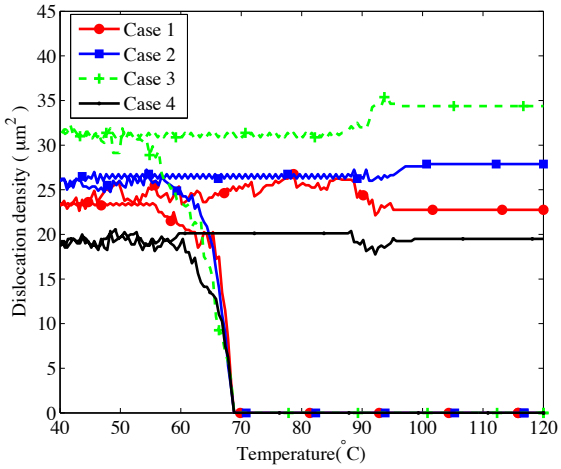

(c)

Figure 5.14: The grain orientation effect on the double grained NiTi under temperature cycling and 300 MPa uni-axial stress.

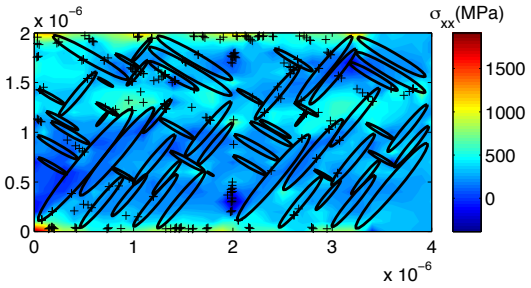

(a)

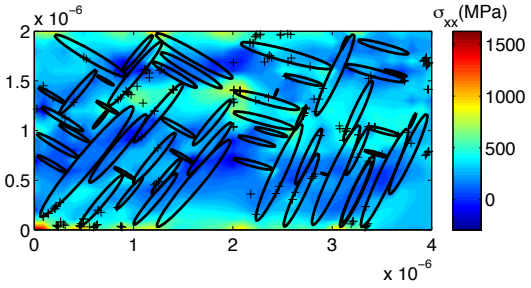

(b)

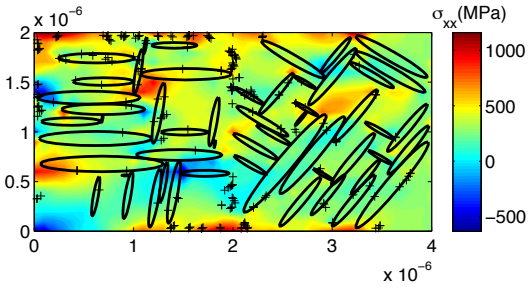

(c)

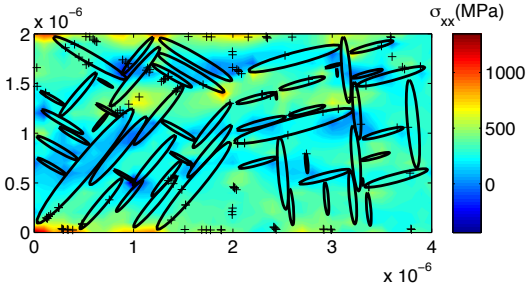

(d)

Figure 5.15: The comparison of average stress contour plot plus dislocations and martensitic distributions at the lowest temperature during thermal cyclic simulations for : (a) Case 1, (b) Case 2, (c) Case 3, and (d) Case 4.

As expected and it is shown in Figure 5.14a, the grain orientation affects

the shape memory response of the multi-crystalline SMA under temperature cyclic loading. Furthermore, Figures 5.14b and 5.14c show the effect of different orientations on the dislocation density and martensitic volume fraction which represent plasticity and transformation mechanisms, respectively. It is observed that the activeness of slip and transformation systems are changed when the grain orientation is changed. However, the grain orientations have more effect on the plasticity mechanism in comparison to transformation mechanisms. The reason is that the mechanical loading (uni-axial applied stress) is the only driving force for the plastic deformation while both thermal and mechanical loadings cause martensitic transformation. It is clear that the thermal driving force in transformation is independent of orientation of the grains.

The grain size effect on thermal cyclic loading of multi-crystalline NiTi is also illustrated in Figures 5.16a to 5.16c. As can be seen in Figure 5.16a, the specimen with larger grain size deformed more than specimens with smaller grain sizes during cooling and heating. Furthermore, to study the grain size effect on both transformation and plasticity mechanisms, the evolution of martensitic volume fraction and dislocation density are compared for different grain sizes in Figures 5.16b and 5.16c, respectively. Furthermore, the average stress contour as well as distribution of dislocations and martensitic regions for different grain sizes are illustrated in Figure 5.17.

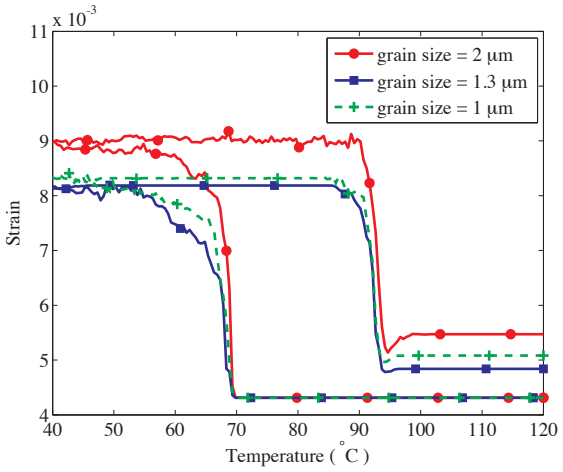

(a)

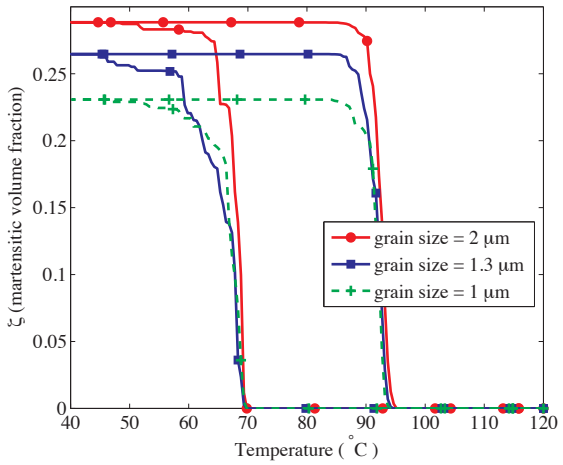

(b)

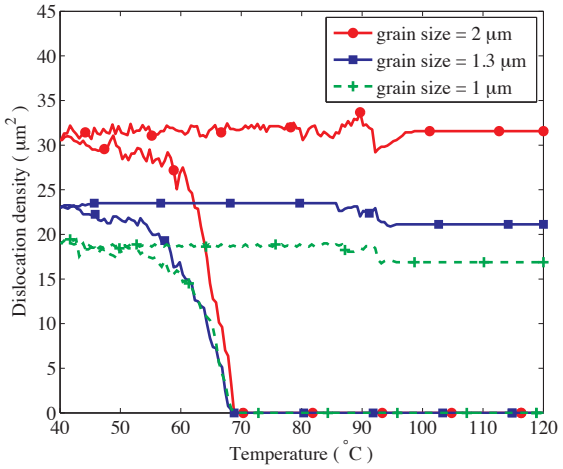

(c)

Figure 5.16: The grain size effect on the shape memory behavior of multi-crystalline NiTi under temperature cyclic loading.

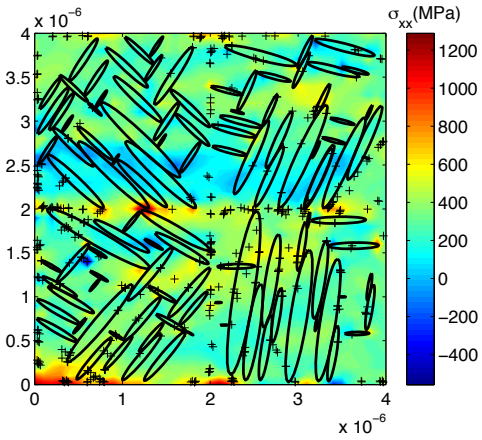

(a)

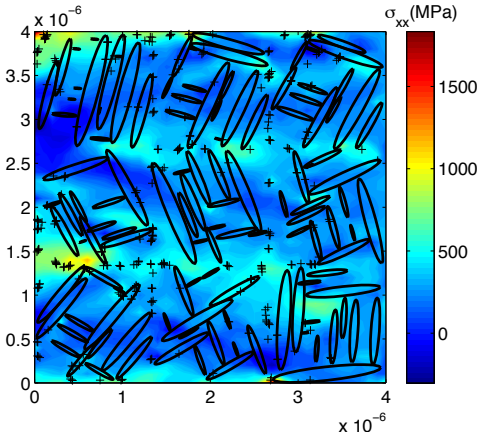

(b)

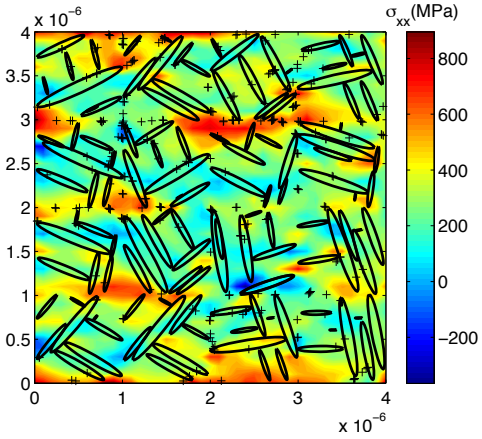

(c)

Figure 5.17: The comparison of average stress contour plot plus dislocations and martensitic distributions at the lowest temperature during temperature cyclic simulation for different grain size samples : (a) grain size=2μm, (b) grain size=1.33μm, and (c) grain size=1μm.

Figure 5.16b represents that the material transformed less in finer grain samples. It is because of the fact that by reducing the size of grains, the density of grain boundaries increased and each grain boundary works as a resistance wall against the growth of transformation interface.

Moreover, Figure 5.16c illustrates that the dislocation density and as a result, plastic strain is higher in specimens with larger grain size. At a glance, it is against the fact that grain boundaries cause the increase of dislocations and hence work hardening. However, looking deeply into Figure 5.16c it is notable that dislocation generation is induced by phase transformation around the temperature of $70°C$ and before martensitic transformation there is no dislocation dynamics. It means that the plastic mechanism here is activated by the local stress field generated by martensitic regions. Therefore, the sample with higher transformation growth (grain size= 2 μm in Figure 5.16b) shows higher dislocation density in Figure 5.16c. For brevity, a simple flowchart of the mechanism happening in these simulations is shown in Figure 5.18.

Finally, the shape memory behavior of a multi-crystalline sample made from nine grains, is studied under temperature cycling and two different uni-axial stresses equal to 50 MPa and 300 MPA. The results are presented in Figure 5.19. As shown in Figures 5.19b and 5.19d, in both models, the martensitic regions transformed back completely by heating to the initial temperature in austenite phase. This means there is no residual strain due

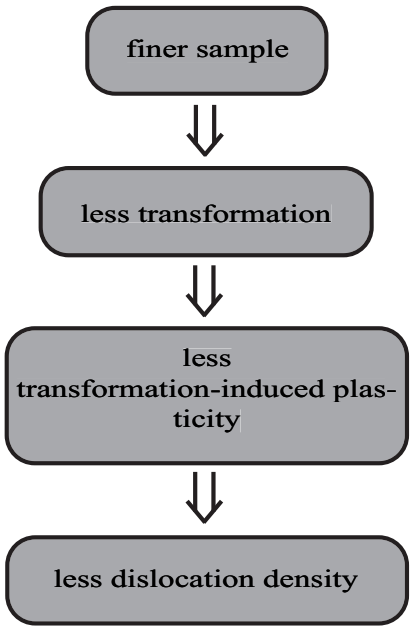

Figure 5.18: A simple flowchart to explain the effects of transformation-induced plasticity and grain size on the dislocation density of the samples when they are under thermal cycling.

to the remaining martensitic phase after thermal cyclic loading. However, Figures 5.19a and 5.19c illustrate some none-reversible strain after thermal cycling in both sample. This remaining strain is due to dislocation plasticity which is induced mainly by the martensitic transformation. It is observed that the plastic strain for the sample under 300 MPa external stress is bigger than that of the sample under 50 MPA applied stress. It is due to the fact that, the Peach-Koehler force (driving force for dislocation generation and motion) is computed by local stress field which is a combination of stress field of martensitic regions (which is similar for both sample) and the external stresses.

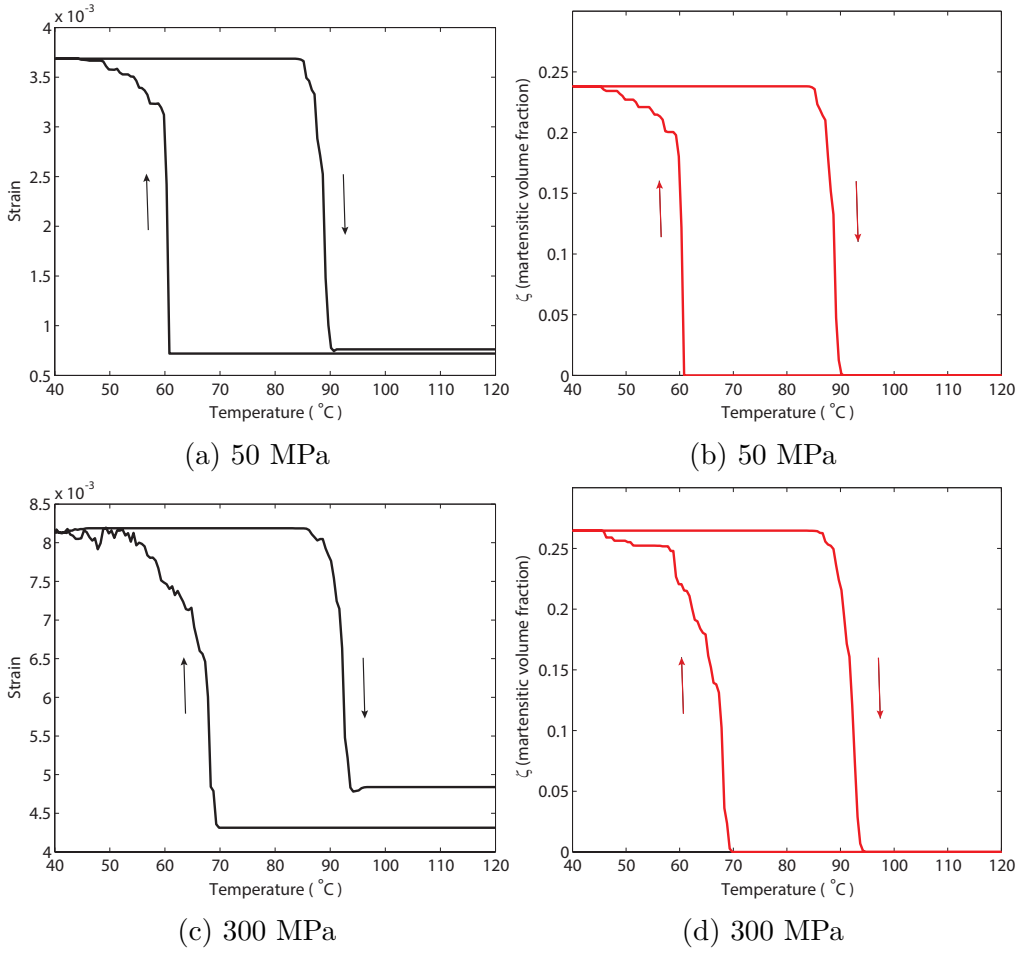

Figure 5.19: The mechanical response of multiple-crystalline NiTi under temperature cycling behavior and different uni-axial applied stress.

5.4 Conclusions

In this chapter the behavior of multi-crystalline SMA under thermo-mechanical loading is studied with the discrete dislocation-transformation model. The orientation effect and grain size effect were investigated when the specimens experienced isothermal mechanical loading and thermal cycling. It is concluded that the grain orientation is an important factor for both transformation and slip systems. Therefore, to reduced the anisotropic behavior

of the model it is crucial to use polycrystalline simulation for larger scales.

Furthermore, as the grain boundaries have a resistance against dislocation motion and martensitic growth, the grain size study is important for predicting the behavior of multi-crystalline SMA. The results in this chapter shows that the material with finer grains shows harder behavior when isothermal mechanical loading is applied. However under temperature cycling loading where the external applied stress is less the than yield stress, the sample with smaller grain shows less dislocation densities. It is due to the fact that, the plastic deformation is induced by the transformation and the specimen with finer grain experienced less transformation, and the grain boundaries in finer grained specimen shows more resistance against the martensitic growth.

Although the multi-crystalline samples in this chapter are limited to domains with maximum 16 grains due to the computational cost, the results show some fundamental phenomenon about polycrystalline structure. Therefore, it can be used for larger scale specimens with more grains in the future.

Chapter 6

Macro scale modeling of shape memory alloys

In the previous chapters, the behavior of single and multi-crystalline shape memory alloy were studied with discrete dislocation-transformation method. The nucleation and motion of dislocations in addition to generation and growth of martensitic regions were modeled in micro-scale domains. Although the discrete dislocation-transformation method described the behavior of SMAs under thermo-mechanical loading well, it is not suitable for modeling the large-scale application of SMAs. In this chapter a three-dimensional constitutive model based on the isotropic plasticity consideration is presented to predict the mechanical behavior of SMAs. This model is also capable simulating the response of SMA at high temperatures with creep as a rate-dependent deformation mechanism being activated.

The constitutive equations are implemented in a finite element program (ABAQUS) by writing an explicit user-material subroutine and then the coupled temperature-displacement problems are solved with this finite element method solver. Then, the results from numerical simulations are compared with experimental data for a ternary high temperature shape memory alloy (Ti-Ni-Pd) during temperature cycling tests under different external stress and different temperature rates. High temperature shape memory alloys (HTSMA) are kinds of SMAs with high transformation temperatures usually above 100°C. The main difference between HTSMAs and ordinary SMAs is the ability of going through this transformation process at higher temperatures and therefore, they extend the application range of these materials to high temperatures such as jet engine and oil and gas industry.

In comparison to the ordinary shape memory alloys, the deformation behavior of HTSMAs is more complicated due to the value of thermal energy at high temperatures. At high temperatures, the yield stress (σ_Y) decreases in both austenite and martensite phases. Therefore, the small resistance to plastic deformation affects the level of irrecoverable strain in HTSMAs. Furthermore, in HTSMAs the transformation temperatures usually lie in the range of 0.3-0.5 of melting temperature where the viscoplastic behavior is observed in metallic materials. Hence, viscoplastisty and transformation occur together at a specific range of temperature and stresses.

Moreover, the internal stresses due to the martensitic transformation may cause transformation-induced plasticity. Recently, some experiments were done on Ti-Pd-Ni alloys and the coexistence of transformation strain and irrecoverable plastic strains were observed [160–163].

It is worth mentioning that although the results from the previous chapters are not used in the continuum model quantitatively, the observation from micro-scale modeling is applied qualitatively to suggest appropriate phenomenological equations for the deformation mechanisms.

6.1 Constitutive equations based on isotropic plasticity

A three dimensional constitutive model is developed in this section to describe the behavior of SMA under thermo-mechanical loading. The isotropic elasto-viscoplasticity theory is used here to model the coexistence of plastic deformation and phase transformation. The proposed model can cover two-way shape memory behavior and super-elasticity but cannot be used for martensitic reorientation/detwinning. For more information about the latter, one can refer to the work of [150].

The governing variable in the constitutive models are taken as: (i) the Helmholtz free energy per reference volume, ψ; (ii) the Cauchy stress, $\mathbf{T}$; (iii) the deformation gradient $\mathbf{F}$ with $(det\mathbf{F}) > 0$; (iv) elastic deformation

gradient, $\mathbf{F}^e$ with $(det\mathbf{F}^e) > 0$; (v) inelastic deformation gradient due to the A$\leftrightarrow$M transformation and plasticity in austenite and martensite, $\mathbf{F}^{inel}$ and we know $\mathbf{F} = \mathbf{F}^e\mathbf{F}^{inel}$; (vi) absolute temperature, θ; (vii) total martensite volume fraction, ξ; with $0 \leq \xi \leq 1$; (viii) heat flux per unit referential area, $\mathbf{q}$.

Furthermore, the continuum body is considered to occupy a region $\mathscr{R}_0$ in reference configuration with $\mathbf{n}_0$ the outward unit normal of the boundary $\partial\mathscr{R}_0$.

As mentioned, the elastic deformation gradient can be found as

$$\mathbf{F}^e = \mathbf{F}\mathbf{F}^{inel^{-1}}, \tag{6.1}$$

and from polar decomposition theory, the elastic deformation gradient can be decompose as elastic stretch and rotation parts,

$$\mathbf{F}^e = \mathbf{R}^e\mathbf{U}^e, \tag{6.2}$$

where $\mathbf{R}^e = \mathbf{R}^{e^{-T}}$ and $\mathbf{U}^e = \mathbf{U}^{e^T}$ are orthogonal elastic rotation tensor and symmetric elastic stretch tensor, respectively. By considering $\mathbf{C}^e = \mathbf{F}^{e^T}\mathbf{F}^e$, the Lagrangian measure of strain is expressed as

$$\mathbf{E}^e = 1/2\left(\mathbf{C}^e - \mathbf{1}\right), \tag{6.3}$$

where $\mathbf{C}^e$ is the elastic right Cauchy-Green strain and $\mathbf{E}^e$ is elastic Green strain tensor.

The total velocity gradient is given by

$$\mathbf{L} \equiv \dot{\mathbf{F}}\mathbf{F}^{-1} = \mathbf{L}^e + \mathbf{F}^e\mathbf{L}^{inel}\mathbf{F}^{e^{-1}}, \tag{6.4}$$

where $\mathbf{L}^e = \dot{\mathbf{F}}^e\mathbf{F}^{e^{-1}}$ is elastic velocity gradient and $\mathbf{L}^{inel} = \dot{\mathbf{F}}^{inel}\mathbf{F}^{inel^{-1}}$ is inelastic velocity gradient. We also decompose $\mathbf{L}^{inel} = \mathbf{D}^{inel} + \mathbf{W}^{inel}$ where $\mathbf{D}^{inel} = Sym\left(\mathbf{L}^{inel}\right)$ is the plastic stretching rate and $\mathbf{W}^{inel} = Skew\left(\mathbf{L}^{inel}\right)$ represents the plastic rotation rate. Furthermore, in the current constitutive equations, some assumption are considered as follows.

(i) According to the work of [164], it is assumed that for isotropic metallic plasticity $\mathbf{W}^{inel} = \mathbf{0}$ means that the inelastic flow is irrotational, and therefore $\mathbf{L}^{inel} = \mathbf{D}^{inel}$.

(ii) It is considered that $(det\mathbf{F}^{inel}) = 1$, $\mathbf{D}^{inel}$ is purely deviatoric.

From second law of thermodynamics $\mathbf{S}\cdot\dot{\mathbf{F}} - \mathbf{q}_0 \cdot \frac{\mathrm{Grad}(\theta)}{\theta} - \dot{\epsilon} + \theta\dot{\eta} \geq 0$, where ϵ is internal energy per unit reference volume and η represents entropy per unit reference volume and by defining $\psi = \epsilon - \eta\theta$ it results in

$$\mathbf{S} \cdot \dot{\mathbf{F}} - \mathbf{q}_0 \cdot \frac{\mathrm{Grad}(\theta)}{\theta} - \dot{\psi} - \eta\dot{\theta} \geq 0, \tag{6.5}$$

and

$$\mathbf{S} \cdot (\dot{\mathbf{F}}^e\mathbf{F}^{inel} + \mathbf{F}^e\dot{\mathbf{F}}^{inel}) - \mathbf{q}_0 \cdot \frac{\mathrm{Grad}(\theta)}{\theta} - \dot{\psi} - \eta\dot{\theta} \geq 0, \tag{6.6}$$

where $\mathbf{S}$ is first Piola Kirchhoff stress tensor and is defined as $\mathbf{S} = (det\mathbf{F})\mathbf{T}\mathbf{F}^{-T}$ where $\mathbf{T}$ is Cauchy stress tensor. Therefore the second law of thermodynamic will be rewritten as:

$$(det\mathbf{F})\,\mathbf{T}\cdot\mathbf{L}^{e} + (det\mathbf{F})\,\mathbf{F}^{e^{T}}\mathbf{T}\mathbf{F}^{e^{-T}}\cdot\mathbf{L}^{inel} - \mathbf{q}_0\cdot\frac{\mathrm{Grad}(\theta)}{\theta} - \dot{\psi} - \eta\dot{\theta} \geq 0. \quad (6.7)$$

It is recalled that $\mathbf{E}^{e} = 1/2\left(\mathbf{F}^{e^{T}}\mathbf{F}^{e} - \mathbf{1}\right)$ and $\dot{\mathbf{E}}^{e} = \mathbf{F}^{e^{T}}\mathbf{D}^{e}\mathbf{F}^{e}$. Therefore, for the first term of second law of thermodynamics in inequality (6.7), it is written as $(det\mathbf{F})\mathbf{T}\cdot\mathbf{L}^{e} = (det\mathbf{F})\mathbf{T}\cdot\mathbf{D}^{e} = (det\mathbf{F})\mathbf{T}\cdot\mathbf{F}^{e^{-T}}\dot{\mathbf{E}}^{e}\mathbf{F}^{e^{-1}}$. Then by defining $\mathbf{T}^{*} = (det\mathbf{F})\mathbf{F}^{e^{-1}}\mathbf{T}\mathbf{F}^{e^{-T}}$ the second law of thermodynamics can be simplified as

$$\mathbf{T}^{*}\cdot\dot{\mathbf{E}}^{e} + \mathbf{C}^{e}\mathbf{T}^{*}\cdot\mathbf{D}^{inel} - \mathbf{q}_0\cdot\frac{\mathrm{Grad}(\theta)}{\theta} - \dot{\psi} - \eta\dot{\theta} \geq 0. \quad (6.8)$$

It is considered in this study that the mechanism of inelastic deformation includes the martensitic transformation, plasticity in austenite phases and also plasticity induced by martensitic transformation. Therefore the inelastic velocity gradient $\mathbf{D}^{inel}$ is decomposed as

$$\mathbf{D}^{inel} = \mathbf{D}^{t} + (1-\xi)\mathbf{D}_{A}^{vp} + \mathbf{D}^{tp}, \quad (6.9)$$

where $\mathbf{D}^{t}$ is *inelastic distortion rate* due to transformation and $\mathbf{D}_{A}^{vp}$ is *inelastic distortion rate* due to plasticity in austenitic phase and $\mathbf{D}^{tp}$ is *dis-*

tortion rate due to the transformation induced plasticity that each of them are defined as

$$\begin{cases} \mathbf{D}^t = \sqrt{\frac{3}{2}}\bar{\varepsilon}^t \sum_{i=1}^{2} \dot{\xi}_i \mathbf{N}_i, \\ \mathbf{D}_A^{vp} = \sqrt{\frac{3}{2}}\dot{\varepsilon}_A^{vp} \mathbf{N}_A, \\ \mathbf{D}^{tp} = \sqrt{\frac{3}{2}}\dot{\varepsilon}^{tp} \mathbf{N}_{tp}, \end{cases} \tag{6.10}$$

where $\dot{\xi}_1 \geq 0$ and $\dot{\xi}_2 \leq 0$ denoted the forward and reverse martensitic transformation rates, respectively, and $\mathbf{N}_1$ and $\mathbf{N}_2$ are forward and reverse flow direction respectively and $\bar{\varepsilon}^t$ is the maximum transformation strain for martensitic transformation which is a physical properties of SMAs.

From the microscopic point of view, the reverse transformation is limited by the forward transformation history to recover the crystallography of the deformation which is induced during forward transformation. Therefore $\mathbf{N}_2$ is defined here based on forward flow direction ($\mathbf{N}_1$) according to [29, 165]:

$$\mathbf{N}_2 = \frac{\mathbf{B}}{|\mathbf{B}|} \qquad \text{with} \qquad \dot{\mathbf{B}} = \mathbf{D}^t. \tag{6.11}$$

Furthermore $\mathbf{N}_A$ is austenite plastic flow directions and $\dot{\epsilon}_A^{vp}$ is the austenitic plastic strain rate and $\dot{\varepsilon}^{tp}$ is transformation induced plastic strain rate. With substitution of decomposed form of $\mathbf{D}^{inel}$ in second law of thermody-

namic, the inequality (6.8) is simplified as

$$\mathbf{T}^* \cdot \dot{\mathbf{E}}^e + \mathbf{C}^e \mathbf{T}^* \cdot \mathbf{D}^t + \mathbf{C}^e \mathbf{T}^* \cdot \left\{ (1-\xi)\mathbf{D}_A^{vp} + \mathbf{D}^{tp} \right\} - \mathbf{q}_0 \cdot \frac{\mathrm{Grad}(\theta)}{\theta} - \dot{\psi} - \eta\dot{\theta} \geq 0. \tag{6.12}$$

The Helmholtz free energy per unit reference volume ψ, is defined as

$$\psi = \widehat{\psi}\left(\mathbf{E}^e, \theta, \xi\right) = \widehat{\psi}^e\left(\mathbf{E}^e, \theta\right) + \widehat{\psi}^\theta\left(\theta\right) + \widehat{\psi}^\xi\left(\theta, \xi\right). \tag{6.13}$$

Therefore, the time derivative of free energy is

$$\dot{\psi} = \frac{\partial \psi}{\partial \mathbf{E}^e} \cdot \dot{\mathbf{E}}^e + \frac{\partial \psi}{\partial \theta}\dot{\theta} + \frac{\partial \psi}{\partial \xi}\dot{\xi}. \tag{6.14}$$

By substituting equation (6.14) in inequality (6.12) and doing some simplification we have

$$\left(\mathbf{T}^* \cdot \dot{\mathbf{E}}^e - \frac{\partial \psi}{\partial \mathbf{E}^e}\right) \cdot \dot{\mathbf{E}}^e - \left(\eta + \frac{\partial \psi}{\partial \theta}\right)\dot{\theta} + \left(\mathbf{C}^e \mathbf{T}^* \cdot \sqrt{\frac{3}{2}}\bar{\varepsilon}^t \sum_{i=1}^{2} \dot{\xi}_i \mathbf{N}_i - \frac{\partial \psi}{\partial \xi}\dot{\xi}\right) + \mathbf{C}^e \mathbf{T}^* \cdot \left\{ (1-\xi)\mathbf{D}_A^{vp} + \mathbf{D}^{tp} \right\} - \mathbf{q}_0 \cdot \frac{\mathrm{Grad}(\theta)}{\theta} \geq 0. \tag{6.15}$$

By using the principle of equipresence it is shown that,

$$\mathbf{T}^* = \frac{\partial \psi}{\partial \mathbf{E}^e}, \tag{6.16}$$

$$\eta = -\frac{\partial \psi}{\partial \theta}, \tag{6.17}$$

$$\left(\mathbf{C}^e\mathbf{T}^* \cdot \sqrt{\frac{3}{2}}\bar{\varepsilon}^t \sum_{i=1}^{2} \dot{\xi}_i \mathbf{N}_i - \frac{\partial \psi}{\partial \xi}\dot{\xi}\right) + \mathbf{C}^e\mathbf{T}^* \cdot \left\{(1-\xi)\mathbf{D}_A^{vp} + \mathbf{D}^{tp}\right\} - \mathbf{q}_0 \cdot \frac{\mathrm{Grad}(\theta)}{\theta} \geq 0. \tag{6.18}$$

Equation (6.16) is the stress-strain constitutive law and equation (6.17) is the constitutive relation for entropy and inequality (6.18) is the total dissipation that is always non-negative. It is assumed that

$$-\mathbf{q}_0 \cdot \frac{\mathrm{Grad}(\theta)}{\theta} \geq 0, \tag{6.19}$$

$$\left(\mathbf{C}^e\mathbf{T}^* \cdot \sqrt{\frac{3}{2}}\bar{\varepsilon}^t \sum_{i=1}^{2} \dot{\xi}_i \mathbf{N}_i - \frac{\partial \psi}{\partial \xi}\dot{\xi}\right) \geq 0, \tag{6.20}$$

$$\begin{cases} \mathbf{C}^e\mathbf{T}^* \cdot \{(1-\xi)\mathbf{D}_A^{vp}\} \geq 0 \\ \mathbf{C}^e\mathbf{T}^* \cdot \mathbf{D}^{tp} \geq 0. \end{cases} \tag{6.21}$$

Inequality (6.19) is the dissipation due to heat conduction and inequality (6.20) is the dissipation due to phase transformation and finally inequalities (6.21) are the dissipation due to austenite plastic deformation and transformation induced plasticity.

In this study, the Helmholtz free energy density, $\psi = \widehat{\psi}\left(\mathbf{E}^e, \theta, \xi\right)$ is considered to be constructed of three parts,

$$\psi = \widehat{\psi}\left(\mathbf{E}^e, \theta, \xi\right) = \widehat{\psi}^e\left(\mathbf{E}^e, \theta\right) + \widehat{\psi}^\theta\left(\theta\right) + \widehat{\psi}^\xi\left(\theta, \xi\right). \tag{6.22}$$

Then the terms of the Helmholtz free energy per unit reference volume, ψ is assumed in the forms of

$$\widehat{\psi}^{e}\left(\mathbf{E}^{e},\theta\right)=\frac{1}{2}\mathbf{E}^{e}\cdot\mathbb{C}\left[\mathbf{E}^{e}\right]-\mathbf{A}\left(\theta-\theta_{0}\right)\cdot\mathbb{C}\left[\mathbf{E}^{e}\right], \tag{6.23}$$

$$\widehat{\psi}^{\theta}\left(\theta\right)=c\left(\theta-\theta_{0}\right)-c\theta\ln\left(\frac{\theta}{\theta_{0}}\right), \tag{6.24}$$

$$\widehat{\psi}^{\xi}\left(\theta,\xi\right)=\frac{\lambda_{T}}{\theta_{T}}\left(\theta-\theta_{T}\right)\xi+\frac{1}{2}h\xi^{2}. \tag{6.25}$$

Here $\widehat{\psi}^{e}$ denotes the classical thermo-elastic free energy density, where $\mathbb{C}$ is the symmetric forth-order elastic modulus tensor, $\mathbf{A}$ is the symmetric second order thermal expansion tensor and θ_0 is the reference temperature. Furthermore, $\widehat{\psi}^{\theta}$ is thermal portion of free energy density where c is the specific heat per unit volume. Finally, $\widehat{\psi}^{\xi}$ represents the austenite/martensite phase transformation energy where λ_T is the latent heat of phase transformation, h is the transformation hardening factor and $\theta_T = \frac{M_s+A_s}{2}$ is transformation temperature and M_s is the martensite start temperature and A_s is the austenite start temperature.

From equation (6.16), the stress measurement $\mathbf{T}^{*}$ is presented by

$$\mathbf{T}^{*}=\frac{\partial\psi}{\partial\mathbf{E}^{e}}=\mathbb{C}\left(\mathbf{E}^{e}-\mathbf{A}\left(\theta-\theta_{0}\right)\right). \tag{6.26}$$

Substituting equation (6.22) in equation (6.17), the constitutive equation

for entropy density is found as

$$\eta = -\frac{\partial \psi}{\partial \theta} = \mathbf{A} \cdot \mathbb{C}\left[\mathbf{E}^e\right] + c\theta \ln\left(\frac{\theta}{\theta_0}\right) - \frac{\lambda_T}{\theta_T}\xi. \tag{6.27}$$

It is assumed that the material obeys Fourier's law of heat conduction therefore, from $-\mathbf{q}_0 \cdot \frac{\mathrm{Grad}(\theta)}{\theta} \geq 0$ it is expressed as

$$\mathbf{q}_0 = -\mathbf{K}\mathrm{Grad}(\theta), \tag{6.28}$$

where $\mathbf{K}$ is the thermal conductivity tensor.

The other dissipation parts presented in inequalities (6.20) and (6.21) are due to the martensitic transformation and the plasticity in austenitic phase and the plasticity due to phase transformation respectively. For dissipation because of transformation, $\left(\mathbf{C}^e\mathbf{T}^* \cdot \sqrt{\frac{3}{2}}\bar{\varepsilon}^t \sum_{i=1}^{2} \dot{\xi}_i \mathbf{N}_i - \frac{\partial \psi}{\partial \xi}\dot{\xi}\right) \geq 0$ it is shown as

$$f_1\dot{\xi}_1 \geq 0 \qquad \text{whenever} \qquad \dot{\xi}_1 \neq 0, \tag{6.29}$$

where $f_1 \equiv \left(\sqrt{\frac{3}{2}}\bar{\varepsilon}^t \left(\mathbf{C}^e\mathbf{T}^*\right) \cdot \mathbf{N}_1 - \frac{\partial \psi}{\partial \xi}\right)$ denotes the driving force for forward transformation, and

$$f_2\dot{\xi}_2 \geq 0 \quad \text{whenever} \quad \dot{\xi}_2 \neq 0, \tag{6.30}$$

where $f_2 \equiv \left(\sqrt{\frac{3}{2}}\bar{\varepsilon}^t \left(\mathbf{C}^e\mathbf{T}^*\right) \cdot \mathbf{N}_2 - \frac{\partial \psi}{\partial \xi}\right)$ denotes the driving force for reverse transformation. As mentioned before, we have assumed that $det(\mathbf{F}^{inel}) = 1$,

therefore $\mathbf{D}^{inel}$, $\mathbf{D}^{t}$, $\mathbf{D}_{A}^{vp}$, and $\mathbf{D}^{tp}$ are purely deviatoric and as a result the inequalities (6.29) and (6.30) are rewritten as

$$f_1 \equiv \left(\sqrt{\frac{3}{2}} \bar{\varepsilon}^t dev\left(\mathbf{C}^e \mathbf{T}^*\right) \cdot \mathbf{N}_1 - \frac{\lambda_T}{\theta_T}\left(\theta - \theta_T\right) - h\xi \right), \tag{6.31}$$

$$f_2 \equiv \left(\sqrt{\frac{3}{2}} \bar{\varepsilon}^t dev\left(\mathbf{C}^e \mathbf{T}^*\right) \cdot \mathbf{N}_2 - \frac{\lambda_T}{\theta_T}\left(\theta - \theta_T\right) - h\xi \right). \tag{6.32}$$

It is considered that $f_{1,2} = f_c \widehat{g}\left(\dot{\xi}\right)$ where, $\widehat{g}\left(\dot{\xi}\right) > 0$ for $\dot{\xi} > 0$ and $\widehat{g}\left(\dot{\xi}\right) < 0$ for $\dot{\xi} < 0$, then since $|\mathbf{N}_i| = 1$ it is shown as

$$\sqrt{\frac{3}{2}} \bar{\varepsilon}^t dev\left(\mathbf{C}^e \mathbf{T}^*\right) \cdot \mathbf{N}_1 = \frac{\lambda_T}{\theta_T}\left(\theta - \theta_T\right) + h\xi + f_c \widehat{g}\left(\dot{\xi}\right), \tag{6.33}$$

therefore,

$$\sqrt{\frac{3}{2}} \bar{\varepsilon}^t dev\left(\mathbf{C}^e \mathbf{T}^*\right) = \left\{ \frac{\lambda_T}{\theta_T}\left(\theta - \theta_T\right) + h\xi + f_c \widehat{g}\left(\dot{\xi}\right) \right\} \mathbf{N}_1. \tag{6.34}$$

Since $|\mathbf{N}_1| = 1$, taking the magnitude on both sides of equation (6.34) it is obtained

$$\mathbf{N}_1 = \frac{dev\left(\mathbf{C}^e \mathbf{T}^*\right)}{\left|dev\left(\mathbf{C}^e \mathbf{T}^*\right)\right|}, \tag{6.35}$$

and

$$\overline{\sigma}\bar{\varepsilon}^t - \frac{\lambda_T}{\theta_T}\left(\theta - \theta_T\right) - h\xi = f_c \widehat{g}\left(\dot{\xi}\right), \tag{6.36}$$

where $\overline{\sigma} = \left| \sqrt{\frac{3}{2}} dev\left(\mathbf{C}^e \mathbf{T}^*\right) \right|$ and $f_{1,2}$ is defined as driving force for forward

and reverse phase transformation,

$$f_{1,2} = \overline{\sigma}\bar{\varepsilon}^t - \frac{\lambda_T}{\theta_T}(\theta - \theta_T) - h\xi. \tag{6.37}$$

According to work done by [166] on the rate-dependent and isotropic metal plasticity the $\widehat{g}\left(\dot{\xi}\right)$ is assumed in the form of

$$\widehat{g}\left(\dot{\xi}\right) = \left(\frac{\left|\dot{\xi}\right|}{\dot{\xi}_0}\right)^{m-1}\left(\frac{\dot{\xi}}{\dot{\xi}_0}\right). \tag{6.38}$$

Therefore, the kinetic relation for martensitic volume fraction ξ is determined as

$$\dot{\xi} = sign\,(f)\,\dot{\xi}_0\left(\frac{|f|}{f_c}\right)^{\frac{1}{m}}, \tag{6.39}$$

where m is the rate sensitivity factor for phase transformation, $\dot{\xi}_0 > 0$ is the reference martensite or austenite generation rate and f_c is the resistance to transformation.

For the dissipation part due to plasticity in austenite and transformation induced plasticity, $\mathbf{C}^e\mathbf{T}^* \cdot \left\{(1-\xi)\mathbf{D}_A^{vp} + \mathbf{D}^{tp}\right\} \geq 0$, it is considered that

$$det(\mathbf{F}_A^{vp}) = 1 \quad \Rightarrow \quad trace(\mathbf{D}_A^{vp}) = 0 \quad \Rightarrow \quad \mathbf{D}_A^{vp} = dev(\mathbf{D}_A^{vp}),$$

$$det(\mathbf{F}^{tp}) = 1 \quad \Rightarrow \quad trace(\mathbf{D}^{tp}) = 0 \quad \Rightarrow \quad \mathbf{D}_M^{tp} = dev(\mathbf{D}^{tp}).$$

Therefore, the inequality (6.21) is rewritten as

$$\begin{cases} \left(\mathbf{C}^e\mathbf{T}^*\right)_{dev} \cdot \left(\mathbf{D}_A^{vp}\right)_{dev} \geq 0, \\ \left(\mathbf{C}^e\mathbf{T}^*\right)_{dev} \cdot \left(\mathbf{D}^{tp}\right)_{dev} \geq 0. \end{cases} \tag{6.40}$$

To solve inequalities (6.40) it is considered that, $\mathbf{N}_A = \mathbf{N}_{tp} = \mathbf{N}_3$ therefore

$$\begin{cases} \left(\mathbf{D}_A^{vp}\right)_{dev} = k\dot{\bar{\epsilon}}_A^p \mathbf{N}_3, \\ \left(\mathbf{D}^{tp}\right)_{dev} = k\dot{\bar{\epsilon}}^{tp} \mathbf{N}_3. \end{cases} \tag{6.41}$$

and

$$\left(\mathbf{C}^e\mathbf{T}^*\right)_{dev} = \left\{(1-\xi)k\dot{\bar{\epsilon}}_A^p + k\dot{\bar{\epsilon}}^{tp}\right\}\mathbf{N}_3, \tag{6.42}$$

also as $|\mathbf{N}_3|$=1. Hence,

$$\left|\left(\mathbf{C}^e\mathbf{T}^*\right)_{dev}\right| = \left\{(1-\xi)k\dot{\bar{\varepsilon}}_A^p + k\dot{\bar{\varepsilon}}^{tp}\right\}, \tag{6.43}$$

and

$$\mathbf{N}_3 = \frac{\left(\mathbf{C}^e\mathbf{T}^*\right)_{dev}}{\left|\left(\mathbf{C}^e\mathbf{T}^*\right)_{dev}\right|}. \tag{6.44}$$

As the plastic mechanisms in austenite phase is fully dissipative it is obtained that

$$\begin{cases} \overline{\tau}\left(\dot{\bar{\varepsilon}}_A^p\right) > 0, \\ \overline{\tau}\left(\dot{\bar{\varepsilon}}^{tp}\right) > 0. \end{cases} \tag{6.45}$$

where $\overline{\tau} = k\left|(\mathbf{C}^e\mathbf{T}^*)_{dev}\right|$, $k = \sqrt{\frac{3}{2}}$, and $\dot{\overline{\varepsilon}}^p_A$ and $\dot{\overline{\varepsilon}}^{tp}$ are plastic strain rate. Then to specify the kinetic rate-dependent relation for isotropic metal plasticity, it is defined that

$$\overline{\tau} = \frac{S_a}{\left[exp\left(\frac{-Q_a}{R\theta}\right)\right]^n}\left(\frac{\dot{\overline{\varepsilon}}^p_A}{\dot{\varepsilon}_0}\right)^{(n-1)}\left(\frac{\dot{\overline{\varepsilon}}^p_A}{\dot{\varepsilon}_0}\right). \tag{6.46}$$

Therefore, the kinetic equation to find plastic strain in austenitic phase is expressed as

$$\dot{\overline{\varepsilon}}^p_A = \dot{\varepsilon}_0 sign\left(\overline{\tau}\right)\left(\frac{\overline{\tau}}{S_a}\right)^{\frac{1}{n}} exp\left(\frac{-Q_a}{R\theta}\right), \tag{6.47}$$

where n is rate sensitivity factor, $\dot{\varepsilon}_0$ is the reference strain rate, Q_A is the activation energy for austenite and R is the Stefan-Boltzmann constant and S_a is the plastic resistance in austenite phase.

The kinetic equation to predict the plastic strain rate that is occurred due to the martensitic transformation is suggested by Leblond [167] as

$$\dot{\overline{\varepsilon}}^{tp} = \dot{\varepsilon}^{tp}_0\left(\frac{\overline{\tau}}{S_a}\right), \tag{6.48}$$

where

$$\dot{\varepsilon}^{tp}_0 = \delta\dot{\phi}\left(\xi\right)g\left(\overline{\tau}\right), \tag{6.49}$$

where δ is volumetric change of crystals between austenitic and martensitic phases and is found by microstructure calculation on crystals. $\phi\left(\xi\right)$ is a function of martensitic volume fraction which increase from zero to one

during transformation from austenite to martensite and is assumed as: $\phi(\xi) = \xi(1 - \ln \xi)$ and $g(\overline{\tau})$ is a function to describe the nonlinearity of relation between $\dot{\varepsilon}_0^{tp}$ and $\overline{\tau}$ and is suggested by Leblond [167] as

$$g(\overline{\tau}) = \begin{cases} 1 \quad if \quad \frac{\overline{\tau}}{S_a} < \frac{1}{2}, \\ 1 + a\left(\frac{\overline{\tau}}{S_a} - \frac{1}{2}\right), \qquad \text{if} \qquad \frac{\overline{\tau}}{S_a} > \frac{1}{2}. \end{cases} \tag{6.50}$$

A model to update the plasticity resistance of austenite phase is defined as

$$\dot{S}_a = d_{2a}\dot{\bar{\varepsilon}}_A^p, \tag{6.51}$$

From the first law of thermodynamics, $\mathbf{S} \cdot \dot{\mathbf{F}} - \mathrm{Div}\mathbf{q}_0 + r = \dot{\epsilon}$ and since $\epsilon = \psi + \eta\theta$ and $\dot{\epsilon} = \dot{\psi} + \dot{\eta}\theta + \eta\dot{\theta}$ it is obtained that

$$\mathbf{S} \cdot \dot{\mathbf{F}} - \mathrm{Div}\mathbf{q}_0 + r - \dot{\psi} - \dot{\eta}\theta - \eta\dot{\theta} = 0. \tag{6.52}$$

where r is the heat supply per unit reference volume. Then with substituting the terms and doing some simplification, it will be

$$\begin{aligned} &\left(\mathbf{T}^* - \frac{\partial\psi}{\partial\mathbf{E}^e}\right) \cdot \dot{\mathbf{E}}^e - \left(\eta + \frac{\partial\psi}{\partial\theta}\right)\dot{\theta} + \Bigg(\mathbf{C}^e\mathbf{T}^* \cdot \\ &\sqrt{\frac{3}{2}}\bar{\varepsilon}^t \sum_{i=1}^{2} \dot{\xi}_i \mathbf{N}_{\mathrm{i}} - \frac{\lambda_T}{\theta_T}(\theta - \theta_T)\dot{\xi} - h\xi\dot{\xi}\Bigg) + \\ &\mathbf{C}^e\mathbf{T}^* \cdot \left\{(1 - \xi)\mathbf{D}_A^{vp} + \mathbf{D}^{tp}\right\} - \mathrm{Div}\mathbf{q}_0 + r = \dot{\eta}\theta, \end{aligned} \tag{6.53}$$

and it is reduced to

$$\left(\mathbf{C}^e\mathbf{T}^* \cdot \sqrt{\frac{3}{2}}\bar{\varepsilon}^t \sum_{i=1}^{2} \dot{\xi}_i \mathbf{N}_{\mathrm{i}} - \frac{\lambda_T}{\theta_T}\left(\theta - \theta_T\right)\dot{\xi} - h\xi\dot{\xi}\right) + \mathbf{C}^e\mathbf{T}^* \cdot \left\{(1-\xi)\mathbf{D}_A^{vp} + \mathbf{D}^{tp}\right\} - \mathrm{Div}\mathbf{q}_0 + r = \dot{\eta}\theta. \tag{6.54}$$

Then the rate of entropy is found by the constitutive equation (6.27)

$$\dot{\eta} = \overbrace{\mathbf{A} \cdot \mathbb{C}\left[\mathbf{E}^e\right] + c\ln\left(\frac{\theta}{\theta_0}\right) - \frac{\lambda_T}{\theta_T}\xi}^{\cdot} = \mathbf{A} \cdot \mathbb{C}\left[\dot{\mathbf{E}}^e\right] + c\frac{\dot{\theta}}{\theta} - \frac{\lambda_T}{\theta_T}\dot{\xi}, \tag{6.55}$$

and by substituting equation (6.55) in equation (6.54) it is obtained

$$c\dot{\theta} = -\mathbf{A} \cdot \mathbb{C}\left[\dot{\mathbf{E}}^e\right]\theta - \mathrm{Div}\mathbf{q}_0 + r + \left(\mathbf{C}^e\mathbf{T}^* \cdot \sqrt{\frac{3}{2}}\bar{\varepsilon}^t \sum_{i=1}^{2} \dot{\xi}_i \mathbf{N}_{\mathrm{i}} - \frac{\lambda_T\theta}{\theta_T}\dot{\xi} - h\xi\dot{\xi}\right) + \mathbf{C}^e\mathbf{T}^* \cdot \left\{(1-\xi)\mathbf{D}_A^{vp} + \mathbf{D}^{tp}\right\}, \tag{6.56}$$

where the first term is the elastic heat generation, the second term is the heat conduction, the third is the heat source, the fourth term is because of transformation dissipation and finally the last term is the plastic dissipation in the austenitic phase.

A time integration algorithm is developed to implement constitutive equations for SMAs in ABAQUS/Explicit by writing an explicit user material subroutine (VUMAT). The time integration algorithm using for implementation code is presented in appendix A.

6.2 Calibration of the model

The material which is used in this section for the model is a shape memory alloy with the composition of $Ti_{50}Pd_{30}Ni_{20}$. This material is selected because of its transformation temperature which is as follow: martensitic finish = 223°C, martensitic start = 234°C, austenitic start = 235°C and austenitic finish = 245°C [162]. These transformation temperatures are between 200°C and 300°C, which lie in the range of 0.3-0.35 of the alloy's melting temperature. It is shown that in this range of temperature, the creep mechanism in metallic alloys is activated [11, 168].

To study the actuation behavior of $Ti_{50}Pd_{30}Ni_{20}$, it is crucial to investigate the occurrence of martensitic transformation and plasticity simultaneously during thermal cycling loads. Some of the material parameters are defined based on the literatures [162, 163] and some of them have been found by fitting the results from one dimensional constitutive equations by the uni-axial thermal cycling experiments. Figure 6.1 and 6.2 show these comparisons at 100 MPa and 300 MPa external applied stresses and thermal changes between 370°C and 100°C to the find fitting parameters where the temperature rate during cooling and heating is 5 $\frac{^{\circ}C}{min}$. A summary of all material constants and fitting parameters for $Ti_{50}Pd_{30}Ni_{20}$ is presented in Table 6.1. This data is used for the three dimensional simulation to model the coexistence of phase transformation and plasticity during thermal actuation behavior.

Table 6.1: Material Parameters of $Ti_{50}Pd_{30}Ni_{20}$.

Thermo elastic behavior [162]
$E_A = 32GPa$ $E_M = 57GPa$
$\nu_A = \nu_M = 0.33$ $\alpha_A = \alpha_M = 2.5 \times 10^{-5} 1/°C$
Transformation properties [162, 163]
$\bar{\varepsilon}^t \approx 0.015$ Latent heat:$\lambda_T = 58.6MJ/m^3$
$M_f = 223°C$ $M_s = 234°C$ $A_s = 235°C$ $A_f = 245°C$
$m = 0.02$ $\dot{\xi}_0 = 0.001$ $h = 7$
Plasticity in Austenite [162]
$n = 0.24$ $Q_a = 263KJ/mol$ $\varepsilon_0 = 10^6$ $R = 0.00831$
$S_A = 300$ MPa
Transformation induced Plasticity
$\delta = 0.0067$ $a = 2$

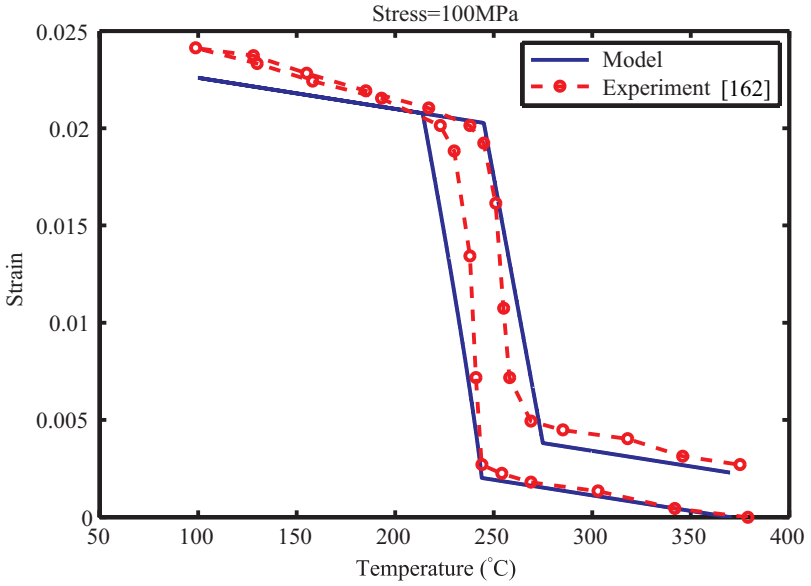

Figure 6.1: comparison of strain-temperature behavior of the $Ti_{50}Pd_{30}Ni_{20}$ specimen thermally cycled at 100 MPa applied stress.

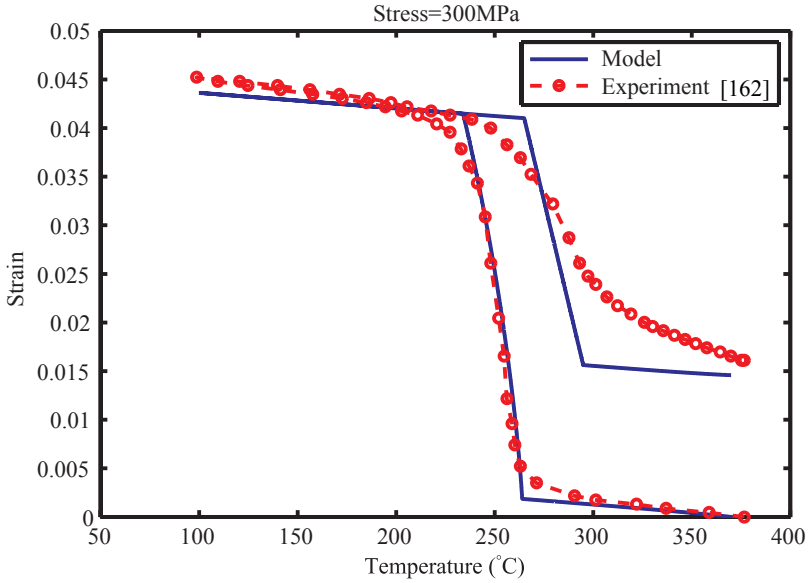

Figure 6.2: comparison of strain-temperature behavior of the $Ti_{50}Pd_{30}Ni_{20}$ specimen thermally cycled at 300 MPa applied stress.

6.3 Three-dimensional computational analysis

The coupled temperature-displacement simulations are modeled by using finite element in ABAQUS software to observe the actuation behavior of $Ti_{50}Pd_{30}Ni_{20}$. It includes the coexistence of martensitic transformation, plasticity in austenite, and transformation induced plasticity (TRIP). The cylindrical specimens and spring coil are the three-dimensional examples which are presented in the next sections.

6.3.1 Example 1: Cylinder under thermal cycling

This problem consists of compression loading of a solid cylinder with $7mm$ diameter and $14mm$ height and it is in accordance with experimental data available. In these experiments, each specimen was heated to $100°C$ under no-load condition and subsequently loaded to the desired stress level in the martensitic state. The specimen was then heated to a temperature of $370°C$ while holding the stress constant. From this point, three consecutive thermal cycles were conducted by cooling and subsequently heating the specimen between 100 and $370°C$ [162]. The grips are considered as rigid surfaces and the Abaqus contact algorithm is applied to model the grip-cylinder contact. The friction coefficient is assumed as 0.2 and the external stress is applied on the rigid grips. Finally the temperature is changed at the rate of $5\ °C/min$ on the external surfaces. The schematic of the three-dimensional model of cylinder which is under thermal cycling and constant compression stress along the axial direction is presented in Figure 6.3.

The cylindrical specimens are under temperature cyclic loading between 370°C and 100°C with the temperature rate of $5°C/min$ when they are under compression with applied stresses of 50 MPa, 100 MPa, 200 MPa, 300 MPa and 400 MPa for different tests. The comparison of strain-temperature response that is predicted by the three dimensional simulations and experiments for different applied stresses is presented in Figures 6.4 to 6.8.

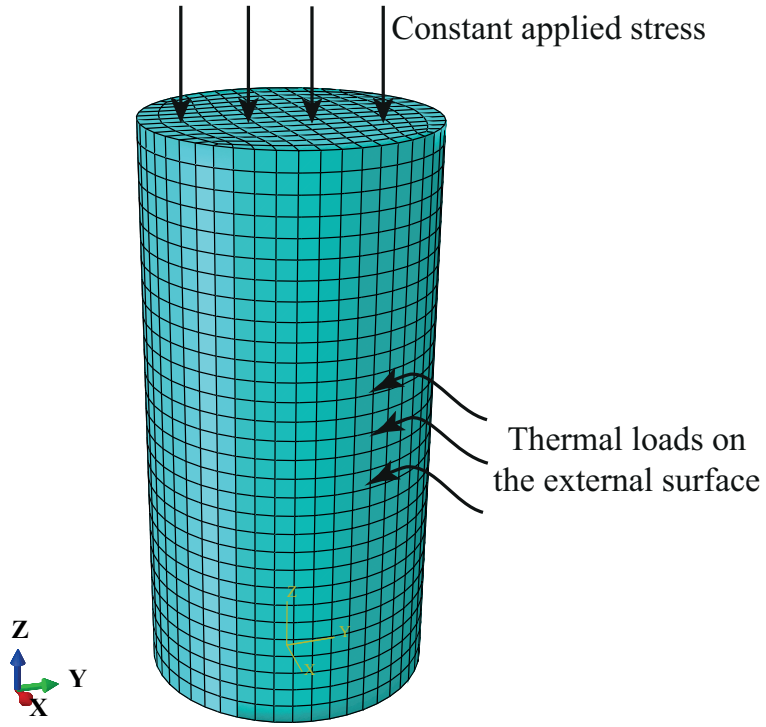

Figure 6.3: 3D view of cylinder model to study the behavior of the $Ti_{50}Pd_{30}Ni_{20}$ specimen thermally cycled at 200 MPa applied stress on axial direction and temperature rate of $5°C/min$.

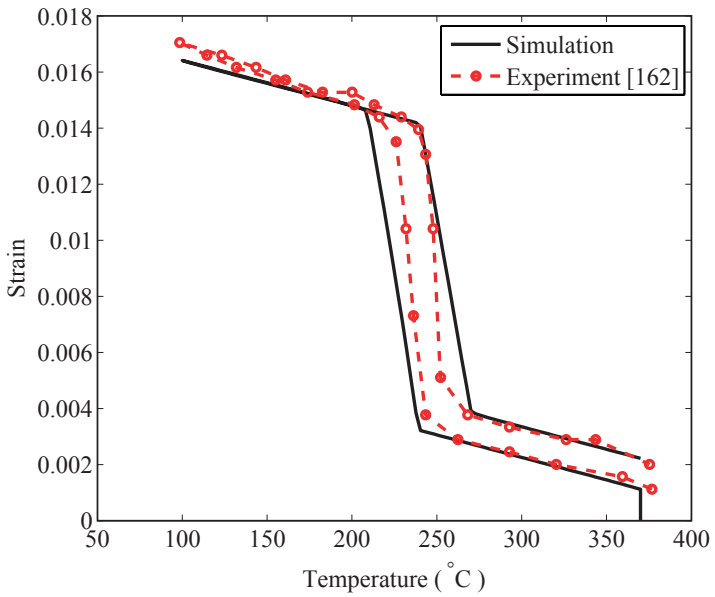

Figure 6.4: Comparison of 3D simulation and experiments for strain-temperature behavior of the $Ti_{50}Pd_{30}Ni_{20}$ specimen thermally cycled at 50 MPa applied stress.

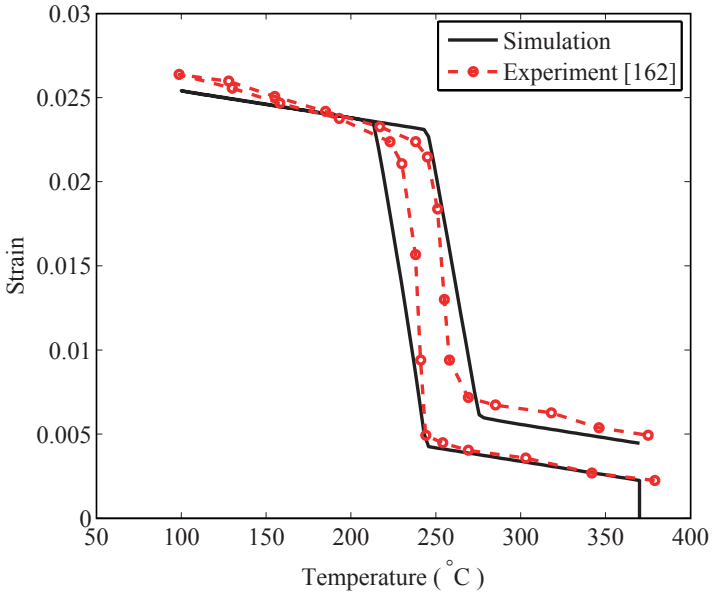

Figure 6.5: Comparison of 3D simulation and experiments for strain-temperature behavior of the $Ti_{50}Pd_{30}Ni_{20}$ specimen thermally cycled at 100 MPa applied stress.

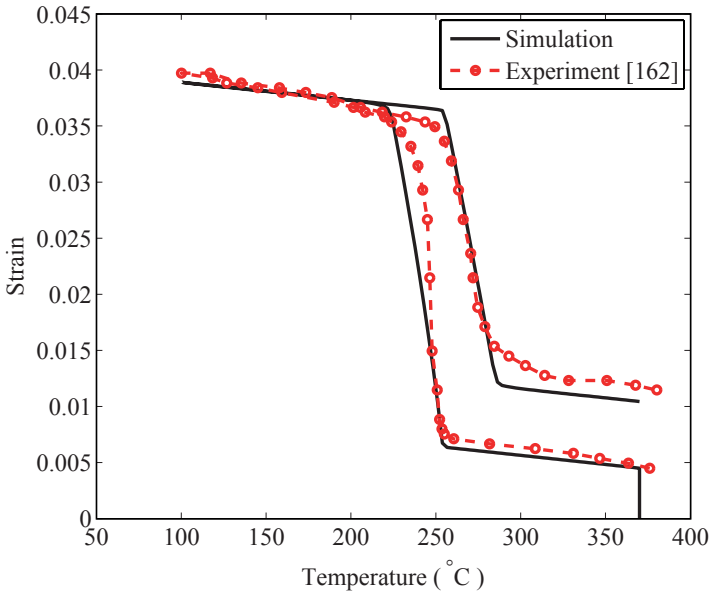

Figure 6.6: Comparison of 3D simulation and experiments for strain-temperature behavior of the $Ti_{50}Pd_{30}Ni_{20}$ specimen thermally cycled at 200 MPa applied stress.

As seen in Figures 6.4 to 6.8, the three dimensional isotropic based constitutive equations can predict the actuator behavior of $Ti_{50}Pd_{30}Ni_{20}$. It

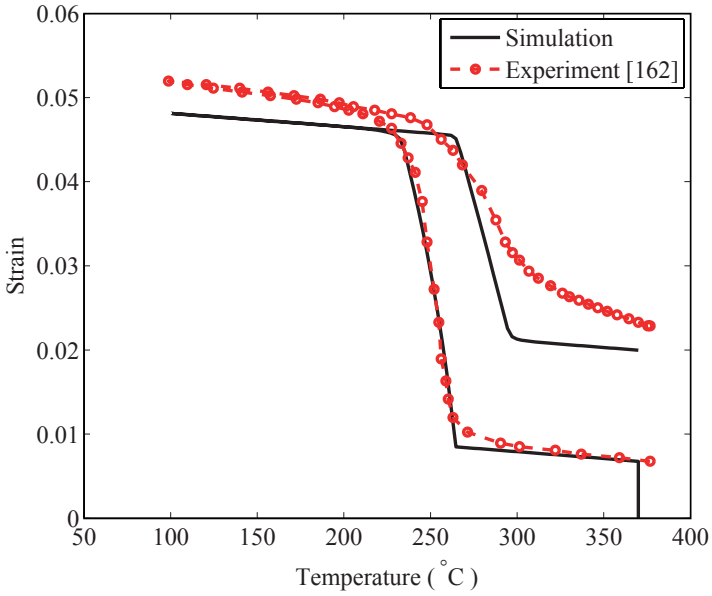

Figure 6.7: Comparison of 3D simulation and experiments for strain-temperature behavior of the $Ti_{50}Pd_{30}Ni_{20}$ specimen thermally cycled at 300 MPa applied stress.

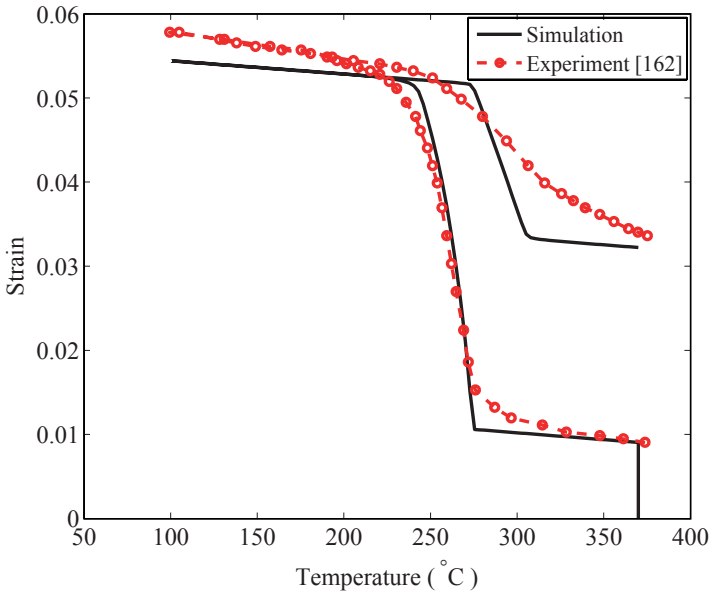

Figure 6.8: Comparison of 3D simulation and experiments for strain-temperature behavior of the $Ti_{50}Pd_{30}Ni_{20}$ specimen thermally cycled at 400 MPa applied stress.

is shown in Figure 6.4 that the transformation induced plasticity is an active deformation mechanism when the applied stress is small. It is because the

local stress due to the martensitic transformation is much higher than the external stresses.

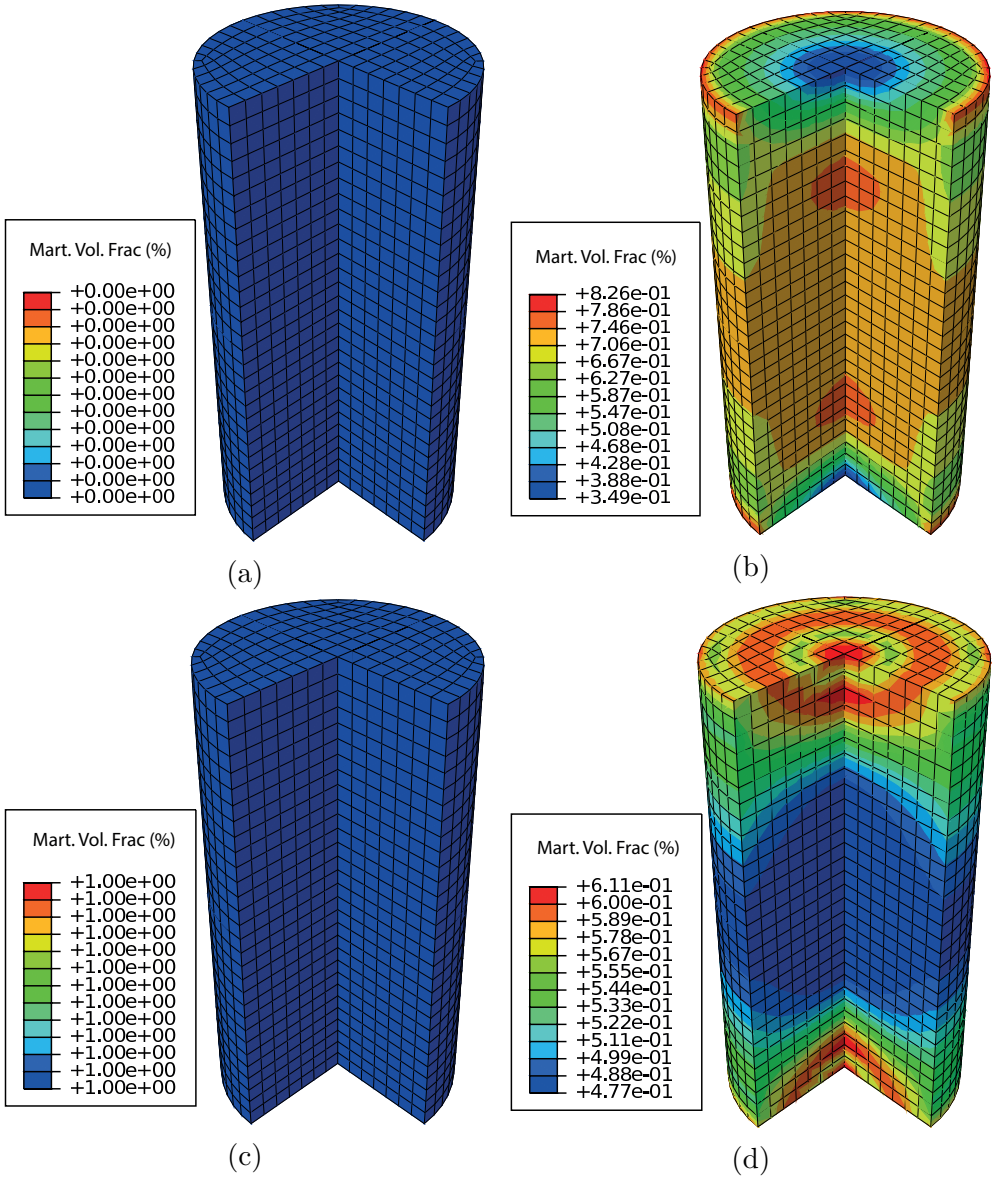

Figure 6.9: The evolution of martensitic volume fraction during forward and backward transformation: (a) $\theta = 370°C$, forward transformation, (b) $\theta = 232°C$, forward transformation, (c) $\theta = 100°C$, backward transformation, and (d) $\theta = 270°C$, backward transformation.

The distribution of martensitic volume fraction and Mises stress during forward and backward transformation for the sample under thermal cycling

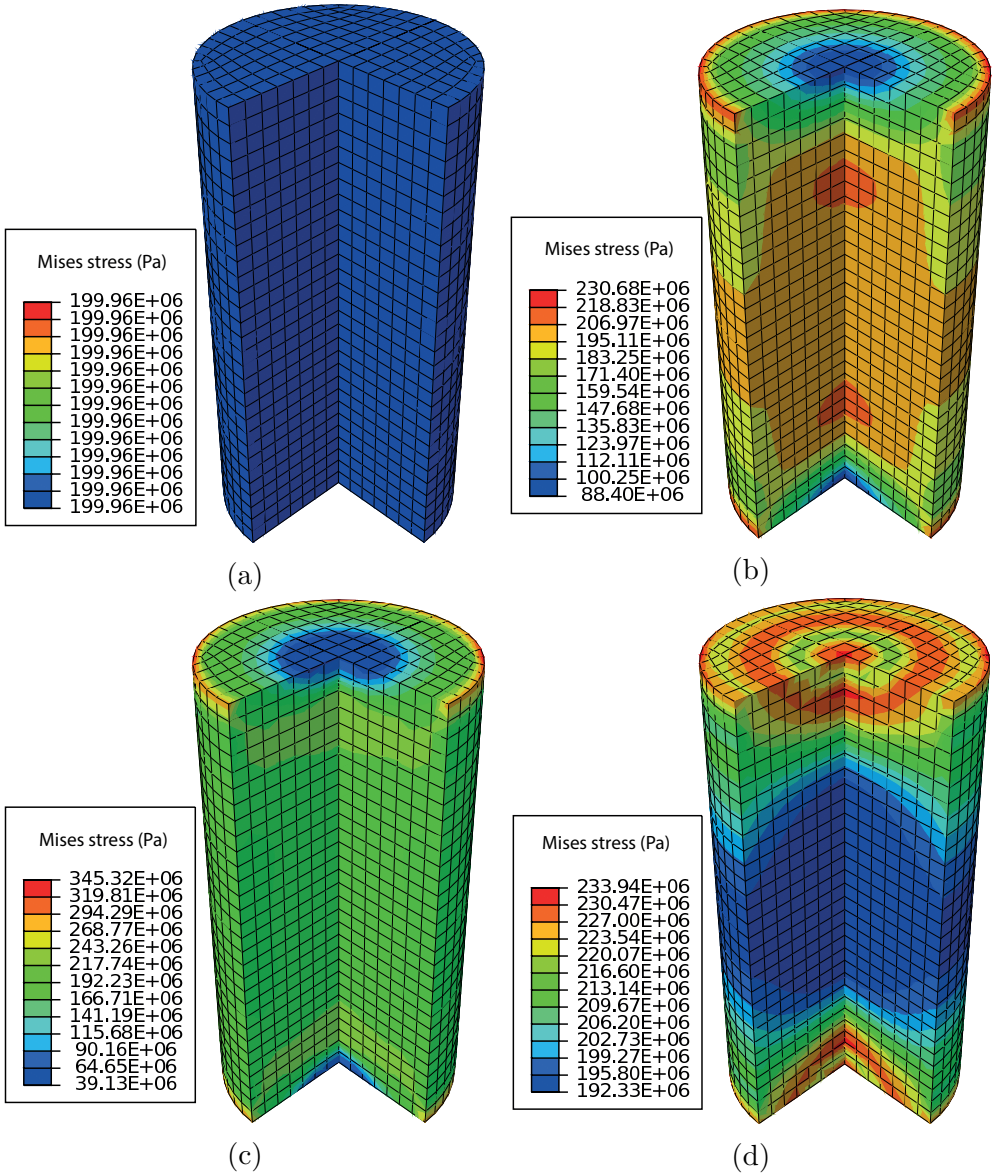

Figure 6.10: The distribution of mises stress during forward and backward transformation: (a) $\theta = 370°C$, forward transformation, (b) $\theta = 232°C$, forward transformation, (c) $\theta = 100°C$, backward transformation, and (d) $\theta = 270°C$, backward transformation.

and 200 MPa compression stress are presented in Figures 6.9 and 6.10, respectively. It is illustrated in the these figures that the distribution of stress and the martensitic volume fraction are not homogeneous. This heterogeneity is created by the friction contact between cylinder and rigid

grips.

6.3.2 Example 2: Actuation response of a spring

One of the main applications of high temperature shape memory alloys is actuation behavior. In this section the response of a helical spring that is made from $Ti_{50}Pd_{30}Ni_{20}$ that is applied in thermally induced actuators is investigated. In this model, the coil diameter is 12.7 mm and the wire diameter is 0.5 mm with spring pitch of 2.8 mm. The three-dimensional C3D8T which is suitable for coupled temperature-displacement situation is applied to solve the problem. The single coil spring is modeled while the environment temperature is changing between 200°C and 320°C with the rate of $5°C/min$ and the spring is under 0.25 N axial force when the other end is fixed. The model is presented in Figure 6.11 and the displacement-temperature response of the spring is presented in Figure 6.12.

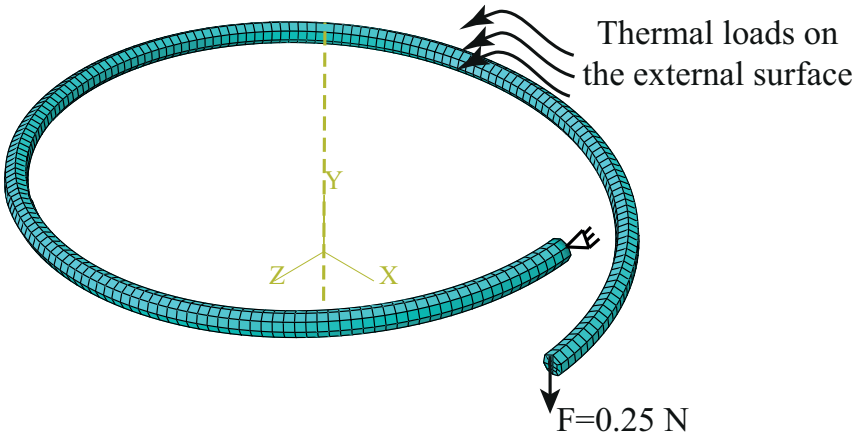

Figure 6.11: 3D view of an one coil spring of the $Ti_{50}Pd_{30}Ni_{20}$ specimen thermally cycled with temperature rate of $5°C/min$.

As can be seen in Figure 6.12, when the spring heated back to the initial temperature, the material fully transformed back to austenite but the specimen still shows the irrecoverable strain. The recoverable response of the actuator is affected by the irrecoverable viscoplastic and transformation induced plasticity (TRIP).

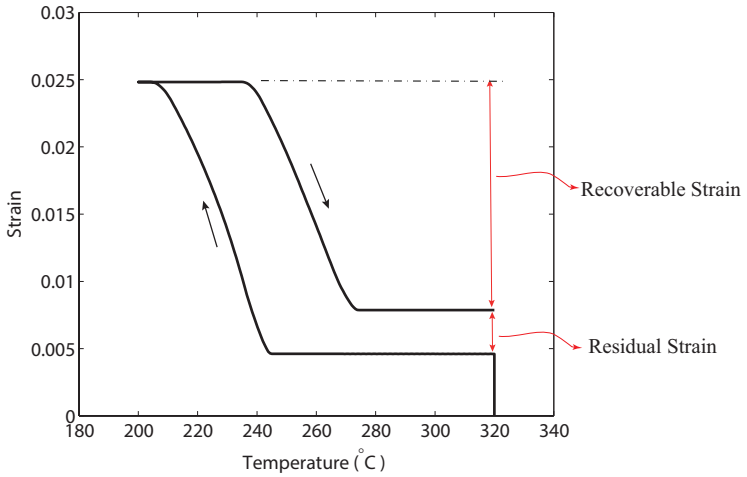

Figure 6.12: Displacement-Temperature behavior of the $Ti_{50}Pd_{30}Ni_{20}$ spring, thermally cycled with temperature rate of $5°C/min$.

6.4 Linking the micro-scale simulations with macro-scale modeling

As mentioned at the beginning of this chapter, although the discrete dislocation-transformation framework (presented in Chapters 3-5) and isotropic based constitutive model (presented in this chapter) are not linked together quantitatively, there are some relations between the results of the micro-scale simulations and the suggested phenomenological equations in the macro-

scale model. To relate these two models, some comparisons between results calculated by both methods under certain assumptions, are performed in this section.

The predicted strain-temperature responses of NiTi under thermal cycling and a 300 MPa constant applied stress by both methods are compared here. The following considerations are made to compare results from the two models: (i) The material behavior of NiTi is applied in the continuum model expect for maximum transformation strain that is scaled by a factor of 0.1 so that it is the same as discrete dislocation-transformation model. (ii) According to the discrete dislocation-transformation model, the NiTi transforms to a maximum 25% of martensitic phase with this method. Therefore, this limit is applied to the macroscopic model. (iii) As the important terms in our study are plasticity and transformation strains, the thermal expansion strain is subtracted from both simulations. (iv) The heating and cooling rate is assumed to be high enough to avoid any viscoplasticity in austenite phase, but it is not as high as the temperature rate in discrete dislocation-transformation model.

The comparison between strain-temperature results of the discrete dislocation-transformation method and isotropic continuum model is presented in Figure 6.13. As can be seen in this figure, by applying the above assumptions, the results show a similar trend with comparable values. However, there are some phenomenological equations and fitting parameters in the con-

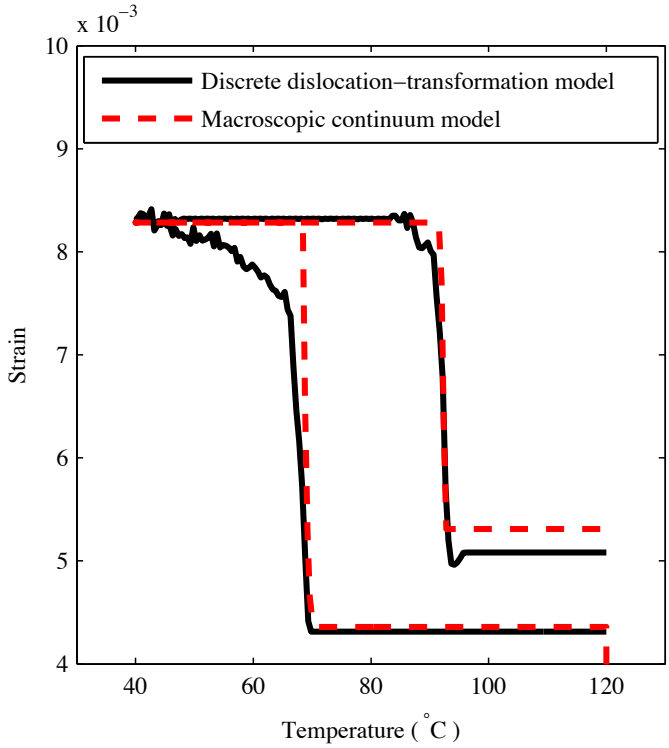

Figure 6.13: The comparison of predicted strain-temperature response by discrete dislocation-transformation framework and continuum model for NiTi under thermal cycling and 300 MPa applied stress.

tinuum model which describe the physical phenomena in microstructure. One of these phenomena is transformation-induced plasticity which is a result of interaction between martensitic transformation and dislocation slip. This phenomena is modeled by a suggested phenomenological model (equations (6.49) and (6.50)) and material parameter "a". The effect of changing "a" factor on the results is illustrated in Figure 6.14. As can be seen in this figure, the "a" factor is a material parameter that has direct effect on transformation-induced plastic(TRIP) strain. Therefore, it can be concluded, that the dislocation-transformation interaction and TRIP strain are linked together qualitatively. Furthermore, although the multi-

scale simulation is not the aim of this study, it can be suggested as a future work to calculate "a" parameter or update the phenomenological equation from the discrete dislocation-transformation method and then used in the continuum model.

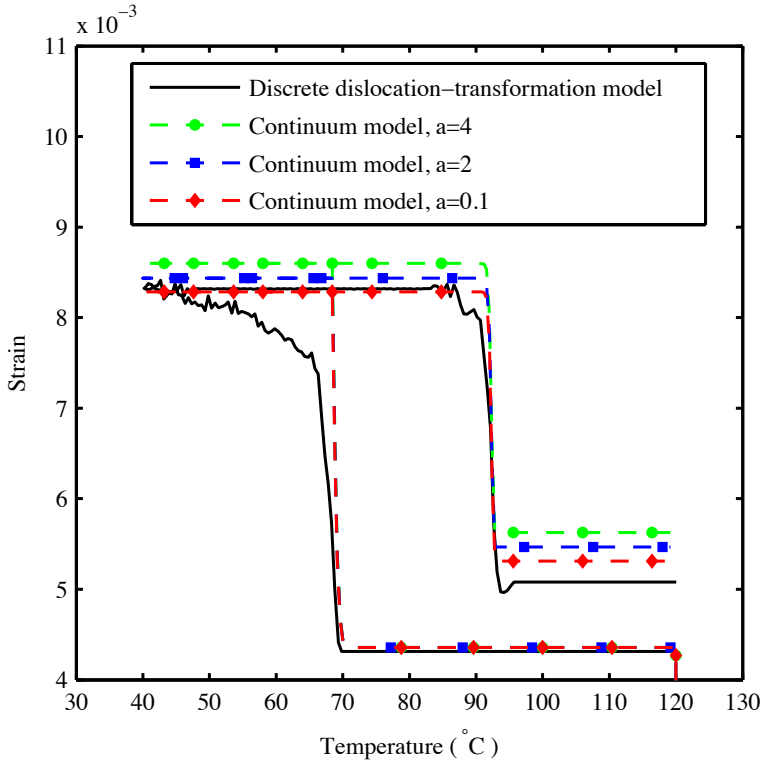

Figure 6.14: The comparison of predicted strain-temperature response by discrete dislocation-transformation framework and continuum model for NiTi and effect of material parameter "a" on the results.

The other physical phenomena which is illustrated in Figure 6.15 is the resistance of grain boundaries and dislocation arrays on the transformation growth. This phenomena is also modeled with the material parameter "h" in the continuum model (equation (6.37)) to fit the slope of the martensitic transformation. Again, it can be suggested to compute the "h" factor based on to the results from the discrete dislocation-transformation simulations

of polycrystalline NiTi as a multi-scale model in future.

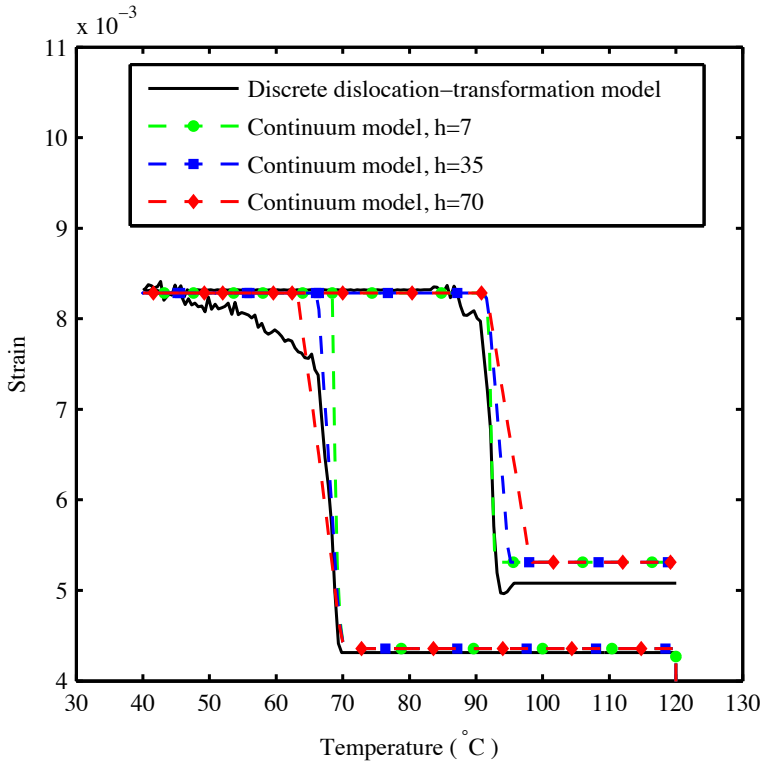

Figure 6.15: The comparison of predicted strain-temperature response by discrete dislocation-transformation framework and continuum model for NiTi and effect of material parameter "h" on the results.

6.5 Conclusions

In this chapter, an isotropic-plasticity-based constitutive equation is presented for investigation of the coexistence between plasticity and martensitic transformation in high temperature shape memory alloys. Then, the three-dimensional constitutive equations are implemented in a commercial FEM software (ABAQUS) by writing an explicit user subroutine to model the mechanical behavior of $Ti_{50}Pd_{30}Ni_{20}$. Some coupled displacement-

temperature simulations under thermal cycling and constant compression stresses are designed. To verify the predicted theoretical results, they are compared with physical experiments data from [162, 169].

The comparison of results with experimental data firstly shows us the validity of the presented constitutive equation for SMAs after calculating the material constant. Therefore, this model can be used to predict the thermo-mechanical behavior of SMAs such as $Ti_{50}Pd_{30}Ni_{20}$. It also can be applied to study and design of the macro-scale engineering application. Furthermore, it is concluded that, for shape memory alloys in high temperatures, the phase transformation occurs in the temperatures that the creep mechanisms and transformation induced plasticity (TRIP) have been activated. Therefore some irrecoverable strains occur during phase transformation and also during plasticity in austenite that affects on the actuation behavior of the thermally induced actuators that are made from these materials.

Finally, the comparison between strain-temperature results of the discrete dislocation-transformation method and isotropic continuum model under special assumptions shows the qualitative link between two methods. It is also shown how some of the fitting parameters in continuum model represent physical phenomena in microstructure of SMA. However, the multi-scale modeling of the material is out of the scope of this study and the two methods are not linked together quantitatively.

Chapter 7

Conclusions and future work

In this thesis, the interaction between dislocation slip plasticity and martensitic phase transformation has been investigated. This interaction includes the effects of martensitic transformation on dislocation plasticity (called transformation-induced plasticity) and effects of dislocations on the generation and growth of martensitic regions. These phenomena were modeled by discrete dislocation-transformation method in microstructure and the continuum model in macro-scale. The results have shown that the plastic strain due to the dislocation slip mechanism affects the reversibility of shape memory alloys during thermal or mechanical cycles that influences the actuation behavior of SMAs. Furthermore, the results have better explanatory power for illustrating the important factors that influence the two-way shape memory effect and pseudo-elasticity behaviors. The results also provide new perspective to modify the behavior of shape memory alloys

for thermal actuation application.

In Chapter 3, the discrete dislocation-transformation method was presented for the shape memory alloys. This model is capable of simulating the two-way martensitic transformation under mechanical and thermal loading. Therefore, this method can be used for modeling the cyclic behavior of SMAs. Although the presented discrete dislocation-transformation framework is restricted to two-dimensional models, it gives an acceptable estimation of total behavior of the material due to the nature of slip and transformation systems. The validity of two-dimensional discrete dislocation-transformation model for simulating the dislocation slips and phase transformation mechanisms are discussed further in [35, 96].

In Chapter 4, a two-dimensional single crystal region of NiTi shape memory alloy was modeled by the discrete dislocation-transformation method. The specimen was loaded under cyclic mechanical and thermal loading. The results indicated the effect of dislocation slip on total cyclic behavior of SMAs as well as the effects of dislocation on the generation and growth of transformation regions. Furthermore, the martensitic transformation influenced the local stresses and thus affected the dislocation nucleation and slip mechanisms. The results showed that the sample in the presence of dislocations transforms less in comparison to the one without dislocations and it means that the dislocations play the obstacle role against martensitic growth. However, when the specimen experiences multi-cycle loadings, the

remaining dislocations from one cycle helps the generation of martensitic regions in subsequent cycles. Therefore, dislocations play both resisting and assisting role for martensitic transformation depending on the loading states.

It was also shown that for thermal cyclic test under low applied tractions (lower than critical slip stress), the dislocation systems were activated at the beginning of transformations. These results provide a clear conclusion that the phase transformation in shape memory alloys changes the local stress in specimen, and it affects the dislocation slip mechanism. Moreover, the solid-solid phase boundaries between austenite and martensite phases play a role similar to grain boundaries and resist the dislocation motions.

In Chapter 5, a two dimensional multi-crystalline sample of NiTi shape memory alloy was simulated by the discrete dislocation-transformation framework which was used to model the single crystal material. The results illustrate the effect of different structural orientations on the thermo-mechanical response of the SMAs. It was explained that both dislocation slip and martensitic transformation are orientation dependent. Therefore, changing the orientation of one grain in a double-grain sample changes the mechanical response of the specimen during loading.

Furthermore, the effect of grain size and grain boundary densities on the two-way shape memory effect and super-elasticity were studied. The grain boundaries works as an obstacle against the dislocation motion and

martensitic growth. Therefore, the smaller grain specimens contain more dislocations and less martensitic volume fraction and as a result shows harder response. These results also confirms that our discrete dislocation-transformation framework has the ability to simulate the Hall-Petch effect in polycrystalline structures.

Due to computational limitations, the number of grains was limited to a maximum of sixteen grains. Although the real polycrystalline model have to include hundreds or thousands of grains, the current model is useful to investigate the orientation and grain boundary effects by looking directly at the dislocation dynamics and transformation in the microstructure.

In Chapter 6, the three-dimensional constitutive equations for modeling the interaction of plasticity and phase transformation in macro-scale are presented. The macroscopic simulations can be used to model the large scale of specimen and therefore it is useful to model the real industrial applications. Then, the results from the simulation of the $Ti_{50}Pd_{30}Ni_{20}$ systems were compared with the experimental results from the literature. The results and comparison validated the constitutive model for this kind of shape memory alloys. As the results illustrated, transformation-induced plasticity is an important mechanism that affects the reversibility of $Ti_{50}Pd_{30}Ni_{20}$ under thermal cyclic loading although the applied external stress is lower than yield stress of the material.

7.1 Suggestion for future works

Based on the studies and results described in this thesis, some further research projects can be suggested based on discrete dislocation-transformation method and application of this method for shape memory alloys.

- In this study, the two-dimensional formulation for discrete dislocation and transformation were considered. This assumption was because of the intrinsic behavior of dislocation dynamic and martensitic transformation which occurs in plane geometries. This framework can predict the behavior of SMAs correctly because the mechanism of dislocation slip and transformation occur in slip planes and habit planes respectively. However, developing the three-dimensional discrete dislocation-transformation framework is an interesting area for future research.

- It would also be interesting to develop a multi-scale modeling on SMAs by exporting some material parameters from the discrete dislocation-transformation model from the microstructure modeling and importing them to the three-dimensional continuum model. This may be helpful to have a complete framework to model the 3D macro-scale application by considering the important factors in microstructure.

- In this study, we have investigated the grain size effect in multi-crystalline samples. It includes the resistance of grain boundaries in

front of dislocation motions and martensitic growth. Recently, it has been shown experimentally that the size of single crystalline samples influences martensitic transformation as well as dislocation plasticity [170, 171]. Furthermore, the nature of our discrete dislocation-transformation method makes it a good tool to study this phenomenon in the microstructure. Therefore, one interesting future work may be the study of the sample size effect in single-crystalline shape memory alloys.

- As indicated, the dislocation dynamic mechanism is limited to dislocations slip in this study. However, other plasticity mechanism such as dislocation climb can be added to the current model. Therefore, the study the interaction between dislocation climb and martensitic transformation is a suggestion for future work. The result of these simulations will be useful for high temperature shape memory alloys where creep mechanism is affecting martensitic transformation.

Bibliography

[1] L.C. Chang and T.A. Read. Plastic Deformation and Diffusionless Phase Changes in Metals The Bold-Cadmium Beta Phase. *AIME Transactions*, page 6, 1951.

[2] J. Van Humbeeck. Non-medical applications of shape memory alloys. *Materials Science and Engineering: A*, 273-275:134–148, 1999.

[3] D.J. Hartl and D.C. Lagoudas. Aerospace applications of shape memory alloys. *Proceedings of the Institution of Mechanical Engineers, Part G: Journal of Aerospace Engineering*, 221(4):535–552, 2007.

[4] P.K. Kumar and D.C. Lagoudas. *Shape Memory Alloys*, volume 1. Springer US, Boston, MA, 2008.

[5] S Barbarino, E I Saavedra Flores, R M Ajaj, I Dayyani, and M I Friswell. A review on shape memory alloys with applications to morphing aircraft. *Smart Materials and Structures*, 23(6):063001, 2014.

[6] K. Otsuka and C.M. Wayman, editors. *Shape Memory Materials*. Cambridge University press, 1999.

[7] G.B. Olson and M. Cohen. Thermoelastic behavior in martensitic transformations. *Scripta Metallurgica*, 9(11):1247–1254, 1975.

[8] K. Gall. The role of texture in tension-compression asymmetry in polycrystalline NiTi. *International Journal of Plasticity*, 15(1):69–92, 1999.

[9] M.L. Bowers, X. Chen, M. De Graef, P.M. Anderson, and M.J. Mills. Characterization and modeling of defects generated in pseudoelastically deformed NiTi microcrystals. *Scripta Materialia*, 78-79:69–72, 2014.

[10] J. Wang and H. Sehitoglu. Modelling of martensite slip and twinning in NiTiHf shape memory alloys. *Philosophical Magazine*, 94(20):2297–2317, 2014.

[11] D.A. Miller and D.C. Lagoudas. Thermomechanical characterization of NiTiCu and NiTi SMA actuators: influence of plastic strains. *Smart Materials and Structures*, 9(5):640–652, 2000.

[12] D.A. Miller and D.C. Lagoudas. Influence of cold work and heat treatment on the shape memory effect and plastic strain development of NiTi. *Materials Science and Engineering: A*, 308(1-2):161–175, 2001.

[13] J. Ma, I. Karaman, B. Kockar, H.J. Maier, and Y.I. Chumlyakov. Severe plastic deformation of $Ti_{74}Nb_{26}$ shape memory alloys. *Materials Science and Engineering: A*, 528(25-26):7628–7635, 2011.

[14] R.F. Hamilton, H. Sehitoglu, Y. Chumlyakov, and H.J. Maier. Stress dependence of the hysteresis in single crystal NiTi alloys. *Acta Materialia*, 52(11):3383–3402, 2004.

[15] H. Scherngell and A.C. Kneissl. Training and stability of the intrinsic two-way shape memory effect in Ni-Ti alloys. *Scripta Materialia*, 39(2):205–212, 1998.

[16] C. Lexcellent and G. Bourbon. Thermodynamical model of cyclic behaviour of Ti-Ni and Cu-Zn-Al shape memory alloys under isothermal undulated tensile tests. *Mechanics of Materials*, 24(1):59–73, 1996.

[17] J. Dadda, H.J. Maier, D. Niklasch, I. Karaman, H.E. Karaca, and Y.I. Chumlyakov. Pseudoelasticity and Cyclic Stability in $Co_{49}Ni_{21}Ga_{30}$ Shape-Memory Alloy Single Crystals at Ambient Temperature. *Metallurgical and Materials Transactions A*, 39(9):2026–2039, 2008.

[18] O. Benafan, R.D. Noebe, S.a. Padula, D.W. Brown, S. Vogel, and R. Vaidyanathan. Thermomechanical cycling of a NiTi shape memory alloy-macroscopic response and microstructural evolution. *International Journal of Plasticity*, 56:99–118, 2014.

[19] M. Cherkaoui, M. Berveiller, and X. Lemoine. Couplings between plasticity and martensitic phase transformation: overall behavior of polycrystalline TRIP steels. *International Journal of Plasticity*, 16(10-11):1215–1241, 2000.

[20] F.D. Fischer, G. Reisner, E. Werner, K. Tanaka, G. Cailletaud, and T. Antretter. A new view on transformation induced plasticity (TRIP). *International Journal of Plasticity*, 16(7-8):723–748, 2000.

[21] Qian Zhou, Lihe Qian, Jun Tan, Jiangying Meng, and Fucheng Zhang. Inconsistent effects of mechanical stability of retained austenite on ductility and toughness of transformation-induced plasticity steels. *Materials Science and Engineering: A*, 578:370–376, 2013.

[22] Z. Bo and D.C. Lagoudas. Thermomechanical modeling of polycrystalline SMAs under cyclic loading, Part III: evolution of plastic strains and two-way shape memory effect. *International Journal of Engineering Science*, 37(9):1205–1249, 1999.

[23] P.B. Entchev and D.C. Lagoudas. Modeling of transformation-induced plasticity and its effect on the behavior of porous shape memory alloys. Part I: constitutive model for fully dense SMAs. *Mechanics of Materials*, 36(9):865–892, 2004.

[24] Hiroyuki Kato and Kazuaki Sasaki. Transformation-induced plasticity as the origin of serrated flow in an NiTi shape memory alloy. *International Journal of Plasticity*, 50:37–48, 2013.

[25] T. Fukuda, T. Saburi, K. Doi, and S. , Nenno. Nucleation and self-accommodation of the r-phase in Ti-Ni alloys. *Materials Transactions JIM*, 33(3):271–277, 1992.

[26] A. Ibarra, J. San Juan, E.H. Bocanegra, and M.L. Nó. Evolution of microstructure and thermomechanical properties during superelastic compression cycling in Cu-Al-Ni single crystals. *Acta Materialia*, 55(14):4789–4798, 2007.

[27] G.B. Olson and M. Cohen. A general mechanism of martensitic nucleation: Part I. General concepts and the FCC $\longrightarrow$ HCP transformation. *Metallurgical Transactions A*, 7(12):1897–1904, 1976.

[28] G.B. Olson and M. Cohen. A general mechanism of martensitic nucleation: Part II. FCC $\longrightarrow$ BCC and other martensitic transformations. *Metallurgical Transactions A*, 7(12):1905–1914, 1976.

[29] J.G. Boyd and D.C. Lagoudas. A thermodynamical constitutive model for shape memory materials. Part I. The monolithic shape memory alloy. *International Journal of Plasticity*, 12(6):805–842, 1996.

[30] P. Thamburaja. Constitutive equations for martensitic reorientation and detwinning in shape-memory alloys. *Journal of the Mechanics and Physics of Solids*, 53(4):825–856, 2005.

[31] O. Kastner. Molecular-dynamics of a 2D model of the shape memory effect. *Continuum Mechanics and Thermodynamics*, 15(5):487–502, 2003.

[32] O. Kastner, G. Eggeler, W. Weiss, and G.J. Ackland. Molecular dynamics simulation study of microstructure evolution during cyclic martensitic transformations. *Journal of the Mechanics and Physics of Solids*, 59(9):1888–1908, 2011.

[33] R. Amodeo and N. Ghoniem. Dislocation dynamics. I. A proposed methodology for deformation micromechanics. *Physical Review B*, 41(10):6958–6967, 1990.

[34] E. Van der Giessen and A. Needleman. Discrete dislocation plasticity: a simple planar model. *Modelling and Simulation in Materials Science and Engineering*, 3(5):689–735, 1995.

[35] J. Shi, S. Turteltaub, E. Van der Giessen, and J.J.C. Remmers. A discrete dislocation-transformation model for austenitic single crystals. *Modelling and Simulation in Materials Science and Engineering*, 16(5):055005, 2008.

[36] W.J. Buehler, J.V. Gilfrich, and R.C. Wiley. Effect of Low-Temperature Phase Changes on the Mechanical Properties of Alloys near Composition TiNi. *Journal of Applied Physics*, 34(5):1475, 1963.

[37] W.J. Buehler and F.E. Wang. A summary of recent research on the nitinol alloys and their potential application in ocean engineering. *Ocean Engineering*, 1(1):105–120, 1968.

[38] L. Petrini and F. Migliavacca. Biomedical Applications of Shape Memory Alloys. *Journal of Metallurgy*, 2011(Figure 1):1–15, 2011.

[39] L.C. Zhao, T.W. Duerig, S. Justi, K.N. Melton, J.L. Proft, W. Yu, and C.M. Wayman. The Study of Niobium-Rich Precipitates in a Ni-Ti-Nb Shape Memory Alloy. *Scripta Metallurgica Et Materialia*, 24(2):221–226, 1990.

[40] C. a. Biffi, a. Nespoli, B. Previtali, E. Villa, and a. Tuissi. Functional Response of NiTi Elements for Smart Micro-actuation Applications. *Journal of Materials Engineering and Performance*, 23(7):2351–2356, 2014.

[41] Antonio Isalgue, Carlota Auguet, Guillem Carreras, and Vicenç Torra. Sma (Cu-Based, Niti) For Use In Damping: The Implications Of Reliability For Long Time Applications And Aging Behavior. *Functional Materials Letters*, 05(01):1250008, 2012.

[42] D.E. Hodgson, M.H. Wu, and R.J. Biermann. Shape memory alloys. *Metals Handbook*, 2:897–902, 1990.

[43] D.R. Angst, P.E. Thoma, and M.Y. Kao. The effect of hafnium content on the transformation temperatures of $Ni_{49}Ti_{51-x}Hf_x$ shape memory alloys. *Journal de Pysique IV*, 5(C8, 2):747–752, 1995.

[44] O. Rios, R. Noebe, T. Biles, A. Garg, A. Palczer, D. Scheiman, H.J. Seifert, and M. Kaufman. Characterization of ternary NiTiPt high-temperature shape memory alloys. *Active Materials: Behavior and Mechanics*, 5761:376–387, 2005. Smart Structures and Materials 2005 Conference, San Diego, CA, MAR 07-10, 2005.

[45] G.S. Firstov, J. Van Humbeeck, and Y.N. Koval. Comparison of high temperature shape memory behaviour for ZrCu-based, Ti-Ni-Zr and Ti-Ni-Hf alloys. *Scripta Materialia*, 50(2):243–248, 2004.

[46] Z. Pu, H. Tseng, and K. Wu. Martensite Transformation and Shape Memory Effect of Niti-Zr High Temperature Shape Memory Alloys. *Smart Materials*, 2441:171–178, 1995.

[47] H.E. Karaca, S.M. Saghaian, G. Ded, H. Tobe, B. Basaran, H.J. Maier, R.D. Noebe, and Y.I. Chumlyakov. Effects of nanoprecipitation on the shape memory and material properties of an Ni-rich NiTiHf high temperature shape memory alloy. *Acta Materialia*, 61(19):7422–7431, 2013.

[48] Patrick J. McCluskey, Kechao Xiao, John M. Gregoire, Darren Dale, and Joost J. Vlassak. Application of in-situ nano-scanning calorimetry and X-ray diffraction to characterize Ni–Ti–Hf high-temperature shape memory alloys. *Thermochimica Acta*, 2014.

[49] K.C. Atli, I. Karaman, R.D. Noebe, and D. Gaydosh. The effect of training on two-way shape memory effect of binary NiTi and NiTi based ternary high temperature shape memory alloys. *Materials Science and Engineering: A*, 560:653–666, 2013.

[50] J. Mohd Jani, M. Leary, A. Subic, and M.A. Gibson. A review of shape memory alloy research, applications and opportunities. *Materials & Design*, 56:1078–1113, 2014.

[51] I. Karaman, B. Basaran, H. E. Karaca, a. I. Karsilayan, and Y. I. Chumlyakov. Energy harvesting using martensite variant reorientation mechanism in a NiMnGa magnetic shape memory alloy. *Applied Physics Letters*, 90(17):172505, 2007.

[52] Baris Emre, Süheyla Yüce, Enric Stern-Taulats, Antoni Planes, Simone Fabbrici, Franca Albertini, and Lluìs Mañosa. Large reversible entropy change at the inverse magnetocaloric effect in Ni-Co-Mn-Ga-In magnetic shape memory alloys. *Journal of Applied Physics*, 113(21):213905, 2013.

[53] Xiao Xu, Makoto Nagasako, Wataru Ito, Rie Y. Umetsu, Takeshi Kanomata, and Ryosuke Kainuma. Magnetic properties and phase

diagram of Ni50Mn50âĹŠxGax ferromagnetic shape memory alloys. *Acta Materialia*, 61(18):6712–6723, 2013.

[54] S. Miyazaki, K. Otsuka, and Y. Suzuki. Transformation pseudoelasticity and deformation behavior in a Ti-50.6at%Ni alloy. *Scripta Metallurgica*, 15(3):287–292, 1981.

[55] I. Mihálcz. Fundamental characteristics and design method for nickel-titanium shape memory alloy. *Periodica Pol Ytechnica Ser. Mech. Eng.*, 45(1):75–86, 2001.

[56] L. Torrisi. The NiTi superelastic alloy application to the dentistry field. *Bio-Medical Materials and Engineering*, 9(1):39–47, 1999.

[57] S.A. Thompson. An overview of nickel-titanium alloys used in dentistry. *International Endodontic Journal*, 33(4):297–310, 2000.

[58] D. Mantovani. Shape memory alloys: Properties and biomedical applications. *JOM*, 52(10):36–44, 2000.

[59] N.B. Morgan. Medical shape memory alloy applications–the market and its products. *Materials Science and Engineering: A*, 378(1-2):16–23, 2004.

[60] J. Ryhänen, M. Kallioinen, J. Tuukkanen, J. Junila, E. Niemelä, P. Sandvik, and W. Serlo. In vivo biocompatibility evaluation of nickel-titanium shape memory metal alloy: muscle and perineural tissue responses and encapsule membrane thickness. *Journal of Biomedical Materials Research*, 41(3):481–8, 1998.

[61] T.W. Duerig, A. Pelton, and D. Stöckel. An overview of nitinol medical applications. *Materials Science and Engineering: A*, 273-275:149–160, 1999.

[62] D. Stoeckel. Shape memory actuators for automotive applications. *Materials & Design*, 11(6):302–307, 1990.

[63] A. Bellini, M. Colli, and E. Dragoni. Mechatronic Design of a Shape Memory Alloy Actuator for Automotive Tumble Flaps: A Case Study. *IEEE Transactions on Industrial Electronics*, 56(7):2644–2656, 2009.

[64] E.A. Williams, G. Shaw, and M. Elahinia. Control of an automotive shape memory alloy mirror actuator. *Mechatronics*, 20(5):527–534, 2010.

[65] S. Padula II, G. Bigelow, R. Noebe, D. Gaydosh, and A. Garg. Challenges and progress in the development of high-temperature shape memory alloys based on NiTiX compositions for high-force actuator applications. In *SMST 2006: Proceedings of The International Conference On Shape Memory And Superelastic Technologies*. ASM INTERNATIONAL, 2006. International Conference on Shape Memory and Superelastic Technologies, Pacific Grove, CA, MAY 07-11, 2006.

[66] O.J. Godard, M.Z. Lagoudas, and D.C. Lagoudas. Design of Space Systems Using Shape Memory Alloys. *Smart Structures and Integrated Systems*, 5056:545–558, 2003.

[67] K. Singh and I. Chopra. Design of an Improved Shape Memory Alloy Actuator for Rotor Blade Tracking. *Smart Structures and Integrated Systems*, 4701:244–266, 2002.

[68] A.Y.N. Sofla, S.A. Meguid, K.T. Tan, and W.K. Yeo. Shape morphing of aircraft wing: Status and challenges. *Materials & Design*, 31(3):1284–1292, 2010.

[69] Y. Furuya and H. Shimada. Shape memory actuators for robotic applications. *Materials & Design*, 12(1):21–28, 1991.

[70] M. Sreekumar, T. Nagarajan, M. Singaperumal, M. Zoppi, and R. Molfino. Critical review of current trends in shape memory alloy actuators for intelligent robots. *Industrial Robot: An International Journal*, 34(4):285–294, 2007.

[71] L. Janke. Applications of shape memory alloys in civil engineering structures - Overview, limits and new ideas. *Materials and Structures*, 38(279):578–592, 2005.

[72] G. Song, N. Ma, and H.-N. Li. Applications of shape memory alloys in civil structures. *Engineering Structures*, 28(9):1266–1274, 2006.

[73] J. Gore, A. Bowles, M. Maylin, L. Chandrasekaran, D. Forsyth, and M. Buyers. High temperature shape memory alloy actuators through mechanical treatments for an oil & gas down-hole valve. *Industrial and Commercial Applications of Smart Structures Technologies*, 6930:69300R–69300R–11, 2008.

[74] S. Miyazaki, Y. Igo, and K. Otsuka. Effect of thermal cycling on the transformation temperatures of Ti-Ni alloys. *Acta Metallurgica*, 34(10):2045–2051, 1986.

[75] H. Sehitoglu, J. Jun, X. Zhang, I. Karaman, Y. Chumlyakov, H.J. Maier, and K. Gall. Shape memory and pseudoelastic behavior of 51.5%Ni-Ti single crystals in solutionized and overaged state. *Acta Materialia*, 49(17):3609–3620, 2001.

[76] K. Gall, M.L. Dunn, Y. Liu, P. Labossiere, H. Sehitoglu, and Y.I. Chumlyakov. Micro and Macro Deformation of Single Crystal NiTi. *Journal of Engineering Materials and Technology*, 124(2):238, 2002.

[77] Y. Nakata, T. Tadaki, and K. Shimizu. Thermal Cycling Effects in a Cu-A-Ni Shape Memory Alloy. *Transactions of the Japan Institute of Metals*, 26(9):646–652, 1985.

[78] A.R. Pelton, G.H. Huang, P. Moine, and R. Sinclair. Effects of thermal cycling on microstructure and properties in Nitinol. *Materials Science and Engineering: A*, 532:130–138, 2012.

[79] T. Simon, A. Kröger, C. Somsen, A. Dlouhy, and G. Eggeler. On the multiplication of dislocations during martensitic transformations in NiTi shape memory alloys. *Acta Materialia*, 58(5):1850–1860, 2010.

[80] J.A. Shaw and S. Kyriakides. Thermomechanical aspects of NiTi. *Journal of the Mechanics and Physics of Solids*, 43(8):1243–1281, 1995.

[81] B. Strnadel, S. Ohashi, H. Ohtsuka, S. Miyazaki, and T. Ishihara. Effect of mechanical cycling on the pseudoelasticity characteristics of Ti-Ni and Ti-Ni-Cu alloys. *Materials Science and Engineering: A*, 203(1-2):187–196, 1995.

[82] D.M. Norfleet, P.M. Sarosi, S. Manchiraju, M.F.-X. Wagner, M.D. Uchic, P.M. Anderson, and M.J. Mills. Transformation-induced plasticity during pseudoelastic deformation in Ni-Ti microcrystals. *Acta Materialia*, 57(12):3549–3561, 2009.

[83] K. Gall and H.J. Maier. Cyclic deformation mechanisms in precipitated NiTi shape memory alloys. *Acta Materialia*, 50(18):4643–4657, 2002.

[84] R. Delville, B. Malard, J. Pilch, P. Sittner, and D. Schryvers. Transmission electron microscopy investigation of dislocation slip during superelastic cycling of Ni-Ti wires. *International Journal of Plasticity*, 27(2):282–297, 2011.

[85] B. Kockar, I. Karaman, J.I. Kim, Y.I. Chumlyakov, J. Sharp, and C.J. (Mike) Yu. Thermomechanical cyclic response of an ultrafine-grained NiTi shape memory alloy. *Acta Materialia*, 56(14):3630–3646, 2008.

[86] B. Malard, J. Pilch, P. Sittner, V. Gartnerova, R. Delville, D. Schryvers, and C. Curfs. Microstructure and functional property changes in thin Ni-Ti wires heat treated by electric current – high energy x-ray and tem investigations. *Functional Materials Letters*, 02(02):45–54, 2009.

[87] J. Perkins. Lattice transformations related to unique mechanical effects. *Metallurgical Transactions*, 4(12):2709–2721, 1973.

[88] S. Kajiwara and T. Kikuchi. Dislocation structures produced by reverse martensitic transformation in a Cu-Zn alloy. *Acta Metallurgica*, 30(2):589–598, 1982.

[89] G. Ghosh. Effect of pre-strain on the kinetics of isothermal martensitic transformation. *Philosophical Magazine A*, 71(2):333–345, 1995.

[90] H. Morawiec, D. Stróz, T. Goryczka, and D. Chrobak. Two-stage martensitic transformation in a deformed and annealed NiTi alloy. *Scripta Materialia*, 35(4):485–490, 1996.

[91] J.P. Hirth and J. Lothe. *Theory of Dislocations*. Wiley, New York, 1982.

[92] F.R.N. Nabarro. *Theory of crystal dislocations*. Oxford University Press, Oxford, 1967.

[93] V.V. Bulatov, M. Tang, and H.M. Zbib. Crystal Plasticity from Dislocation Dynamics. *MRS Bulletin*, 26(March):191–195, 2001.

[94] S. Olarnrithinun, S.S. Chakravarthy, and W.a. Curtin. Discrete dislocation modeling of fracture in plastically anisotropic metals. *Journal of the Mechanics and Physics of Solids*, 61(6):1391–1406, 2013.

[95] Siamak Soleymani Shishvan and Erik Van Der Giessen. Mode I crack analysis in single crystals with anisotropic discrete dislocation plasticity: I. Formulation and crack growth. *Modelling and Simulation in Materials Science and Engineering*, 21(6):065006, 2013.

[96] A.A. Benzerga, Y. Bréchet, A. Needleman, and E. Van Der Giessen. Incorporating three-dimensional mechanisms into two-dimensional dislocation dynamics. *Modelling and Simulation in Materials Science and Engineering*, 12(1):159–196, 2004.

[97] A. Needleman, E. Van der Giessen, and V.S. Deshpande. Statistical aspects of discrete dislocation plasticity. *Scripta Materialia*, 54(5):729–733, 2006.

[98] H.M. Zbib, M. Hiratani, and M. Shehade. *Multiscale discrete dislocation dynamics plasticity*, chapter Book Chapter 9 of Continuum Scale Simulation of Engineering Materials. Wiley-VCH, 2003.

[99] Minsheng Huang, Liguo Zhao, and Jie Tong. Discrete dislocation dynamics modelling of mechanical deformation of nickel-based single crystal superalloys. *International Journal of Plasticity*, 28(1):141–158, 2012.

[100] Minsheng Huang and Zhenhuan Li. The key role of dislocation dissociation in the plastic behaviour of single crystal nickel-based superalloy with low stacking fault energy: Three-dimensional discrete dislocation dynamics modelling. *Journal of the Mechanics and Physics of Solids*, 61(12):2454–2472, 2013.

[101] G.V. Prasad Reddy, C. Robertson, C. Déprés, and M. Fivel. Effect of grain disorientation on early fatigue crack propagation in face-centred-cubic polycrystals: A three-dimensional dislocation dynamics investigation. *Acta Materialia*, 61(14):5300–5310, 2013.

[102] Kamyar M. Davoudi, Lucia Nicola, and Joost J. Vlassak. Dislocation climb in two-dimensional discrete dislocation dynamics. *Journal of Applied Physics*, 111(10):103522, 2012.

[103] K Danas and V S Deshpande. Plane-strain discrete dislocation plasticity with climb-assisted glide motion of dislocations. *Modelling and Simulation in Materials Science and Engineering*, 21(4):045008, 2013.

[104] Siu Sin Quek, Zhaoxuan Wu, Yong Wei Zhang, and David J. Srolovitz. Polycrystal deformation in a discrete dislocation dynamics framework. *Acta Materialia*, 75:92–105, 2014.

[105] T. Ezaz, J. Wang, H. Sehitoglu, and H.J. Maier. Plastic deformation of NiTi shape memory alloys. *Acta Materialia*, 61(1):67–78, 2013.

[106] J. Shi, S. Turteltaub, and E. Van der Giessen. Analysis of grain size effects on transformation-induced plasticity based on a discrete dislocation-transformation model. *Journal of the Mechanics and Physics of Solids*, 58(11):1863–1878, 2010.

[107] J. Kundin, D. Raabe, and H. Emmerich. A phase-field model for incoherent martensitic transformations including plastic accommodation processes in the austenite. *Journal of the Mechanics and Physics of Solids*, 59(10):2082–2102, 2011.

[108] Julia Kundin, Heike Emmerich, and Johannes Zimmer. Mathematical concepts for the micromechanical modelling of dislocation dynamics

with a phase-field approach. *Philosophical Magazine*, 91(1):97–121, 2011.

[109] R. Abeyaratne and S.J. Kim. Cyclic effects in shape-memory alloys: a one-dimensional continuum model. *International Journal of Solids and Structures*, 34(25):3273–3289, 1997.

[110] J.G. Boyd and D.C. Lagoudas. A thermodynamical constitutive model for shape memory materials. Part I. The monolithic shape memory alloy. *International Journal of Plasticity*, 12(6):805–842, 1996.

[111] X. Gao, M. Huang, and L.C. Brinson. A multivariant micromechanical model for SMAs Part 1. Crystallographic issues for single crystal model. *International Journal of Plasticity*, 16(10-11):1345–1369, 2000.

[112] M. Panico and L.C. Brinson. A three-dimensional phenomenological model for martensite reorientation in shape memory alloys. *Journal of the Mechanics and Physics of Solids*, 55(11):2491–2511, 2007.

[113] L. Anand and M.E. Gurtin. Thermal effects in the superelasticity of crystalline shape-memory materials. *Journal of the Mechanics and Physics of Solids*, 51(6):1015–1058, 2003.

[114] F. Auricchio, E. Bonetti, G. Scalet, and F. Ubertini. Theoretical and numerical modeling of shape memory alloys accounting for multiple phase transformations and martensite reorientation. *International Journal of Plasticity*, 59:30–54, 2014.

[115] K. Tanaka, F. Nishimura, T. Hayashi, H. Tobushi, and C. Lexcellent. Phenomenological analysis on subloops and cyclic behavior in shape memory alloys under mechanical and/or thermal loads. *Mechanics of Materials*, 19(4):281–292, 1995.

[116] D.J. Hartl, G. Chatzigeorgiou, and D.C. Lagoudas. Three-dimensional modeling and numerical analysis of rate-dependent irrecoverable deformation in shape memory alloys. *International Journal of Plasticity*, 26(10):1485–1507, 2010.

[117] A. Paiva, M.A. Savi, A.M.B. Braga, and P.M.C.L. Pacheco. A constitutive model for shape memory alloys considering tensile-compressive asymmetry and plasticity. *International Journal of Solids and Structures*, 42(11-12):3439–3457, 2005.

[118] X.M. Wang, B.X. Xu, and Z.F. Yue. Micromechanical modelling of the effect of plastic deformation on the mechanical behaviour in pseudoelastic shape memory alloys. *International Journal of Plasticity*, 24(8):1307–1332, 2008.

[119] W. Zaki and Z. Moumni. A 3D model of the cyclic thermomechanical behavior of shape memory alloys. *Journal of the Mechanics and Physics of Solids*, 55(11):2427–2454, 2007.

[120] F. Jemal, T. Bouraoui, T. Ben Zineb, E. Patoor, and C. Bradaï. Modelling of martensitic transformation and plastic slip effects on the thermo-mechanical behaviour of Fe-based shape memory alloys. *Mechanics of Materials*, 41(7):849–856, 2009.

[121] Bo Zhou. A macroscopic constitutive model of shape memory alloy considering plasticity. *Mechanics of Materials*, 48:71–81, 2012.

[122] Seong-Woong Kim, Chan Hee Park, Jeoung Han Kim, Jae Keun Hong, and Jong-Taek Yeom. Effect of plastic working on martensitic phase transformation characteristics of TiNi alloys. *Journal of Alloys and Compounds*, 610:315–321, 2014.

[123] T. Iwamoto. Multiscale computational simulation of deformation behavior of TRIP steel with growth of martensitic particles in unit cell by asymptotic homogenization method. *International Journal of Plasticity*, 20(4-5):841–869, 2004.

[124] L. Taleb and S. Petit. New investigations on transformation induced plasticity and its interaction with classical plasticity. *International Journal of Plasticity*, 22(1):110–130, 2006.

[125] S. Turteltaub and A. Suiker. Transformation-induced plasticity in ferrous alloys. *Journal of the Mechanics and Physics of Solids*, 53(8):1747–1788, 2005.

[126] M. Cherkaoui, A. Soulami, A. Zeghloul, and M.A. Khaleel. A phenomenological dislocation theory for martensitic transformation in ductile materials: From micro- to macroscopic description. *Philosophical Magazine*, 88(30-32):3479–3512, 2008.

[127] V.I. Levitas, D.W. Lee, and D.L. Preston. Interface propagation and microstructure evolution in phase field models of stress-induced martensitic phase transformations. *International Journal of Plasticity*, 26(3):395–422, 2010.

[128] V.I. Levitas and I.B. Ozsoy. Micromechanical modeling of stress-induced phase transformations. Part 1. Thermodynamics and kinetics of coupled interface propagation and reorientation. *International Journal of Plasticity*, 25(2):239–280, 2009.

[129] H. Pan, P. Thamburaja, and F.S. Chau. Multi-axial behavior of shape-memory alloys undergoing martensitic reorientation and detwinning. *International Journal of Plasticity*, 23(4):711–732, 2007.

[130] V.G. Kouznetsova and M.G.D. Geers. A multi-scale model of martensitic transformation plasticity. *Mechanics of Materials*, 40(8):641–657, 2008.

[131] V.I. Levitas, A.V. Idesman, G.B. Olson, and E. Stein. Numerical modelling of martensitic growth in an elastoplastic material. *Philosophical Magazine A*, 82(3):429–462, 2002.

[132] V.I. Levitas, A.V. Idesman, and E. Stein. Finite element simulation of martensitic phase transitions in elastoplastic materials. *International Journal of Solids and Structures*, 35(9-10):855–887, 1998.

[133] S. Manchiraju and P.M. Anderson. Coupling between martensitic phase transformations and plasticity: A microstructure-based finite element model. *International Journal of Plasticity*, 26(10):1508–1526, 2010.

[134] S. Manchiraju, D. Gaydosh, O. Benafan, R. Noebe, R. Vaidyanathan, and P.M. Anderson. Thermal cycling and isothermal deformation response of polycrystalline NiTi: Simulations vs. experiment. *Acta Materialia*, 59(13):5238–5249, 2011.

[135] G. Krauss and A.R. Marder. The morphology of martensite in iron alloys. *Metallurgical Transactions*, 2(9):2343–2357, 1971.

[136] J.R.C. Guimarães and P.R. Rios. Unified description of martensite microstructure and kinetics. *Journal of Materials Science*, 44(4):998–1005, 2009.

[137] D.A. Porter and K.E. Easterling. *Phase Transformations in Metals and Alloys*. CRC Press, 1992.

[138] K.F. Hane and T.W. Shield. Microstructure in the cubic to monoclinic transition in titanium-nickel shape memory alloys. *Acta Materialia*, 47(9):2603–2617, 1999.

[139] J.M. Ball and R.D. James. Fine phase mixtures as minimizers of energy. *Archive for Rational Mechanics and Analysis*, 100(1):13–52, 1987.

[140] J.D. Eshelby. The determination of the elastic field of an ellipsoidal inclusion, and related problems. *Proceedings Of The Royal Society Of London Series A-mathematical And Physical Sciences*, 241(1226):376–396, 1957.

[141] T. Mura. *Micromechanics of Defects in Solids*. Martinus Nijhoff, The Netherlands, (2nd ed.) edition, 1987.

[142] K. Tanaka and T. Mura. A theory of fatigue crack initiation at inclusions. *Metallurgical Transactions A*, 13(1):117–123, 1982.

[143] L.P. Kubin and G. Canova. The modeling of dislocation patterns. *Scripta Metallurgica Et Materialia*, 27(8):957–962, 1992.

[144] H.M. Zbib and T.D. de la Rubia. A multiscale model of plasticity. *International Journal of Plasticity*, 18(9):1133–1163, 2002.

[145] R. Abeyaratne and J.K. Knowles. On the driving traction acting on a surface of strain discontinuity in a continuum. *Journal of the Mechanics and Physics of Solids*, 38(3):345–360, 1990.

[146] R. Abeyaratne and J.K. Knowles. A continuum model of a thermoelastic solid capable of undergoing phase transitions. *Journal of the Mechanics and Physics of Solids*, 41(3):541–571, 1993.

[147] S.J. Kim and R. Abeyaratne. On the effect of the heat generated during a stress-induced thermoelastic phase transformation. *Continuum Mechanics and Thermodynamics*, 7(3):311–332, 1995.

[148] K. Otsuka and X. Ren. Recent developments in the research of shape memory alloys. *Intermetallics*, 7(5):511–528, 1999.

[149] J.R. Rice. Tensile crack tip fields in elastic-ideally plastic crystals. *Mechanics of Materials*, 6(4):317–335, 1987.

[150] H. Pan, P. Thamburaja, and F.S. Chau. An isotropic-plasticity-based constitutive model for martensitic reorientation and shape-memory effect in shape-memory alloys. *International Journal of Solids and Structures*, 44(22-23):7688–7712, 2007.

[151] O. Benafan, R.D. Noebe, S.A. Padula, A. Garg, B. Clausen, S. Vogel, and R. Vaidyanathan. Temperature dependent deformation of the B2 austenite phase of a NiTi shape memory alloy. *International Journal of Plasticity*, 51:103–121, 2013.

[152] S.W. Robertson, A.R. Pelton, and R.O. Ritchie. Mechanical fatigue and fracture of Nitinol. *International Materials Reviews*, 57(1):1–37, 2012.

[153] Wei Cai, S. Tanaka, and Kazuhiro Otsuka. Thermal Cyclic Characteristics under Load in a Ti50.6Pd30Ni19.4 Alloy. *Materials Science Forum*, 327-328:279–282, 2000.

[154] K.C. Atli, I. Karaman, R.D. Noebe, a. Garg, Y.I. Chumlyakov, and I.V. Kireeva. Improvement in the Shape Memory Response of Ti50.5Ni24.5Pd25 High-Temperature Shape Memory Alloy with Scandium Microalloying. *Metallurgical and Materials Transactions A*, 41(10):2485–2497, 2010.

[155] E.O. Hall. The Deformation and Ageing of Mild Steel: III Discussion of Results. *Proceedings of the Physical Society. Section B*, 64(9):747–753, 1951.

[156] N.J. Petch. The cleavage strength of polycrystals. *The Journal of the Iron and Steel Institute London*, 173:25–28, 1953.

[157] J. Lian, J.E. Garay, and J. Wang. Grain size and grain boundary effects on the mechanical behavior of fully stabilized zirconia investigated by nanoindentation. *Scripta Materialia*, 56(12):1095–1098, 2007.

[158] H.H. Fu, D.J. Benson, and M.A. Meyers. Analytical and computational description of effect of grain size on yield stress of metals. *Acta Materialia*, 49(13):2567–2582, 2001.

[159] R. Kumar, L. Nicola, and E. Van der Giessen. Density of grain boundaries and plasticity size effects: A discrete dislocation dynamics study. *Materials Science and Engineering: A*, 527(1-2):7–15, 2009.

[160] T. Sawaguchi, M. Sato, and A. Ishida. Microstructure and shape memory behavior of $Ti_{51.2}(Pd_{27.0}Ni_{21.8})$ and $Ti_{49.5}(Pd_{28.5}Ni_{22.0})$ thin films. *Materials Science and Engineering a-Structural Materials Properties Microstructure and Processing*, 332(1-2):47–55, 2002.

[161] P.K. Kumar, U. Desai, J. Monroe, D.C. Lagoudas, I. Karaman, R. Noebe, and G. Bigelow. Phase Transformation and Creep Behavior in $Ti_{50}Pd_{30}Ni_{20}$ High Temperature Shape Memory Alloy in Compression. *Behavior and Mechanics of Multifunctional Materials and Composites*, 7644:1–7, 2010.

[162] P.K. Kumar, U. Desai, J.A. Monroe, D.C. Lagoudas, I. Karaman, G. Bigelow, and R.D. Noebe. Experimental investigation of simultaneous creep, plasticity and transformation of $Ti_{50.5}Pd_{30}Ni_{19.5}$ high temperature shape memory alloy during cyclic actuation. *Materials Science and Engineering: A*, 530:117–127, 2011.

[163] J.A. Monroe, I. Karaman, D.C. Lagoudas, G. Bigelow, R.D. Noebe, and S. Padula. Determining recoverable and irrecoverable contributions to accumulated strain in a NiTiPd high-temperature shape memory alloy during thermomechanical cycling. *Scripta Materialia*, 65(2):123–126, 2011.

[164] G.G. Weber, A.M. Lush, A. Zavaliangos, and L. Anand. An objective time-integration procedure for isotropic rate-independent and rate-dependent elastic-plastic constitutive equations. *International Journal of Plasticity*, 6(6):701–744, 1990.

[165] Q.P. Sun and K.C. Hwang. Micromechanics modelling for the constitutive behavior of polycrystalline shape memory alloys–I. Derivation of general relations. *Journal of the Mechanics and Physics of Solids*, 41(1):1–17, 1993.

[166] A.M. Lush, G. Weber, and L. Anand. An implicit time-integration procedure for a set of internal variable constitutive equations for isotropic elasto-viscoplasticity. *International Journal of Plasticity*, 5(5):521–549, 1989.

[167] J.B. Leblond, J. Devaux, and J.C. Devaux. Mathematical modelling of transformation plasticity in steels I: case of ideal-plastic phases. *International journal of plasticity*, 5:551–572, 1989.

[168] X. Ren and K. Otsuka. Universal symmetry property of point defects in crystals. *Physical Review Letters*, 85(5):1016–9, 2000.

[169] P.K. Kumar and D.C. Lagoudas. Experimental and microstructural characterization of simultaneous creep, plasticity and phase transformation in $Ti_{50}Pd_{40}Ni_{10}$ high-temperature shape memory alloy. *Acta Materialia*, 58(5):1618–1628, 2010.

[170] Lei Qiao, Julian J. Rimoli, Ying Chen, Christopher a. Schuh, and Raul Radovitzky. Nonlocal Superelastic Model of Size-Dependent Hardening and Dissipation in Single Crystal Cu-Al-Ni Shape Memory Alloys. *Physical Review Letters*, 106(8):085504, 2011.

[171] Lifeng Liu, Xiangdong Ding, Ju Li, Turab Lookman, and Jun Sun. Direct observation of hierarchical nucleation of martensite and size-dependent superelasticity in shape memory alloys. *Nanoscale*, 6(4):2067–72, 2014.

[172] E.J. Routh. Theorems on the Attraction of Ellipsoids for Certain Laws of Force Other than the Inverse Square. *Philosophical Transactions of the Royal Society A: Mathematical, Physical and Engineering Sciences*, 186(January):897–950, 1895.

[173] I.S. Gradshteyn and I.M. Ryzhik. *Table of Integrals, Series and Products*. Oxford : Academic, 7th editio edition, 2007.

[174] X. Jin, L.M. Keer, and Q. Wang. A Closed-Form Solution for the Eshelby Tensor and the Elastic Field Outside an Elliptic Cylindrical Inclusion. *Journal of Applied Mechanics*, 78(3):031009, 2011.

[175] J.W. Ju and L.Z. Sun. A Novel Formulation for the Exterior-Point Eshelby's Tensor of an Ellipsoidal Inclusion. *Journal of Applied Mechanics*, 66(2):570, 1999.

Appendix A

Time integration procedure for the isotropic based constitutive model

An explicit time integration procedure is developed to implement the three dimensional constitutive equations. Then, the explicit user subroutine VUMAT is written to use as an input file for ABAQUS explicit package. With t denoting the current time, Δt is an infinitesimal time increment, and $\tau = t + \Delta t$ is the new time. The algorithm is as follows:

Given: (1) $\left\{\mathbf{F}(t), \mathbf{F}(\tau), \theta(t), \theta(\tau), \mathbf{T}(t), \mathbf{F}^{inel}(t), S_A(t), S_M(t)\right\}$; (2) $\{\xi(t)\}$; (3) $\{\mathbf{B}(t), \mathbf{N}_1(t), \mathbf{N}_2(t)\}$.

Calculate: (1) $\left\{\mathbf{T}(\tau), \mathbf{F}^{inel}(\tau), S_A(\tau), S_M(\tau)\right\}$; (2) $\{\xi(\tau)\}$; (3) $\{\mathbf{B}(\tau), \mathbf{N}_1(\tau), \mathbf{N}_2(\tau)\}$.

The steps used to calculate the above unknowns are presented in continue.

Step 1: Calculate the elastic strain $\mathbf{E}^e(t)$:

$$\mathbf{F}^e(t) = \mathbf{F}(t)\,\mathbf{F}^{inel^{-1}}(t), \tag{A.1}$$

$$\mathbf{C}^e(t) = \mathbf{F}^{eT}(t)\,\mathbf{F}^e(t), \tag{A.2}$$

$$\mathbf{E}^e(t) = \frac{1}{2}\left(\mathbf{C}^e(t) - \mathbf{1}\right) - \mathbf{A}\left(\theta(t) - \theta_0\right). \tag{A.3}$$

Step 2: Calculate the stress $\mathbf{T}^*(t)$:

$$\mathbf{T}^*(t) = \mathbb{C}\mathbf{E}^e(t). \tag{A.4}$$

Step 3: Calculate the inelastic strain increment $\Delta\varepsilon^{inel}(t)$:

$$\bar{\sigma}(t) = \sqrt{\frac{3}{2}}\left|\left(\mathbf{C}^e(t)\,\mathbf{T}^*(t)\right)_{dev}\right|, \tag{A.5}$$

$$f(t) = \bar{\varepsilon}^t\left(\bar{\sigma}(t) - \frac{\lambda_T}{\theta_T}\left(\theta(t) - \theta_T\right) - h\xi(t)\right), \tag{A.6}$$

$$\dot{\xi}(t) = sign\left(f(t)\right)\dot{\xi}_0(t)\left(\frac{|f(t)|}{f_c}\right)^{\frac{1}{m}}, \tag{A.7}$$

$$\Delta\varepsilon^t(t) = \bar{\varepsilon}^t\Delta\xi(t), \tag{A.8}$$

$$\Delta\varepsilon^p_A(t) = \Delta\varepsilon_0 sign\left(\overline{\sigma}(t)\right)\left(\frac{\overline{\sigma}(t)}{S_a(t)}\right)^{\frac{1}{n}} exp\left(\frac{-Q_a}{R\theta(t)}\right), \tag{A.9}$$

$$\Delta\varepsilon^{tp} = \Delta\varepsilon_0^{tp}\left(\frac{\overline{\sigma}}{S_a\left(t\right)}\right), \tag{A.10}$$

$$\Delta\varepsilon^{inel}\left(t\right) = \Delta\varepsilon^{t}\left(t\right) + \left(1-\xi\right)\Delta\varepsilon_A^{p}\left(t\right) + \Delta\varepsilon^{tp}\left(t\right). \tag{A.11}$$

Step 4: Update the inelastic deformation gradient $\mathbf{F}^{inel}\left(\tau\right)$:

$$\mathbf{F}^{inel}\left(\tau\right) = \left\{\mathbf{1} + \mathbf{D}^{inel}\left(t\right)\Delta\left(t\right)\right\}\mathbf{F}^{inel}\left(t\right), \tag{A.12}$$

$$\begin{aligned}\mathbf{D}^{inel}\left(t\right) = \sqrt{\frac{3}{2}}\left(\bar{\varepsilon}^{t}\Delta\xi_1\left(t\right)\mathbf{N}_1\left(t\right) + \bar{\varepsilon}^{t}\Delta\xi_2\left(t\right)\mathbf{N}_2\left(t\right)\right) + \\ \sqrt{\frac{3}{2}}\left(\left(1-\xi\right)\Delta\varepsilon_A^{p}\left(t\right) + \Delta\varepsilon^{tp}\left(t\right)\right)\mathbf{N}_3\left(t\right),\end{aligned} \tag{A.13}$$

$$\mathbf{N}_1\left(t\right) = \frac{\mathbf{T}_{dev}^{*}\left(t\right)}{|\mathbf{T}_{dev}^{*}\left(t\right)|}, \tag{A.14}$$

$$\mathbf{N}_2\left(t\right) = \frac{\mathbf{B}\left(t\right)}{|\mathbf{B}\left(t\right)|}, \tag{A.15}$$

$$\mathbf{N}_3\left(t\right) = \frac{\mathbf{T}_{dev}^{*}\left(t\right)}{|\mathbf{T}_{dev}^{*}\left(t\right)|}. \tag{A.16}$$

Step 5: Update the tensor $\mathbf{B}\left(\tau\right)$:

$$\mathbf{B}\left(\tau\right) = \mathbf{B}\left(t\right) + \sqrt{\frac{3}{2}}\sum_{i=1}^{2}\Delta\xi_i\left(t\right)\mathbf{N}_i\left(t\right). \tag{A.17}$$

Step 6: Calculate the elastic strain $\mathbf{E}^{e}\left(\tau\right)$:

$$\mathbf{F}^{e}\left(\tau\right) = \mathbf{F}\left(\tau\right)\mathbf{F}^{inel\,-1}\left(\tau\right), \tag{A.18}$$

$$\mathbf{C}^e(\tau) = \mathbf{F}^{eT}(\tau)\,\mathbf{F}^e(\tau), \tag{A.19}$$

$$\mathbf{E}^e(\tau) = \frac{1}{2}\left(\mathbf{C}^e(\tau) - \mathbf{1}\right) - \mathbf{A}\left(\theta(\tau) - \theta_0\right). \tag{A.20}$$

Step 7: Update the resistance to plastic flow $S_a(\tau)$ and $S_m(\tau)$:

$$S_a(\tau) = S_a(t) + d_{2a}\Delta\varepsilon_A^p(t). \tag{A.21}$$

Step 8: Update the stress $\mathbf{T}^*(\tau)$:

$$\mathbf{T}^*(\tau) = \mathbb{C}\mathbf{E}^e(\tau). \tag{A.22}$$

Step 9: Calculate the Cauchy stress $\mathbf{T}(\tau)$:

$$\mathbf{T}(\tau) = \frac{1}{det\left(\mathbf{F}^e(\tau)\right)}\mathbf{F}^e(\tau)\,\mathbf{T}^*(\tau)\,\mathbf{F}^{eT}(\tau). \tag{A.23}$$

Appendix B

Evaluation of Eshelby solution for inside and outside of cylindrical ellipse inclusion

In this section the analytical solution to find the displacement field $u_i(\mathbf{x})$, strain field $\varepsilon_{ij}(\mathbf{x})$, and stress field $\sigma_{ij}(\mathbf{x})$ for points inside and outside of a cylindrical ellipse inclusion are presented. Mura [141] defined the inclusion as a sub-domain Ω that is surrounded by the matrix which occupies $D-\Omega$. Then, the general form of the displacement, strain, and stress field for points inside and outside of the inclusion are presented as

$$u_i(\mathbf{x}) = -\mathbb{C}_{jkmn} \int_{\Omega} \varepsilon^*_{mn}(\mathbf{x}') G_{ij.k}(\mathbf{x}-\mathbf{x}') d\mathbf{x}', \tag{B.1}$$

$$\varepsilon_{ij}(\mathbf{x}) = -\frac{1}{2}\int_{\Omega} \mathbb{C}_{klmn}\varepsilon^*_{mn}(\mathbf{x}')(G_{ik,lj}(\mathbf{x}-\mathbf{x}') + G_{jk,li}(\mathbf{x}-\mathbf{x}'))d\mathbf{x}', \quad \text{(B.2)}$$

$$\sigma_{ij}(\mathbf{x}) = -\mathbb{C}_{ijkl}(\int_{\Omega} \mathbb{C}_{pqmn}\varepsilon^*_{mn}(\mathbf{x}')G_{kp,ql}(\mathbf{x}-\mathbf{x}')d\mathbf{x}' + \varepsilon^*_{kl}(\mathbf{x}')), \quad \text{(B.3)}$$

where $\mathbb{C}_{ijkl}$ is the stiffness tensor and it is assumed that the stiffness of inside and outside of inclusion are the same, G_{ij} is Green's tensor function, $\mathbf{x}$ is the position vector and $\mathbf{x}'$ is the position vector of a point source, $\boldsymbol{\varepsilon}^*$ is the eigenstrain in Ω and it is zero in $D-\Omega$.

One of the important results of Eshelby is that the strain and stress field is uniform for interior points of an ellipsoidal inclusion. For brevity the proof that is presented in [140, 141] is not repeated here.

In the next sections the close forms of Eshelby solution for interior and exterior points of an ellipsoidal inclusions are presented. It is assumed that the domain of ellipsoidal Ω is

$$\frac{x_1^2}{a_1^2} + \frac{x_2^2}{a_2^2} + \frac{x_3^2}{a_3^2} \leq 1, \quad \text{(B.4)}$$

where a_1, a_2, and a_3 are ellipsoidal diameters. Furthermore, according to [141] the Green's function for isotropic materials is

$$G_{ij.k}(\mathbf{x}-\mathbf{x}') = \frac{1}{16\pi\mu(1-\nu)\left|\mathbf{x}-\mathbf{x}'\right|}\left[(3-4\nu)\delta_{ij} + \frac{(x_i - x_i')(x_j - x_j')}{\left|\mathbf{x}-\mathbf{x}'\right|^2}\right]. \quad \text{(B.5)}$$

B.1 Interior points

If the eigenstrain of the inclusion is constant and as Eshelby proved the strain and stress field inside the ellipsoidal inclusion are uniform, the $\boldsymbol{\varepsilon}^*$ can be out of the integration in equation (B.2). Therefore, for interior points:

$$\varepsilon_{ij}(\mathbf{x}) = S_{ijkl}\varepsilon^*_{kl} \qquad \text{for} \qquad \mathbf{x} \in \Omega, \tag{B.6}$$

where S_{ijkl} is called the Eshelby tensor and it is constant for interior points of the inclusion. Mura [141] showed the forth order Eshelby tensor in the form of

$$\begin{cases} S_{ijkl} = S_{jikl} = S_{ijlk}, \\ S_{1111} = \frac{3}{8\pi(1-\nu)}a_1^2 I_{11} + \frac{1-2\nu}{8\pi(1-\nu)}I_1, \\ S_{1122} = \frac{1}{8\pi(1-\nu)}a_2^2 I_{12} - \frac{1-2\nu}{8\pi(1-\nu)}I_1, \\ S_{1133} = \frac{3}{8\pi(1-\nu)}a_3^2 I_{13} - \frac{1-2\nu}{8\pi(1-\nu)}I_1, \\ S_{1212} = \frac{a_1^2+a_2^2}{16\pi(1-\nu)}I_{12} + \frac{1-2\nu}{16\pi(1-\nu)}(I_1 + I_2), \end{cases} \tag{B.7}$$

and the all other components can be found by cyclic permutation. The component which can not found by this way are zero. Furthermore I_i and

I_{ij} are integrals which are presented by Routh [172] as

$$\begin{cases} I_1 = 2\pi a_1 a_2 a_3 \int_0^\infty \frac{ds}{(a_1^2+s)\Delta(s)}, \\ I_{11} = 2\pi a_1 a_2 a_3 \int_0^\infty \frac{ds}{(a_1^2+s)^2\Delta(s)}, \\ I_{12} = 2\pi a_1 a_2 a_3 \int_0^\infty \frac{ds}{(a_1^2+s)(a_2^2+s)\Delta(s)}, \end{cases} \tag{B.8}$$

where $\Delta(s) = (a_1^2+s)^{\frac{1}{2}}(a_2^2+s)^{\frac{1}{2}}(a_3^2+s)^{\frac{1}{2}}$ and s is the integration variable. The rest integrals will be found by cyclic permutation. If it is considered $a_1 > a_2 > a_3$, then the above integrals are rewritten in the standard elliptical [173]:

$$\begin{cases} I_1 = \frac{4\pi a_1 a_2 a_3}{(a_1^2-a_2^2)(a_1^2-a_3^2)^{\frac{1}{2}}} \left\{F(\theta,k) - E(\theta,k)\right\}, \\ I_3 = \frac{4\pi a_1 a_2 a_3}{(a_2^2-a_3^2)(a_1^2-a_3^2)^{\frac{1}{2}}} \left\{\frac{a_2(a_1^2-a_3^2)^{\frac{1}{2}}}{a_1 a_3} - E(\theta,k)\right\}, \end{cases} \tag{B.9}$$

where

$$\begin{cases} F(\theta,k) = \int_0^\theta \frac{dw}{(1-k^2 sin^2 w)^{\frac{1}{2}}}, \\ E(\theta,k) = \int_0^\theta (1-k^2 sin^2 w)^{\frac{1}{2}} dw, \end{cases} \tag{B.10}$$

and

$$\begin{cases} \theta = sin^{-1}(1-\frac{a_3^2}{a_1^2})^{\frac{1}{2}}, \\ k = \left\{\frac{(a_1^2-a_2^2)}{(a_1^2-a_3^2)}\right\}^{\frac{1}{2}}. \end{cases} \tag{B.11}$$

Mura [141] combined (B.8) to (B.11) and simplified the relationship

between I_i and I_{ij} as:

$$\begin{cases} I_1 + I_2 + I_3 = 4\pi, \\ 3I_{11} + I_{12} + I_{13} = \frac{4\pi}{a_1^2}, \\ 3a_1^2 I_{11} + a_2^2 I_{12} + a_3^2 I_{13} = 3I_1, \\ I_{12} = \frac{I_2 - I_1}{a_1^2 - a_2^2}. \end{cases} \tag{B.12}$$

Then for the special case of the elliptical cylinder ($a_3 \to \infty$), the above integrals for the interior points are simplified to

$$\begin{cases} I_1 = \frac{4\pi a_2}{a_1 + a_2}, \\ I_2 = \frac{4\pi a_1}{a_1 + a_2}, \\ I_3 = 0, \\ I_{12} = \frac{4\pi}{(a_1 + a_2)^2}, \\ 3I_{11} = \frac{4\pi}{(a_1)^2} - I_{12}, \\ 3I_{22} = \frac{4\pi}{(a_2)^2} - I_{12}, \\ I_{13} = \frac{I_1}{a_3^2} = 0, \\ I_{23} = \frac{I_2}{a_3^2} = 0, \\ I_{33} = \frac{0}{a_3^2} = 0, \end{cases} \tag{B.13}$$

and the components of Eshelby tensor for interior points are

$$\begin{cases} S_{1111} = \frac{1}{2(1-\nu)}\left\{\frac{a_2^2+2a_1a_2}{(a_1+a_2)^2} + (1-2\nu)\frac{a_2}{a_1+a_2}\right\}, \\ S_{2222} = \frac{1}{2(1-\nu)}\left\{\frac{a_1^2+2a_1a_2}{(a_1+a_2)^2} + (1-2\nu)\frac{a_1}{a_1+a_2}\right\}, \\ S_{3333} = 0, \\ S_{1122} = \frac{1}{2(1-\nu)}\left\{\frac{a_2^2}{(a_1+a_2)^2} - (1-2\nu)\frac{a_2}{a_1+a_2}\right\}, \\ S_{2233} = \frac{1}{2(1-\nu)}\frac{2\nu a_1}{a_1+a_2}, \\ S_{3311} = 0, \\ S_{1133} = \frac{1}{2(1-\nu)}\frac{2\nu a_2}{a_1+a_2}, \\ S_{2211} = \frac{1}{2(1-\nu)}\left\{\frac{a_1^2}{(a_1+a_2)^2} - (1-2\nu)\frac{a_1}{a_1+a_2}\right\}, \\ S_{3322} = 0, \\ S_{1212} = \frac{1}{2(1-\nu)}\left\{\frac{a_1^2+a_2^2}{2(a_1+a_2)^2} + \frac{1-2\nu}{2}\right\}, \\ S_{2323} = \frac{a_1}{2(a_1+a_2)}, \\ S_{2323} = \frac{a_2}{2(a_1+a_2)}. \end{cases} \tag{B.14}$$

Therefore by having the eigenstrain the close form of strain and stress fields for interior points can be found by:

$$\begin{cases} \varepsilon_{ij} = S_{ijkl}\varepsilon^*_{kl}, \\ \sigma_{ij} = \mathbb{C}_{ijkl}\varepsilon_{kl}. \end{cases} \tag{B.15}$$

B.2 Exterior points

When the point is outside of ellipsoidal inclusion the strain and stress fields are not uniform therefore, the solution is slightly different with interior points. As the eigenstrain ($\boldsymbol{\varepsilon}^*$) for the exterior points are the same as interior points, the equation (B.2) can be written in the form of

$$\varepsilon_{ij}(\mathbf{x}) = D_{ijkl}(\mathbf{x})\varepsilon^*_{kl}, \tag{B.16}$$

where it is shown in [141] that

$$\begin{aligned}
8\pi(1-\nu)D_{ijkl}(\mathbf{x}) &= 8\pi(1-\nu)S_{ijkl}(\lambda) + 2\nu\delta_{kl}x_i I_{I,j}(\lambda) \\
&+(1-\nu)\{\delta_{il}x_k I_{K,j}(\lambda) + \delta_{jl}x_k I_{k,i}(\lambda) + \delta_{ik}x_l I_{L,j}(\lambda) + \delta_{jk}x_l I_{L,i}(\lambda)\} \\
&-\delta_{ij}x_k[I_K(\lambda) - a_I^2 I_{KI}(\lambda)]_{,l} - (\delta_{ik}x_j + \delta_{jk}x_i)[I_J(\lambda) - a_I^2 I_{IJ}(\lambda)]_{,l} \\
&-(\delta_{il}x_j + \delta_{jl}x_i)[I_J(\lambda) - a_I^2 I_{IJ}(\lambda)]_{,k} - x_i x_j[I_J(\lambda) - a_I^2 I_{IJ}(\lambda)]_{,lk}.
\end{aligned} \tag{B.17}$$

In the expression (B.17) only the repeated lower case indices are summed over while the upper case indices are the same number as lower case but without any summation. δ_{ij} is the Dirak delta and λ is a parameter for exterior points which is defined as the largest positive root of

$$\frac{x_1^2}{a_1^2+\lambda} + \frac{x_2^2}{a_2^2+\lambda} + \frac{x_3^2}{a_3^2+\lambda} = 1. \tag{B.18}$$

Equation (B.18) describes an imaginary ellipsoid which is constructed to include the exterior points. It is clear that for the interior points $\lambda = 0$. I_i and I_{ij} are similar to what is defined in equation (B.8) but the lower limit of the integral is λ. To find $D_{ijkl}(\mathbf{x})$, I_i and I_{ij} as well as their first and second-ordered derivation in respect to x_i are needed. I_i and I_{ij} can be found like equations (B.9) and (B.12)

$$\begin{cases} I_1(\lambda) = \frac{4\pi a_1 a_2 a_3}{(a_1^2-a_2^2)(a_1^2-a_3^2)^{\frac{1}{2}}} \left\{F(\theta(\lambda),k) - E(\theta(\lambda),k)\right\}, \\ I_3(\lambda) = \frac{4\pi a_1 a_2 a_3}{(a_2^2-a_3^2)(a_1^2-a_3^2)^{\frac{1}{2}}} \left\{ \frac{(a_2^2+\lambda)(a_1^2-a_3^2)^{\frac{1}{2}}}{\prod_k (a_k^2+\lambda)^{\frac{1}{2}}} - E(\theta(\lambda),k) \right\}, \\ I_2(\lambda) = \frac{4\pi a_1 a_2 a_3}{\prod_k (a_k^2+\lambda)^{\frac{1}{2}}} - I_1(\lambda) - I_3(\lambda), \\ I_{ij}(\lambda) = -\frac{I_i(\lambda)-I_j(\lambda)}{(a_i^2-a_j^2)} \qquad \text{for} \qquad i \neq j, \\ I_{ii}(\lambda) = \frac{4\pi a_1 a_2 a_3}{3(a_i^2+\lambda)\prod_k (a_k^2+\lambda)^{\frac{1}{2}}} - \frac{\sum_j I_{ij}(\lambda)}{3} \qquad \text{no summation on i,} \end{cases} \tag{B.19}$$

where $F(\theta(\lambda),k)$ and $E(\theta(\lambda),k)$ are the same as equation (B.10) but θ has been modified to $\theta(\lambda)$ and calculated as

$$\theta = sin^{-1}\left(\frac{a_1^2 - a_3^2}{a_1^2 + \lambda}\right)^{\frac{1}{2}}. \tag{B.20}$$

Mura calculate the first and second-order derivation of I_i and I_{ij} inte-

grals as

$$\begin{cases} I_{i,j}(\lambda) = \frac{-2\pi a_1 a_2 a_3}{(a_i^2+\lambda)\prod_m (a_m^2+\lambda)^{\frac{1}{2}}} \lambda_{,j}, \\ I_{ij,k}(\lambda) = \frac{-2\pi a_1 a_2 a_3}{(a_i^2+\lambda)(a_j^2+\lambda)\prod_m (a_m^2+\lambda)^{\frac{1}{2}}} \lambda_{,k}, \\ I_{i,jk}(\lambda) = \frac{-2\pi a_1 a_2 a_3}{(a_i^2+\lambda)\prod_m (a_m^2+\lambda)^{\frac{1}{2}}} \left(\lambda_{,jk} - \left(\frac{1}{a_i^2+\lambda} + \frac{1}{2}\sum_n \frac{1}{a_n^2+\lambda} \right) \lambda_{,j}\lambda_{,k} \right), \\ I_{ij,kl}(\lambda) = \frac{-2\pi a_1 a_2 a_3}{(a_i^2+\lambda)(a_j^2+\lambda)\prod_m (a_m^2+\lambda)^{\frac{1}{2}}} \left(\lambda_{,kl} - \left(\frac{1}{a_i^2+\lambda} + \frac{1}{a_j^2+\lambda} + \frac{1}{2}\sum_n \frac{1}{a_n^2+\lambda} \right) \lambda_{,k}\lambda_{,l} \right). \end{cases} \tag{B.21}$$

Also from equation (B.18) the first and second derivative of $\lambda(\mathbf{x})$ is calculated as

$$\begin{cases} \lambda_{,j} = \frac{2x_i}{a_I^2+\lambda} / \frac{x_j x_j}{(a_j^2+\lambda)^2}, \\ \lambda_{,ij} = \frac{F_{i,j} - \lambda_{,i} C_{,j}}{C}, \end{cases} \tag{B.22}$$

where

$$\begin{cases} F_i = \frac{2x_i}{a_I^2+\lambda}, \\ C = \frac{x_i x_i}{(a_I^2+\lambda)^2}. \end{cases} \tag{B.23}$$

By substituting equations (B.19) and (B.21) in equation (B.17) $D_{ijkl}(\mathbf{x})$ can be found.

Furthermore, Jin et al [174] used the analytical formulation by Ju and Sun [175] for Eshelby solution for point outside of the ellipsoidal inclusion and then presented a close form expression for the elastic fields of exterior points. According to Ju and sun [175] $\mathbf{n} = \mathbf{n}(n_1, n_2.n_3)$ is outward unit normal at point $\mathbf{x}$ on the imaginary ellipsoidal surface. Then the $D_{ijkl}(\mathbf{x})$

is rewritten as

$$\begin{aligned} D_{ijkl}(x) = \delta_{ij}\delta_{kl}\left[\frac{\nu}{1-\nu}Q_I^{(1)}(\lambda) + Q_{IK}^{(2)}(\lambda)\right] \\ +(\delta_{ik}\delta_{jl}+\delta_{il}\delta_{jk})\left[\frac{Q_I^{(1)}(\lambda)+Q_J^{(1)}(\lambda)}{2} + Q_{IJ}^{(2)}(\lambda)\right] \\ +Q_I^{(3)}(\lambda)(\delta_{ij}n_kn_l+\delta_{il}n_jn_k) + Q_J^{(3)}(\lambda)(\delta_{jk}n_in_l+\delta_{jl}n_in_k) \\ +Q_K^{(3)}(\lambda)(\delta_{kl}n_in_j+\delta_{ki}n_jn_l) + Q_{ijkl}^{(4)}(\lambda) + \left[Q_{IJKL}^{(5)}(\lambda)+Q^{(6)}(\lambda)\right]n_in_jn_kn_l. \end{aligned} \tag{B.24}$$

The Q functions are presented as

$$\begin{cases} Q_M^{(1)}(\lambda) = \frac{1}{4\pi}I_M, \\ Q_{MN}^{(2)}(\lambda) = \frac{1}{8\pi(1-\nu)}\left[a_N^2 I_{MN} - I_M\right] = \frac{1}{8\pi(1-\nu)}\left[a_M^2 I_{NM} - I_N\right] = Q_{NM}^{(2)}(\lambda), \\ Q_M^{(3)}(\lambda) = \frac{\rho_1(\lambda)\rho_2(\lambda)\rho_3(\lambda)}{2(1-\nu)}\left[1-\rho_M^2(\lambda)\right], \\ Q_{ijkl}^{(4)}(\lambda) = -\frac{\rho_1(\lambda)\rho_2(\lambda)\rho_3(\lambda)}{2}\left(\delta_{ik}n_jn_l+\delta_{il}n_jn_k+\delta_{jk}n_in_l+\delta_{jl}n_in_k+\frac{2\nu}{1-\nu}\delta_{kl}n_in_j\right), \\ Q_{IJKL}^{(5)}(\lambda) = \frac{\rho_1(\lambda)\rho_2(\lambda)\rho_3(\lambda)}{1-\nu}\left[\rho_I^2(\lambda)+\rho_J^2(\lambda)+\rho_K^2(\lambda)+\rho_L^2(\lambda)\right], \\ Q^{(6)}(\lambda) = \frac{\rho_1(\lambda)\rho_2(\lambda)\rho_3(\lambda)}{2(1-\nu)}\left[\rho_m(\lambda)\rho_m(\lambda) - 4\rho_m^2(\lambda)n_mn_m - 5\right], \end{cases} \tag{B.25}$$

where

$$\rho_M(\lambda) = \frac{a_M}{\sqrt{a_M^2+\lambda}}. \tag{B.26}$$

The close-form of Eshelby tensor for exterior points of elliptical inclusion is obtained by letting $a_3 \to \infty$. Therefore, $n_3 = 0$ and $\rho_3 = 1$. Then the λ,

ρ_i, and n_i are simplified as

$$\lambda = \frac{1}{2}\left[x_1^2 + x_2^2 - a_1^2 - a_2^2 + \sqrt{(x_1^2 + x_2^2 - a_1^2 + a_2^2)^2 + 4(a_1^2 - a_2^2 x_2^2)}\right], \tag{B.27}$$

and

$$\begin{cases} \rho_1 = \frac{a_1}{\sqrt{a_1^2+\lambda}}, \\ \rho_2 = \frac{a_2}{\sqrt{a_2^2+\lambda}}, \\ n_1 = \frac{m_1}{\sqrt{m_1^2+m_2^2}}, \\ n_2 = \frac{m_2}{\sqrt{m_1^2+m_2^2}}, \end{cases} \tag{B.28}$$

where

$$\begin{cases} m_1 = \frac{x_1}{a_1^2+\lambda}, \\ m_2 = \frac{x_2}{a_2^2+\lambda}. \end{cases} \tag{B.29}$$

By using equation (B.19) and above consideration for elliptic cylindrical inclusion the close form of I integrals are

$$\begin{cases} I_1(\lambda) = \frac{4\pi\rho_1^2\rho_2 a_2}{a_1\rho_2+a_2\rho_1}, \\ I_2(\lambda) = \frac{4\pi\rho_2^2\rho_1 a_1}{a_1\rho_2+a_2\rho_1}, \\ I_{12}(\lambda) = I_{21}(\lambda) = \frac{4\pi\rho_1^3\rho_2^3}{(a_1\rho_2+a_2\rho_1)^2}, \\ I_{11}(\lambda) = \frac{4\pi\rho_1^4\rho_2 a_2}{3a_1^2}\frac{(2a_1\rho_2+a_2\rho_1)}{a_1\rho_2+a_2 rho_1}^2, \\ I_{22}(\lambda) = \frac{4\pi\rho_2^4\rho_1 a_1}{3a_2^2}\frac{(2a_2\rho_1+a_1\rho_2)}{a_1\rho_2+a_2 rho_1}^2, \\ I_3(\lambda) = I_{33}(\lambda) = I_{13}(\lambda) = I_{31}(\lambda) = I_{23}(\lambda) = I_{32}(\lambda) = 0. \end{cases} \tag{B.30}$$

APPENDIX B. EVALUATION OF ESHELBY SOLUTION FOR INSIDE AND OUTSIDE OF CYLINDRICAL ELLIPSE INCLUSION

By substitution of equation (B.30) into equation (B.25) and then in (B.24) the components of the close form of the Eshelby tensor for exterior points ($D_{ijkl}(\mathbf{x})$) are presented as

$$
\begin{cases}
D_{1111}(\mathbf{x}) = \frac{(1-2\nu)I_1(\lambda)+3a_1^2 I_{11}(\lambda)}{8\pi(1-\nu)} + \frac{\rho_1\rho_2 n_1^2}{2(1-\nu)}\left[2+2\nu-6\rho_1^2+(8\rho_1^2+T_6)n_1^2\right], \\
D_{2222}(\mathbf{x}) = \frac{(1-2\nu)I_2(\lambda)+3a_2^2 I_{22}(\lambda)}{8\pi(1-\nu)} + \frac{\rho_1\rho_2 n_2^2}{2(1-\nu)}\left[2+2\nu-6\rho_2^2+(8\rho_2^2+T_6)n_2^2\right], \\
D_{1122}(\mathbf{x}) = \frac{(2\nu-1)I_1(\lambda)+a_2^2 I_{12}(\lambda)}{8\pi(1-\nu)} + \\
\frac{\rho_1\rho_2}{2(1-\nu)}\left[(1-\rho_1^2)n_2^2+(1-2\nu-\rho_2^2)n_1^2+(4\rho_1^2+4\rho_2^2+T_6)n_1^2n_2^2\right], \\
D_{2211}(\mathbf{x}) = \frac{(2\nu-1)I_2(\lambda)+a_1^2 I_{12}(\lambda)}{8\pi(1-\nu)} + \\
\frac{\rho_1\rho_2}{2(1-\nu)}\left[(1-\rho_2^2)n_1^2+(1-2\nu-\rho_1^2)n_2^2+(4\rho_1^2+4\rho_2^2+T_6)n_1^2n_2^2\right], \\
D_{1212}(\mathbf{x}) = \frac{(1-2\nu)[I_1(\lambda)+I_2(\lambda)]+(a_1^2+a_2^2)I_{12}(\lambda)}{16\pi(1-\nu)} + \\
\frac{\rho_1\rho_2}{2(1-\nu)}\left[(\nu-\rho_2^2)n_1^2+(\nu-\rho_1^2)n_2^2+(4\rho_1^2+4\rho_2^2+T_6)n_1^2n_2^2\right], \\
D_{1112}(\mathbf{x}) = \frac{\rho_1\rho_2 n_1 n_2}{2(1-\nu)}\left[1+2\nu-3\rho_1^2+(6\rho_1^2+2\rho_2^2+T_6)n_1^2\right], \\
D_{2212}(\mathbf{x}) = \frac{\rho_1\rho_2 n_1 n_2}{2(1-\nu)}\left[1+2\nu-3\rho_2^2+(6\rho_2^2+2\rho_1^2+T_6)n_2^2\right], \\
D_{1211}(\mathbf{x}) = \frac{\rho_1\rho_2 n_1 n_2}{2(1-\nu)}\left[1-3\rho_1^2+(6\rho_1^2+2\rho_2^2+T_6)n_1^2\right], \\
D_{1222}(\mathbf{x}) = \frac{\rho_1\rho_2 n_1 n_2}{2(1-\nu)}\left[1-3\rho_2^2+(6\rho_2^2+2\rho_1^2+T_6)n_2^2\right], \\
D_{1133}(\mathbf{x}) = \frac{\nu}{(1-\nu)}\left[\frac{I_1(\lambda)}{4\pi}-\rho_1\rho_2 n_1^2\right], \qquad D_{2233}(\mathbf{x}) = \frac{\nu}{(1-\nu)}\left[\frac{I_2(\lambda)}{4\pi}-\rho_1\rho_2 n_2^2\right], \\
D_{2323}(\mathbf{x}) = \frac{1}{2}\left[\frac{I_2(\lambda)}{4\pi}-\rho_1\rho_2 n_2^2\right], \qquad D_{3131}(\mathbf{x}) = \frac{1}{2}\left[\frac{I_1(\lambda)}{4\pi}-\rho_1\rho_2 n_1^2\right], \\
D_{1233}(\mathbf{x}) = -\frac{\nu}{(1-\nu)}\rho_1\rho_2 n_1 n_2, \qquad D_{3123}(\mathbf{x}) = D_{2331}(\mathbf{x}) = -\frac{\rho_1\rho_2}{(2)} n_1 n_2,
\end{cases}
\tag{B.31}
$$

where

$$T_6 = \rho_1^2 + \rho_2^2 - 4\rho_1^2 n_1^2 - 4\rho_2^2 n_2^2 - 4. \tag{B.32}$$

Therefore, for the exterior points the strain and stress fields can be calculated by

$$\begin{cases} \varepsilon_{ij} = D_{ijkl}(\mathbf{x})\varepsilon^*_{kl}, \\ \\ \sigma_{ij} = \mathbb{C}_{ijkl}\varepsilon_{kl}. \end{cases} \tag{B.33}$$

As can be seen in [141], the displacement field for points inside and outside of the inclusion is given by

$$u_i(\mathbf{x}) = \frac{1}{8\pi(1-\nu)}(\psi_{,jli}\varepsilon^*_{jl} - 2\nu\varepsilon^*_{mm}\phi_{,i} - 4(1-\nu)\varepsilon^*_{il}\phi_{,l}), \tag{B.34}$$

where ϕ and ψ are defined as

$$\begin{cases} \phi(\mathbf{x}) = \int_\Omega |x - x'|\, dx', \\ \\ \psi(\mathbf{x}) = \int_\Omega \frac{1}{|x-x'|} dx'. \end{cases} \tag{B.35}$$

Then the above integrals are expressed in the form of elliptic integrals ($I_i(\lambda)$, $I_{ij}(\lambda)$)

$$\begin{cases} \phi = \frac{1}{2}(I(\lambda) - x_n x_n I_N(\lambda)), \\ \\ \psi_{,i} = \frac{1}{2}x_i(I(\lambda) - x_n x_n I_N(\lambda) - a_I^2(I_I(\lambda) - x_n x_n I_{IN}(\lambda))), \end{cases} \tag{B.36}$$

where

$$I(\lambda) = \frac{4\pi a_1 a_2 a_3 F(\theta(\lambda), k)}{(a_1^2 - a_3^2)^{\frac{1}{2}}}. \tag{B.37}$$

Mura [141] has expressed $\phi_{,i}$ and $\psi_{,ijl}$ in terms of I_i and I_{ij} and their first order derivatives as

$$\begin{cases} \phi_{,i} = -x_i I_I(\lambda)), \\ \psi_{,ijl} = -\delta_{ij} x_l (I_L(\lambda) - a_I^2 I_{IL}(\lambda)) - x_i x_j (I_J(\lambda) - a_I^2 I_{IJ}(\lambda))_{,l} - \\ (\delta_{il} x_j + \delta_{jl} x_i)(I_J(\lambda) - a_I^2 I_{IJ}(\lambda)). \end{cases} \tag{B.38}$$

Then by substituting (B.38) in (B.34) the displacement field $u_i(\mathbf{x})$ for interior and exterior points of elliptical inclusion will be expressed in close form.